DEVELOPMENT OF A NEW CELL DESIGN FOR BATTERY RESEARCH AND AN
INVESTIGATION OF ELECTRODE MATERIALS AND ELECTROLYTE SYSTEMS
FOR Mg BATTERIES

by

Periyapperuma Achchige Mary Kalani Erangi

Submitted in partial fulfilment of the requirements
for the degree of Master of Science

at

Dalhousie University
Halifax, Nova Scotia
August 2014

TABLE OF CONTENTS

LIST OF FIGURES

ABSTRACT

Magnesium batteries are currently being investigated as an inexpensive and high energy density alternative to Li-ion batteries. Many challenges are yet to be overcome before they are applied in practical applications. One of these challenges is the lack of appropriate, inexpensive cell hardware to test new electrode materials and electrolytes. In this work a new electrochemical test cell design based on low cost and readily available Conflat vacuum fittings is introduced. These cells can easily be adapted to either 2 or 3-electrode cells, and are capable of operating at temperatures up to 200°C.

As an alternative to Mg metal anodes, in this work it was found that sputtered Pb films could be used as anode materials. Pb films were found to reversibly alloy electrochemically with Mg in Grignard based electrolytes. The voltage curve has a single plateau at about 125 mV vs. Mg, corresponding to the formation of Mg_2Pb, as confirmed by ex-situ X-ray diffraction. Pb was found to be the highest energy density Mg alloy yet reported, with the lowest voltage and highest volumetric capacity of any Mg alloy.

The Mo_6S_8 Chevrel phase is one of the most reversible cathode electrode materials for Mg intercalation known. This work presents a new method of synthesizing $Cu_2Mo_6S_8$ by solid state synthesis of mechanically milled Cu, Mo and MoS_2 precursors. This method resulted in a significantly reduced sintering time. Finally preliminary research work on investigating potential electrolytes other than Grignard reagents for rechargeable Mg batteries is presented. Electrolytes containing $Mg(TFSI)_2$ salts in solvents such as diglyme, adiponitrile, acetonitrile, 1,2-dimethoxyethane showed electrochemical activity against stainless steel substrates at different temperatures that might be caused by either reversible magnesium plating/stripping or electrolyte decomposition reactions.

LIST OF ABBREVIATIONS USED

SEI	Solid electrolyte interface
SS	Stainless steel
$Mg(TFSI)_2$	Magnesium bis(trifluoromethanesulfonyl)imide
PC	Propylene carbonate
THF	Tetrahydrofuran
DME	1, 2-dimethoxyethane
MCMB	Mesocarbon microbeads
EC	Ethylene carbonate
DMC	Dimethyl carbonate
DEC	Diethyl carbonate
LiTFSI	Lithium bis(trifluoromethanesulfonyl)imide
XRD	X-Ray diffraction
FWHM	Full width half maximum
SEM	Scanning electron microscopy
CV	Cyclic voltammetry
WE	Working electrode
CE	Counter electrode
RE	Reference electrode
LTO	Lithium titanium oxide
LFP	Lithium iron phosphate
WC	Tungsten carbide
PVDF	Poly(vinylidene fluoride)

SP	Super P
NMP	N-Methyl-2-pyrrolidone
PTFE	Polytetrafluroethylene
BMF	Polyethylene blown microfiber
ACN	Acetonitrile
HDPE	High density polyethylene
HMDS	Hexamethyldisilazide
BMIm	Butylmethylimidazolium
PY	Pyridine
ADN	Adiponitrile

ACKNOWLEDGEMENTS

First I would like to thank Dr. Obrovac for giving me support, guidance and encouragement throughout these past two years. I couldn't thank enough for your patience and all the kind words even when I am having rough times with my research work. You are one of the best supervisors someone could ever have and I enjoyed every bit of working with you.

I would like to thank Dr. Timothy Hatchard for being so supportive to me whenever I needed help with machines or vacuum pumps or any other research related work. Also I would like to thank my committee Dr. Josef Zwanziger and Dr. Peng Zhang. Many thanks to Dr. Jeff Dahn allowing me to use instruments in Dahn lab, Simon Trussler, Kevin Borgel and John Noddin for their help with machining; Patricia Scallion for SEM work.

Many thanks to my fellow lab mates, you guys were always helpful to me and full of fun: Lauren MacEachern, Ryan Fielden, Zack Brown, Zhijia Du, Xiuyun Zhao, Douglas Iaboni, Lituo Zheng, Leyi Zhao, John Thorne, past lab members Tuan Tran, Leah Ellis, all the summer students and also Jan Poehls (Dr. Mary Anne White's lab).

Lastly I would like to thank my friends and family! Thank you to my friends and family back at home, Sri Lanka, for keeping in touch with me and kept me entertained with everyday stories. Also to my friends in Halifax who kept me from feeling alone in a new country. Finally, thank you to Thushan, who continuously gave me love, confidence and fun times to carry on when I needed the most. Thank you all a lot!

CHAPTER 1   INTRODUCTION

Lithium ion (Li-ion) batteries are one of the most widely used rechargeable batteries in the world due to their attractive features compared to other cell chemistries. This includes high specific energies (~240 Wh/kg), high volumetric energy densities (~640 Wh/L), long cycle life (>1000 cycles) and a broad temperature range of operation (-40°C to 65°C).[1] Since the introduction of the first Li-ion battery in the 1990s, improvements in the above characteristics enabled Li-ion batteries to be used in a wide variety of applications, such as in portable electronic devices. Recently, automobile manufacturers such as Tesla, and Toyota have introduced Li-ion batteries to power hybrid and full electric vehicles to reduce vehicle fuel consumption.[2]

Although Li-ion batteries are a commercial reality in hybrid and electric vehicles, issues still exist especially in terms of cost and cycle life. While continuous work is carried out to improve Li-ion batteries, research attention is also being focused on the development of alternative high performance battery technologies.

Magnesium batteries are long considered as a promising technology due to the divalent nature of magnesium ions (Mg-ions) and the theoretically high volumetric energy density of a Mg metal anode compared to the Li metal or graphite anodes used in Li batteries. Compared to lithium, magnesium metal has superior thermal and air stability due to the formation of protective thin oxide film on metal surface. Magnesium also has a high natural abundance (13.9%) compared to Li (0.0007%)[3] and is relatively inexpensive.[4]

Continuous research efforts in Li-ion batteries resulted from their mass commercialization, while magnesium batteries have drawn less research attention.

1

Progress in Mg batteries, chiefly by the efforts of Aurbach et al., has increased interest in this area.[5] Aurbach et al. introduced a working Mg battery where a magnesium metal anode was cycled with high efficiency and high cycle life at laboratory scale versus a Mo_6S_8 Chevrel phase cathode material in Grignard based electrolytes. Since then, research attention in this field towards developing new electrode materials and compatible electrolyte systems to be used in practical Mg batteries has increased. Despite many achievements in recent years, the advancement of Mg batteries still faces many challenges.

1.1 Motivation

A fundamental challenge of magnesium intercalation is the difficulty of two electron transfer during Mg^{2+} insertion in inorganic hosts. This is due to the strong polarization of the small, divalent Mg^{2+} ion when compared to similarly sized, but monovalent Li^+ ion.[6] It has been shown that Chevrel phase Mo_6T_8 (T = S, Se) materials allow relatively fast and reversible Mg intercalation at ambient temperatures and have much improved kinetics at high temperatures.[7] Nevertheless, the high cost and low specific and volumetric energy densities of Mo_6S_8 Chevrel phase prevents it from being used in practical Mg batteries.

As mentioned above, the low cost, low electrochemical potential, high volumetric and specific capacity of Mg metal make it an attractive negative electrode for rechargeable batteries. Mg cannot be electrodeposited from most of the commonly used aprotic organic electrolyte solutions due to the formation of a passivation film on the Mg electrode owing to its high reactivity towards electrolyte components.[8,9] Unlike the solid electrolyte interface (SEI) formed on Li metal which is electronically insulating, but ionically conducting, the surface film on the Mg electrode acts as a blocking layer which

insulates both electron and ion transfer. Figure 1.1 shows the cyclic voltammogram of a

Mo_6S_8/Mg/stainless steel (SS) 3-electrode Conflat cell (to be described in Chapter 8)

cycled with 0.5M $Mg[N(SO_2CF_3)_2]_2$ ($Mg(TFSI)_2$) in propylene carbonate (PC)

electrolyte. At potentials above 1.5 V vs Mg, an anodic current caused by either Mg

stripping, electrolyte oxidation or corrosion of SS current collector was observed. A

cathodic current corresponding to Mg plating was not observed. The lack of cathodic

activity is most likely due to formation of blocking layer on electrode surface, making

electrodeposition of Mg from the electrolyte impossible.

So far, reversible stripping and plating at the Mg electrode has been demonstrated

with electrolyte solutions based on highly volatile ethereal solvents such as

tetrahydrofuran (THF) and 1,2-dimethoxyethane (DME). As these are flammable

electrolytes with narrow electrochemical windows, they limit the choice of cathode for

Mg batteries and ultimately battery energy density.
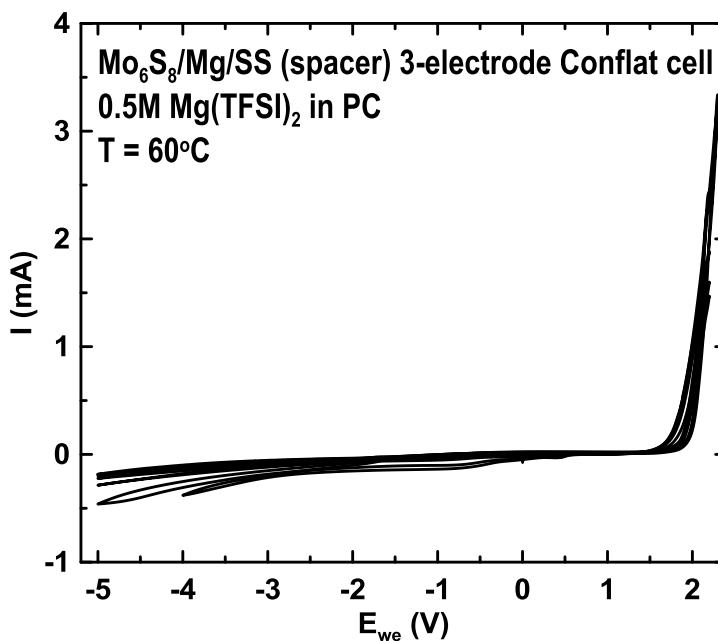
Figure 1.1: Cyclic voltammogram of a Mo_6S_8/Mg/SS (spacer) 3-electrode Conflat cell with 0.5M $Mg(TFSI)_2$ in PC at $60°C$.

3

Therefore, it is imperative that new electrode materials with high energy density and electrolyte systems be developed with broad potential windows for practical Mg battery applications. To undertake this research it is essential to have a reversible counter electrode. The Mo_6S_8 Chevrel phase compounds have shown high reversibility in Mg intercalation and have been long studied as an electrode material for Mg batteries compared to novel silicate and phosphate electrode materials.[10,11] Therefore Mo_6S_8 Chevrel phase was considered as a suitable counter electrode. In order to develop new electrode materials and electrolyte systems, a stable 3-electrode cell is required where Mg metal is used as the reference electrode. In addition, a convenient and reproducible method needs to be developed to synthesize Mo_6S_8 Chevrel that has good electrochemical characteristics. In this thesis, the above matters will be explored.

After reviewing the background of Li and Mg battery technologies as a good basis for the understanding of this thesis work, a theoretical background of the techniques and methods used are described. Chapter 4 presents a new cell hardware design based on Conflat vacuum fittings which can simply be assembled into two and three electrode cell configurations. This is particularly useful for high temperature studies and an excellent alternative to coin and Swagelok cell hardware especially in Mg battery research where the electrolyte is volatile and moderately high temperatures are used. Two and three electrode measurements of Li and Mg battery materials and further details regarding Conflat cell design are discussed in Chapter 4. This cell design was used to evaluate potential electrode materials and electrolytes for rechargeable Mg batteries in this thesis.

Chapter 5 discusses the use of Pb as an anode for rechargeable Mg batteries. It was found that Mg reversibly inserts into sputtered Pb in Grignard based electrolytes and

the electrochemical performance of this anode material is discussed in detail. Chapter 6 evaluates the electrochemistry of Mo_6S_8 Chevrel phase prepared by conventional high temperature solid state synthesis and an alternative solid state synthesis method (Spex milling method) is discussed. Chapter 7 presents the conclusions of this work. Chapter 8 presents the work in progress including the particle size optimization of Mo_6S_8 prepared by the Spex milling method and an ongoing study of potential electrolytes for Mg batteries.

CHAPTER 2   BACKGROUND ON SECONDARY METAL-ION BATTERIES

Transportation plays a key role in economics and in people's daily lives. An urge for mobility has resulted in the production of millions of vehicles all over the world. Today these vehicles are propelled by the combustion of billions of gallons of fossil fuels (gasoline or diesel) extracted from various regions on earth. Apart from the fact that fossil fuels are non-renewable, recent studies have shown that excessive usage of fossil fuels have caused adverse effects on the earth's atmosphere due to the release of combustion products, especially CO_2, which ultimately results in a rise in earth's average surface temperature.[12,13] Global warming could initiate a chain of catastrophic environmental problems. This has attracted research attention to the investigation of alternative technologies for energy storage which are environmentally friendly and cost effective.

The introduction of non-polluting vehicles would be highly desirable. In order to replace the conventional internal gasoline combustion engines, automobile manufacturers are mainly focused on two technologies: fuel cells and rechargeable batteries.[14,15] Both of these technologies are promising in terms of reducing emission of undesirable products to the environment and decreasing the dependence on gasoline. Therefore, the search for cost effective high energy density batteries is an important venture for future automobile applications.

2.1 Battery Theory

Batteries are devices capable of converting chemical energy into electrical energy via electrochemical redox reactions of the battery active materials. Redox reactions

induce electron flow through an external circuit connected to the battery, while charged ions flow from one electrode to another within the cell electrolyte. As this process continues, the active materials deplete until the battery is no longer capable of producing current. At this state the battery is said to be discharged. The basic electrochemical unit of a battery is called a cell and a battery contains one or more of these cells connected in series and/or in parallel to provide the required voltage and capacity depending on the application. Batteries are classified into two types; primary and secondary batteries. Primary batteries are also known as disposable batteries since they are based on a non-reversible electrochemical redox reaction and need to be replaced once fully discharged. These types of batteries include very common alkaline batteries and highly successful zinc/air batteries.[16] Secondary batteries partake in reversible redox reactions and by reversing the current with an external charger, the active materials can be regenerated and the battery can be recharged. Currently lithium-ion, lead-acid and nickel-metal hydride batteries are the most common rechargeable batteries that are commercially available.

2.2 Lithium Batteries

Even though the emphasis of this thesis is on magnesium batteries an introduction to Li batteries provides a good basis for the understanding of rechargeable metal ion batteries.

An electrochemical cell consists of two active electrodes; a positive electrode (cathode) and a negative electrode (anode). The electrodes are separated by an electrolyte solution containing dissociated salts, which enables ion transfer between the two electrodes. A porous membrane separator is typically used to separate the positive and negative electrodes and contain the electrolyte. The use of a separator eliminates the possibility of electric short circuit, minimizes electrolyte usage, and increases battery

7

structural integrity. Upon discharge, electrons and lithium cations flow from the anode to the cathode. The resulting current flow through the external circuit can be used for useful work. A schematic of a typical Li-ion cell is shown in Figure 2.1.
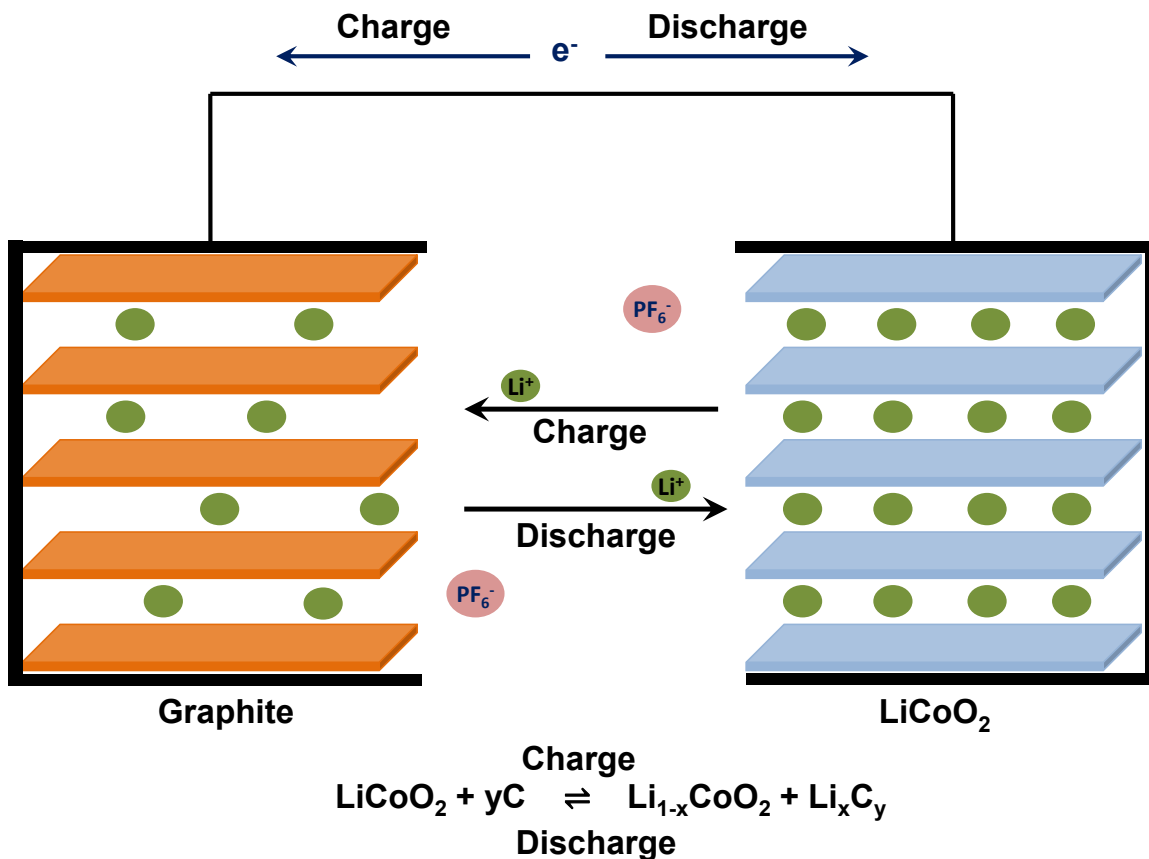
Figure 2.1: Schematic of a general Li-ion cell with graphite anode and $LiCoO_2$ cathode in $LiPF_6$ electrolyte salt.

The crystal structure of the electrode materials in a typical Li-ion cell allows reversible intercalation/deintercalation into and from the host materials. The efficiency of a charge/discharge cycle greatly depends on the reversibility of the reactions at the electrodes. In a Li-ion cell, the cathode contains Li when synthesized, and Li has low chemical potential in the cathode. The anode contains no Li after cell synthesis. Li has

high chemical potential in the anode and therefore a Li-ion cell must first be charged after construction.

2.3.1 Anode Materials

The performance of an anode material is affected by several factors, such as the voltage at which it stores Li-ions, the kinetics of electron transfer, the Li-ion storage capacity, electrode surface area and the structural integrity of the material. Li metal, carbon and alloy materials were tested as anodes for Li based batteries. Their performance, applicability and shortcomings as anode materials will be discussed next.

2.3.1.1 Lithium Metal Anode

The low molar mass and high electrode potential of lithium results in significantly high energy density for lithium metal batteries. Despite the fact that lithium metal has the highest specific energy, the attempts at commercializing rechargeable batteries containing lithium metal have failed due to the inherent instability of lithium metal and poor coulombic efficiency during cycling.

On a thermodynamic basis, lithium metal readily reacts with polar aprotic solvents, many commonly used salt anions such as ClO_4^-, PF_6^-, $N(SO_2CF_3)_2^-$, and also with atmospheric contaminants like H_2O, O_2, CO_2. Yet lithium metal is stable in many polar aprotic solvents due to the formation of electrically insulating, passivating surface film. These films are formed due to the reduction of electrolyte components by the active metal resulting in insoluble lithium salts and organic polymers on lithium surface forming SEI.[17] Nevertheless, repeated stripping and plating of lithium could be problematic owing to irregularities in the Li surface caused by uneven deposition of lithium, which could consequently lead to dendrite formation.[18–20] The resulting high surface area porous

deposits have a high reaction rate with the electrolyte. This results in safety problems, such as thermal runaway or explosions, in extreme cases, and in poor coulombic efficiencies, which make cycle life unacceptable.[21,22–24] These issues have hampered the commercialization of rechargeable Li metal based batteries.

2.3.1.2 Carbon Anode Materials

In an effort to mitigate the intrinsic instability of the lithium metal anode, most research attention shifted towards the development of Li-ion batteries in the late 1980s. In Li-ion batteries, the lithium metal anode was replaced by carbonaceous materials that were capable of reversible intercalation of lithium ions at low potentials.[24–26]

By the use of carbonaceous anodes, Li plating and dendrite formation can be eliminated, reducing the chances of battery shorting and overheating.[1] The pioneering research work of Li intercalation into graphite and other less ordered carbons such as coke was introduced by Herold et al.[27] in 1975 using a vapour transport method. Since then highly ordered graphite was found to be a good choice for the anode in rechargeable Li batteries.[17,28–30] Lithiation of graphite is an intercalation process in which Li is inserted between graphene planes. This process involves phase transitions between intercalation stages. The first intercalation stage has a stoichiometry of LiC_6 with a specific capacity of 372 mAh/g.

Today all the major Li-ion battery manufacturers use carbon anode materials such as graphite. The anode material is combined with a small percent of a polymeric binder, which assists in holding the electrode components together, and a highly conductive carbon to provide electrical conductivity throughout the coating. The mixture is then

coated on a copper current collector. Copper does not form lithium alloys and it is stable at the operating voltages of the anode.

2.3.1.3 Metal Alloy Anode

Although Li-ion batteries offer high specific energy density, the demand for greater electronic performance continues to place increasing pressure on battery storage capabilities. Since graphite/$LiCoO_2$ cells have now approached their engineering limit for energy density, ongoing research activities have focused on the development of new electrode materials to further improve the cell energy. As a result lithium alloys are being developed to replace the graphite anode. The pioneering works on Li-Al,[31,32] Li-Sn,[33,34] Li-Mg,[35] Li-Sb[36,37] and Li-Si[38,39] serves as a basis for continued research work. The Li storage capacity of alloys can decrease quickly after several charge-discharge cycles. This is due to the large volume expansion that occurs during lithiation, creating great stress on the alloy crystal lattice, and finally fracturing alloy particles.[22]

2.3.2 Cathode Materials

In order to achieve a large cell potential, and thus a large energy density, the difference between the chemical potential of lithium within the anode and cathode should be maximized. Therefore high potential intercalation compounds were needed for the cathode such as layered or three dimensional type transition metal oxides. $LiCoO_2$ was first suggested as a cathode in 1980 due to its layered structure and favourable electrochemical properties.[40,41] This is the most widely used cathode material in commercial Li-ion batteries due to its high energy density and good cycle life. Because Co is expensive, most research efforts are directed towards finding a replacement for $LiCoO_2$. These replacements involve the alteration of $LiCoO_2$ stoichiometry by the

11

substitution of more abundant, inexpensive metal ions such as manganese.[30–32] Similar to preparation of the anode, the cathode material is also combined with a polymeric binder and a conductive carbon in excess solvent. The slurry is then cast on to an aluminum current collector, which is stable at the operating voltage of the cathode.[17]

2.3.4 Electrolytes

The role of liquid electrolytes in Li-ion cells is to act as an ionic conductor to transport Li-ions between the electrodes during cycling. Since the electrodes in Li-ion cells are porous, which contain an active material, a conductive material and a polymeric binder, the liquid electrolyte must permeate into the porous electrodes and transfer Li-ions efficiently at the interface between the liquid and the solid phases. Most commercial Li-ion cells utilize nonaqueous electrolyte solutions where the lithium salt is dissolved in aprotic organic solvent.

Even though graphite is an attractive anode material for Li-ion batteries, early attempts at using it as an anode failed due to the high reactivity of lithiated graphite towards the electrolyte.[44,47] When lithiated graphite cells are fabricated with PC based electrolytes, charged decomposition of PC takes place on the graphite surface. Also PC solvent molecules co-intercalate between graphene layers along with Li, thereby exfoliating the graphite particles.[48] The reactivity of these lithium intercalated carbons with electrolyte is due to their chemical potential being very close to that of metallic Li. Ethylene carbonate (EC) replaced PC as the main electrolyte component in the early 1990s and this improved the reversibility of lithiated graphite in Li-ion cell.[44,49] As EC is a solid at room temperature, it is mixed with a low viscosity solvent such as ethers, dimethyl carbonate (DMC) or diethyl carbonate (DEC) to lower the melting point and

viscosity of the solvent, and thereby increasing the ionic conductivity. An improved performance of graphite was observed with EC due to the formation of an effective passivation film on the carbon electrode surface, which permits lithium insertion and prevents co-intercalation of solvent molecules.[14,50,51]

In addition the lithium salt $LiPF_6$ dissolved in these solvents reacts with aluminum at high potentials to form a stable insoluble film which prevents further corrosion of the positive electrode current collector. Due to its high ionic conductivity $LiPF_6$ is widely used as a salt for electrolytes in Li-ion batteries; however their relatively low thermal stability and high reactivity in the presence of water make it difficult to handle.[52,53] Therefore manufacturers add various types of additives to the electrolyte to improve cycling performance and safety characteristics.

2.4 Magnesium Batteries

Two decades after the introduction of the Li-ion battery, the development of Li-ion technology has now reached an advanced state. Recently, this type of battery has been used for energy storage applications in electric vehicles by many automobile manufacturers such as Tesla and Toyota.[2,54] Compared to gasoline vehicles, the high cost, shorter operating distances and longer recharge time of electrified vehicles prevent them from being commonly used. This has led to continuous research activity on developing new cell configurations and new chemistries.

When considering sustainable supply of electrochemical energy storage devices, non-lithium battery systems such as sodium-ion (Na-ion) and magnesium (Mg) based batteries have drawn noticeable research attention over the past few years.[3,5,55–58] Theoretically, Mg based batteries are a promising technology for next generation high energy density rechargeable batteries. As shown in Figure 2.2, when metallic Mg is used

as the anode material a greater volumetric capacity can be achieved compared to graphite and Li metal[59] (3833 mAh/cc for Mg[58] vs 2062 mAh/cc for Li[58]) anodes.
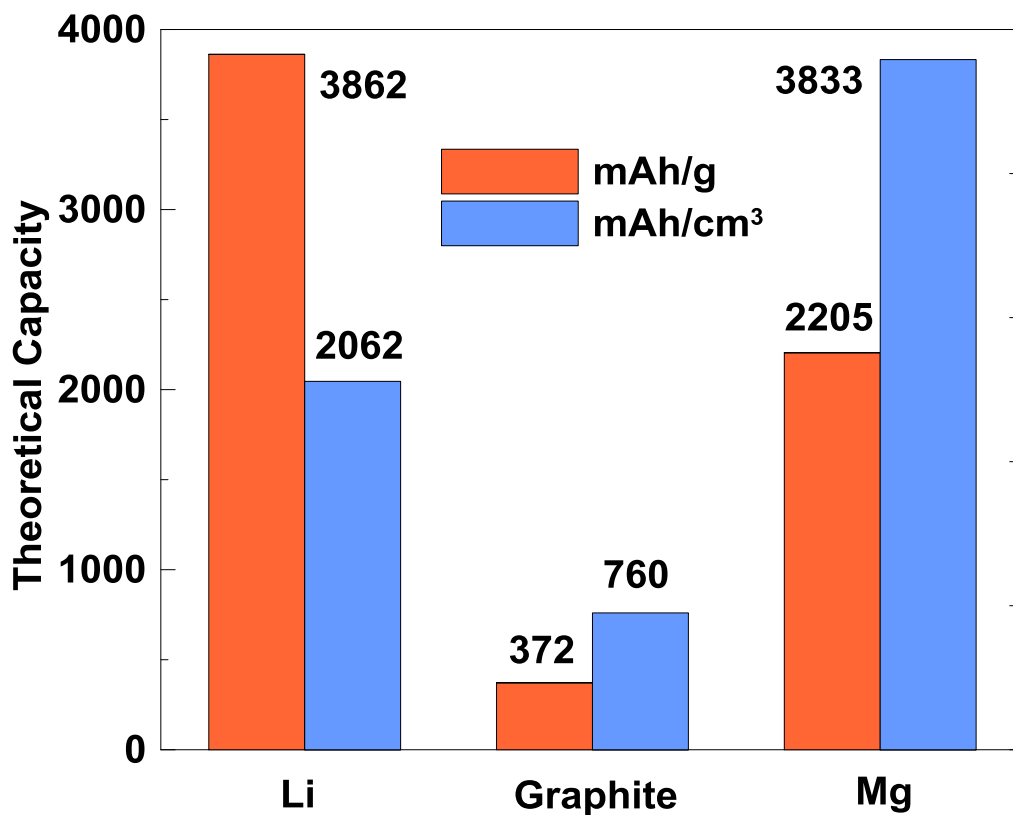
Figure 2.2: Comparison of theoretical capacities of Li metal, graphite (LiC_6) and Mg metal anodes.

In addition, compared to Li, Mg compounds are highly abundant in the earth's crust, are environmentally benign, are inexpensive, and are safe to handle.[5,9,60] Elemental abundance in the earth's crust shown in Figure 2.3 indicates the high abundance of Mg metal compared to that of Li metal.
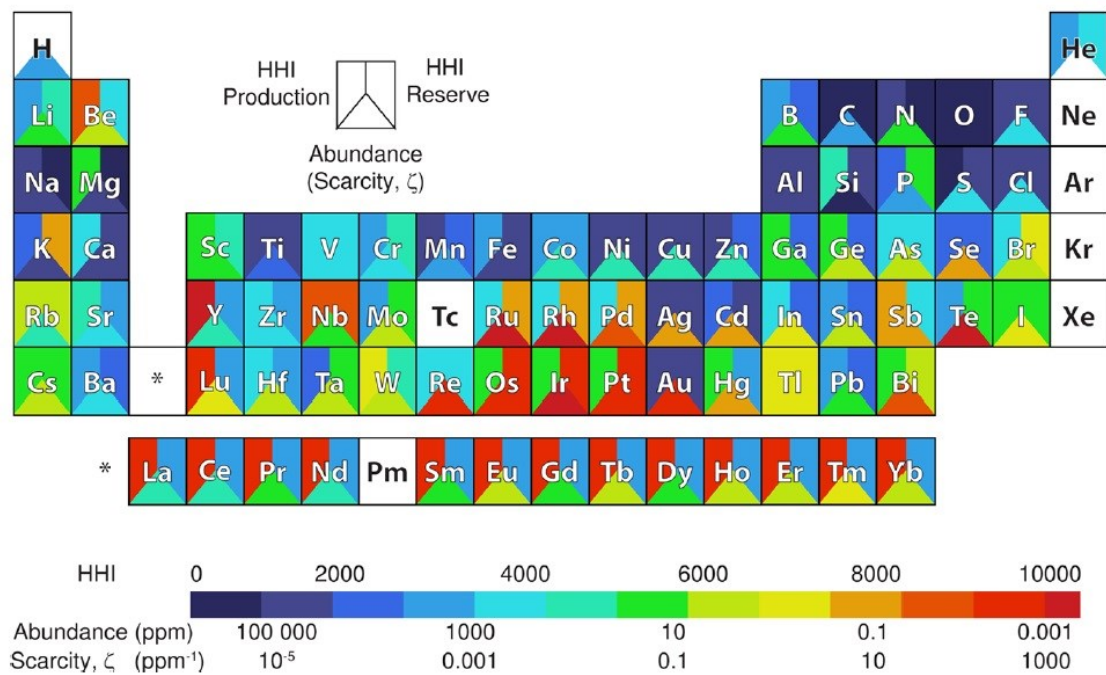
Figure 2.3: Elemental abundance and Herfindahl-Hirschman indices (HHI - production, reserve).[61]

2.4.1 Anode Materials

As mentioned above, Mg metal is a natural candidate as an anode material for secondary batteries owing to its low cost, low electrochemical potential and high volumetric and specific capacities.[62] The redox potential of the Mg/Mg^{2+} couple is 1 V higher than that of Li/Li^+ couple. It is well known that highly reversible stripping/plating of Mg metal electrodes can be obtained in organometallic magnesium salts (RMgX, R = alkyl or aryl groups and X = Cl, Br) dissolved in ethereal-based solvents such as THF[63–66] or DME.[67,68] However such electrolytes are not suitable for practical applications due to their poor oxidative stability. Aurbach et al.[5] developed a family of electrolyte solutions based on magnesium organohaloaluminate salts in ethereal solvents which exhibited an improved stability towards oxidation and reversible stripping and plating of Mg. This

15

breakthrough greatly promoted the development of rechargeable Mg batteries. However, it would be desirable to use non-volatile electrolytes with low flammability for the development of practical Mg batteries.

To overcome this problem, alloys have been suggested as negative electrode materials.[69] Singh et al. have reported investigations of Mg batteries with Sb, Sn and Bi anodes.[70,71] Bi has shown the best cycling capability, with over 100 cycles with low capacity fade. On the other hand, Sb showed only ~55% of capacity retention upon cycling. This behaviour was suggested to be due to greater iconicity and bond strength of Mg-metal in Mg_3Sb_3 than that of Mg_3Bi_2. The greater bond strength has a significant impact on the electrochemical Mg^{2+} extraction properties. Even though electrochemical studies are still required, theoretical studies of Mg insertion in Si and Ge have shown that they can be considered as anode materials capable of providing comparable capacities and larger volumetric energy densities compared to those for Li batteries.[72] This thesis also presents the electrochemical performance of Mg_2Pb, which was found to be the highest energy density Mg alloy yet reported.

2.4.2 Cathode Materials

The operation of cathodes in rechargeable Mg batteries could be based on either insertion or conversion mechanisms. Insertion electrodes involve an intercalation phenomenon where Mg^{2+} ions are reversibly inserted and extracted from a solid matrix, without disturbing its crystal structure. Conversion electrodes do not rely on an intercalation mechanism. During the conversion reactions the structure of the host changes. The divalent nature of Mg^{2+} ions makes intercalation fundamentally difficult and complex. Cathode materials based on inorganic transition metal oxides, sulfides and

borides have been tested for Mg^{2+} ion intercalation. Novák et al. compared the experimental potential ranges for reversible cycling of electrodes based on different materials.[6] They showed that sulfide based electrodes usually have insertion potentials close to 2 V vs Li/Li^+. Oxide based electrodes usually insert both Mg^{2+} and Li^+ in a potential between 3 to 4.5 V vs Li/Li^+. Studies on intercalation of Mg^{2+} into several materials such as Co_3O_4, V_2O_5, ZrS_2, TiS_2, NiS_2, FeS_2 have demonstrated the existence of compounds that can insert magnesium reversibly.[73–75] None of the above compounds were found to be suitable as practical cathode materials for rechargeable Mg batteries due to several shortcomings. Many transition metal oxides and sulfides have undesirable characteristics such as incompatibility with electrolyte solutions used for Mg batteries,[9] very low Mg insertion kinetics,[76,77] and pronounced capacity fade during cycling.[75,78]

Unlike the above transition metal oxides and sulfides, Mo_6S_8 has relatively fast Mg^{2+} intercalation kinetics, making it an excellent host material into which Mg^{2+} ions can be reversibly intercalated. Aurbach et al. first introduced Mo_6S_8 as a cathode material in a prototype system for rechargeable Mg batteries and it was successfully cycled with electrolyte solutions based on magnesium organohaloaluminate salt ($(Mg(AlCl_2BuEt)_2)$) in THF, achieving nearly 100% coulombic efficiency.[5] The crystal structure of the $Mg_xMo_6S_8$ cathode can be considered as a stacking of Mo_6S_8 blocks. Each block contains an octahedral cluster of molybdenum atoms inside a cube of sulfur atoms. As shown in Figure 2.4, the sites for Mg atoms are located in the channels between each of the two blocks. There are 12 possible sites for guest atoms but only some of these can be occupied simultaneously due to electrostatic repulsions and geometrical hindrance. Usually guest atoms are weakly bound to these sites and are capable of diffusion without

17

an electric field, even at room temperature. This allows the high mobility of intercalated ions, resulting in reversible intercalation.[79]
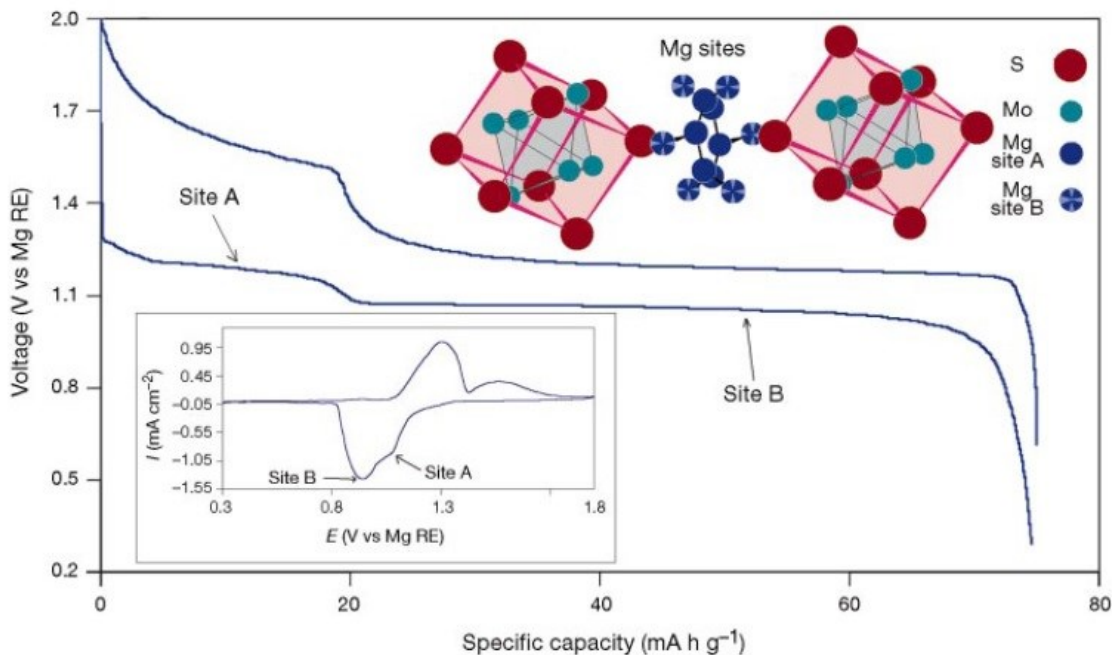
Figure 2.4: Electrochemical behaviour and the basic crystal structure of $Mg_xMo_6S_8$ cathode (0 < x < 1) with 0.25M $Mg(AlCl_2BuEt)_2$ in THF. Inset: Cyclic voltammogram of steady state Mg insertion and deinsertion.[5]

Although Mo_6S_8 Chevrel phase cathode materials provide much better kinetics compared to other oxides and sulphides, there are some aspects of Mo_6S_8 Chevrel that require further development. For example Mg diffusion in Mo_6S_8 Chevrel phase is strongly affected by composition and temperature. At ambient temperature, the selenide (Se) shows excellent Mg mobility in the full intercalation range from zero to two Mg^{2+} ions per formula unit,[80] while partial charge trapping of Mg ions occurs in the sulphide. During the first magnesiation of Mo_6S_8, two Mg^{2+} ions are inserted, achieving full theoretical capacity, 128 mAh/g, but upon electrochemical deintercalation 20-25% of the

first magnesiation capacity is irreversible due to Mg-ion trapping. The trapped ions can be fully deintercalated at elevated temperatures (60°C).[81]

Despite the kinetic advantage of selenide Chevrel phase, the lower specific energy (88.8 mAh/g) limits its practical usage. The high cost and low energy of Mo_6S_8 Chevrel limit their usage in practical Mg batteries.[5,82] Therefore further research attention has been dedicated to develop new cathode materials with high energy densities.

In 1990 Gregory et al. showed that ethereal solutions of magnesium boroalkyl or aryl solutions ($Mg(BR)_2$, R = alkyl or aryl group) can be compatible with Mg insertion compounds such as Mg_xCoO_y.[9] The results presented for the above system are not likely to be practical in terms of long term cyclability and reversibility. Recently, attempts have been taken to investigate the applicability of $MgCo_2O_4$, $Mg_{0.67}Ni_{1.33}O_2$ and $MgNiO_2$ as cathode materials with $Mg(ClO_4)_2$ in acetonitrile solutions using Mg as the negative electrode.[83] These active materials possess high potentials as cathode materials. Nevertheless, they are still far from practical use due to the lack of electrolytes with appropriate electrochemical windows or proper anode materials to circumvent the passivation problem of the Mg metal anode. In addition Sutto et al. investigated RuO_2 as a cathode material in ionic liquid for Mg batteries due to its remarkable performance as a cathode material in Li-ion batteries.[84–86] However, it was discovered that there are significant structural changes upon intercalation of Mg^{2+} ions due to the strong binding of Mg^{2+} with oxide in the lattice of RuO_2.[87]

Conversion cathodes inherently possess higher theoretical volumetric capacities than insertion cathodes. As an example, sulfur has a high theoretical capacity of 3459 mAh/cm^3 and is of great interest when coupled with a Mg metal anode. The theoretical

volumetric energy density of Mg/S battery system exceeds 4500 Wh/l, which is approximately twice the volumetric energy density of a Li-ion battery composed of a graphite anode and a cobalt oxide cathode.[58] The reaction of S with Mg can only occur in a non-nucleophilic electrolyte due to the electrophilic nature of S. Unfortunately, the magnesium organohaloaluminate electrolytes reported so far are nucleophilic and therefore preclude the use of S electrodes. This also shows the necessity of investigating new electrolyte systems compatible with Mg.

Another attractive cathode is oxygen contained in the air. The Mg/air system has a theoretical voltage of 2.93 V vs Mg and a volumetric energy density of 14046 Wh/l.[88] Despite its high energy density, this system is not yet practical due to the absence of moisture/air stable electrolytes. Therefore research efforts are still required to develop successful cathode materials as well as compatible electrolytes for Mg based batteries.

2.4.3 Electrolytes

As mentioned earlier, in most of the commonly used polar aprotic solvents, Mg reacts with the electrolyte components, forming a surface film which is electronically and ionically insulating. Thus Mg deposition is impossible in these electrolyte systems. Jolieois et al.[89] and Gregory et al.[9] showed that Mg electrodes are not passivated in ethereal solutions containing Grignard reagents. In the latter study they synthesized an electrolyte comprising $Mg[B(C_4H_9)_4]_2$ from the reaction between dibutylmagnesium and the Lewis acid tri-n-butylborane. This electrolyte which showed improved anionic stability over Grignard reagents, but poor coulombic efficiencies. In addition, they couldn't be used in batteries owing to their poor oxidative stability, which limits the

choice of available cathodes. Based on their study, it was assumed that the Lewis acid could be the determining factor in improving the voltage stability.

Depending on this hypothesis, a breakthrough was made by Aurbach et al. with the introduction of a family of electrolytes based on Mg organohaloaluminate salts $Mg(AlCl_{4-n}R_n)_2$ (where R = alkyl or aryl groups) in ethereal solvents.[5] The optimized compositions, $Mg(AlCl_2BuEt)_2$ complex (first generation electrolytes)[5] and the $AlCl_3$-$(PhMgCl_2)$ complex (second generation),[90] have improved electrochemical stability (2.4 V and 3.3 V vs Mg reference electrode, respectively). Outstanding electrochemical performance has been achieved for Mg/Mo_6S_8 in these electrolytes, yielding nearly 100% coulombic efficiency.[91,92] However, the above proposed electrolyte systems still suffer from practical point of view such as safety and environmental compatibility. In addition, nucleophilicity and sensitivity towards air/moisture preclude their potential applications in Mg/S and Mg/air batteries.

In search of inert polar aprotic solutions suitable for reversible Mg electrochemistry with wide electrochemical windows, ionic liquids appear to be promising candidates. After extensive investigation of potential ionic liquid electrolyte systems, Aurbach et al. showed that derivatives of imidazolium salts, some of the most commonly used ionic liquids, were reactive with Mg.[78] In other systems in which Mg was stable, unavoidable passivation films were developed due to the possible reactions of Mg with traces of moisture or other contaminants. Recently, Doe et al. reported an inorganic magnesium salt synthesized by the acid-base reaction of $MgCl_2$ and $AlCl_3$ in a variety of solvents, including ethereal solutions such as THF, DME and higher glymes such as tetragylmes, as shown below (reaction 2.2):

$$mMgCl_2 + nAlCl_3 \quad \rightleftharpoons \quad Mg_mAl_nCl_{[(2*m)+(3*n)]} \tag{2.1}$$

This salt showed 99% coulombic efficiency upon Mg deposition and dissolution in ethereal based solvents, low overpotential (< 200 mV) for Mg deposition, and good anodic stability of 3.1 V vs Mg/Mg^{2+}.[67] Liao et al. presented a synthetic strategy to enhance the oxidation stability of oxygenated species of modified Grignard reagents by replacing phenolate with alkoxide. Mg/Mo_6S_8 batteries in complexes of alkoxides based on Mg salts with $AlCl_3$ (1:6, $AlCl_3$: ROMgCl) displayed good cycling and rate performance at both $20^\circ C$ and $50^\circ C$.[93] Very recently, Young et al. proposed a new class of electrolytes based on $Mg(TFSI)_2$ dissolved in glyme-based solvents with unique characteristics, such as highly reduced corrosive nature towards current collectors, high anodic limit, high solvating capability, and the ability to form an appropriate solvation sheath structure for reversible Mg stripping/deposition.[94] $Mg(TFSI)_2$ dissolved in glyme/diglyme has shown excellent anodic stability, exceeding 4.0 V with aluminum current collectors.

With all the recent improvements, more research attention is devoted towards developing electrolyte systems with low vapour pressure and non-flammability for practical battery applications. All these advances in electrolyte systems contribute to the search for better cathode materials with the promise of further improvement in the electrochemical performance of rechargeable Mg batteries

CHAPTER 3   EXPERIMENTAL TECHNIQUES

3.1 X-ray Diffraction

      X-radiation comprises electromagnetic waves whose frequency lies between ultraviolet light and gamma rays in the electromagnetic spectrum. X-rays are generated in a sealed vacuum tube by the interaction of high energy electrons with a heavy metal target such as tungsten (W) or copper (Cu). When a high voltage (several tens of kV) is applied between the cathode (wire filament) and the anode (metallic target), high energy electrons are emitted from the cathode and are accelerated towards the anode. When electrons bombard atoms in the metal target, they can eject an electron from the core electron shell. An electron from a higher energy level drops down immediately to fill the vacancy, emitting an X-ray with a sharply defined energy associated with the energy difference between the initial and final states of the electron. These are known as characteristic X-rays that produce line spectra with discrete energies. A common type of X-ray used for crystallography is Cu Kα radiation, which corresponds to the transition of an electron from L shell (2p) to K shell (1s).

      The radiation produced from a Cu target includes Cu $K\alpha_1$, $K\alpha_2$ and K_β as the highest energy X-rays and a whole set of lower energy radiation. K_β radiation corresponds to the electron transition from M (3p) to K shell. Due to spin orbit coupling, two energy levels exist within the Cu L subshell known as $2p_{1/2}$ (L_2) and $2p_{3/2}$ (L_3), which causes transitions with slightly different energies. The $K\alpha_1$ radiation results from an electron transition from L_3 to K level, which corresponds to an 8.048 keV energy difference and a photon with a wavelength of 1.5405 Å.[95] The $K\alpha_2$ transition from L_2 to K shell corresponds to a photon with 8.028 keV energy and 1.5443 Å wavelength.[95] Due to

high intensity of $K\alpha_1$ radiation compared to $K\alpha_2$ and K_β radiation ($K\alpha_1$: $K\alpha_2$: $K_\beta = 10:5:2$), resulting from the double degeneracy of the $2p_{3/2}$, $K\alpha_1$ is more desirable for X-ray diffraction (XRD). The K_β and other low energy radiation are generally removed by a filter or a monochromator. The similarity in the wavelengths of $K\alpha_1$ and $K\alpha_2$ radiation makes it difficult to separate them with a monochromator.

Once X-rays leave the X-ray tube, they pass through various slits arranged parallel to the path of the X-ray beam. These are used to control the width of the incident beam so that it is confined within the area of the specimen and to restrict the width of the beam entering the detector. Interaction of X-rays with the sample electrons scatters the radiation and creates a secondary diffracted beam. Since the wavelengths of these X-rays are of the same order of magnitude as interatomic distances, diffraction patterns can be observed due to constructive and destructive interferences of X-rays scattered from the sample. The condition for constructive interference is given by the mathematical relation "Bragg's Law":

$$n\lambda = 2d \ \sin\theta, \qquad\qquad (3.1)$$

where n is an integer corresponding to the order of reflection, λ is the X-ray wavelength, d is the interplanar atomic spacing and θ is the diffraction angle. When the difference between the distances travelled by the diffracted X-ray beam from adjacent crystal planes equals to an integer multiple of its wavelength, the diffracted photons will be in phase. The amplitudes of their electromagnetic waves will add, resulting in constructive interference, thereby increasing radiation intensity. When the difference between the distances travelled by the photons diffracted from adjacent crystal planes equals to an

integer multiple of half the wavelength, the scattered photons will be out of phase, resulting in destructive interference.
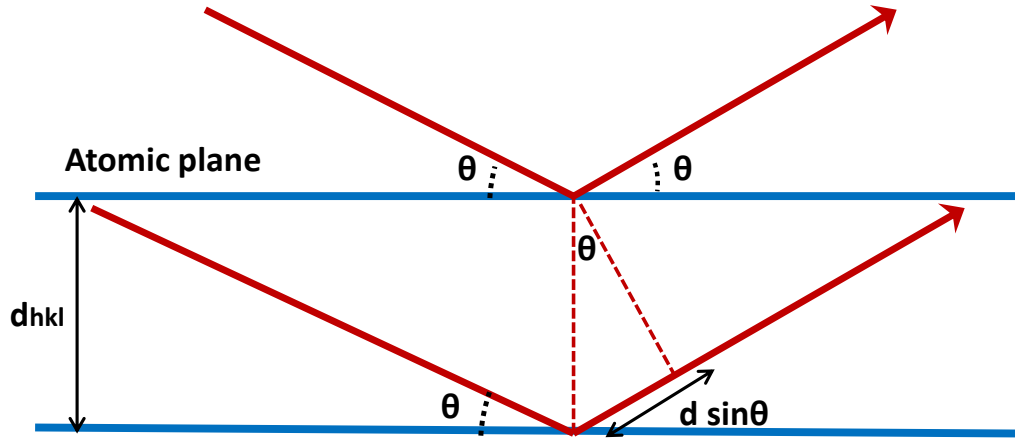
Figure 3.1: Bragg scattering from crystalline planes in a solid.

X-ray data are often recorded in terms of scattering angle (2θ, abscissa) and intensity of scattered radiation (ordinate). Depending on the diffracted X-ray peak positions, the dimensions of the elementary cell, including the d-spacing of the lattice planes, can be calculated from the Bragg's law. The intensity of each diffraction peak is related to the crystallographic structure of the material. It provides information regarding the content of the unit cell such as the position of the atoms within the elementary cell. In addition, crystallite size of the sample material can be derived using the Scherrer equation:

$$FWHM = \frac{K\lambda}{\beta cos\theta} \qquad (3.2)$$

where FWHM is full width at half maximum of the X-ray diffraction peak, K is a dimensionless crystallite shape factor equal to 0.9, λ is the X-ray wavelength, β is the crystallite size perpendicular to the plane defined by Miller indices of the peak and θ is the diffraction angle.

For most samples, the aim of XRD analysis is to identify the crystalline phases present. Phase identification is accomplished by comparing the peak positions and relative intensities from the specimen with a standard data base. This can be performed by using software programs, such as Match!.[96] To extract precise structural information, including lattice constants, atom positions and site occupations, the experimental XRD pattern can be fit to a calculated pattern based on trial crystal structures by Rietveld refinement. Rietveld refinement can be performed by software programmes such as Reitica.[97]

3.1.1 Sample Preparation

XRD measurements of both air sensitive and air stable samples were taken by a Rigaku Ultima IV diffractometer equipped with a Cu Kα radiation source and a scintillation detector with a graphite diffracted beam monochromator. A filament current of 40 mA and an accelerating voltage of 45 kV were used to generate X-rays. For X-ray measurements, non-air sensitive powder was packed into a 25 mm x 20 mm x 3 mm sample well in a stainless steel plate and pressed flat with a glass slide to ensure uniform surface, and thereby minimize zero-offset corrections. As shown in Figure 3.2, air sensitive powder was packed in the same way into a custom designed sample stage equipped with an aluminized Mylar window, which was sealed under an inert atmosphere to avoid contact with air. Ex-situ XRD measurements for sputtered disc electrode, described in Chapter 5, were taken in the latter sample stage, where the disc was adhered onto the zero background holder (silicon wafer) using a double sided tape under argon atmosphere.
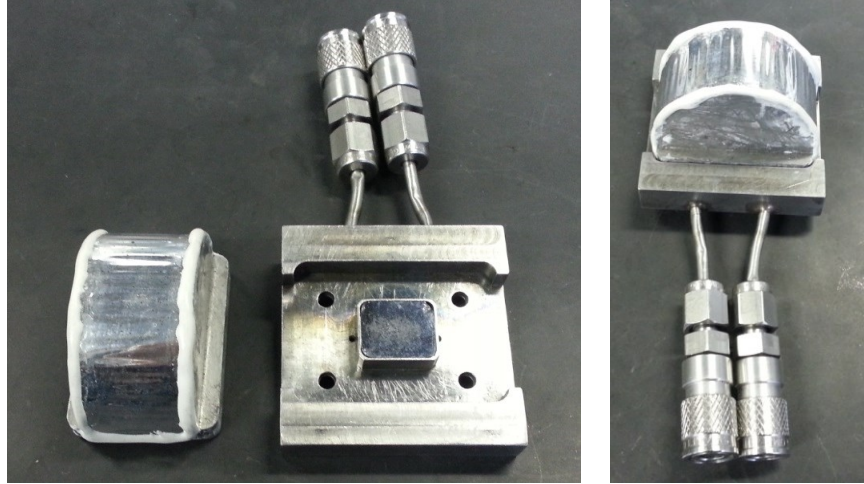
Figure 3.2: X-ray holder for air sensitive samples with the zero background holder.

3.2 Scanning Electron Microscopy (SEM)

Scanning electron microscopy (SEM) is a commonly used technique for investigating bulk specimens at the microscopic level. When an acceleration potential (0.1 keV to 50 keV) is applied between the electrodes, a beam of electrons produced by either a thermionic field emission cathode or an electron gun is accelerated towards the sample specimen. This beam travels under vacuum through an electromagnetic field, thereby focusing the beam onto a small spot on the sample. Once the accelerated electron beam bombards the sample, secondary electrons, back scattered electrons and Auger electrons are ejected from the sample atoms.

Secondary electrons are generated by inelastic collisions of high energy electrons with the valence electrons of atoms in the specimen. After undergoing additional scattering events while travelling through the specimen, some of these ejected electrons emerge from the surface of the specimen. Most of the secondary electrons usually fall in an energy range between 2 to 5 eV. Backscattered electrons are produced by elastic interactions of electrons with the nuclei of the atoms in the specimen. The fraction of

incident electrons that is backscattered strongly depends on the atomic number of the scattering atom and directly affects the brightness of the image. The de-excitation energy released from an electron can be transferred to another atomic electron, which leaves the specimen resulting in Auger electron. Secondary and Auger electrons are susceptible to elastic and inelastic scattering and can only leave the specimen from a very thin surface layer. They are however generated not only by the primary beam of high energy electrons but also by the backscattered electrons on their way back through a larger region of the surface.

The electrons ejected from the sample are recorded by detectors in the SEM and the resulting signal is converted into an image.

3.2.1 Sample Preparation

In this thesis work all the SEM measurements were taken on a Hitachi Cold field Emission SEM S-4700, which has a magnification range of 30× to 500k×. The accelerating voltage of this model SEM can be as low as 500 V, making it very useful for samples that are sensitive to electron beam damage, and to obtain more surface details with improved resolution. SEM samples were firmly mounted in an organic matrix containing finely ground silver flakes on a stainless steel sample holder. An acceleration voltage of 10 kV and an emission current of 15.5 μA were used in these measurements.

3.3 Electrode Fabrication

In this study, thin film electrodes made by sputter deposition and composite electrodes made from powdered materials were used. Sputtered lead (Pb) film electrodes were fabricated for the electrochemical study of magnesiated lead in Chapter 5. Composite electrodes were fabricated for measurements performed on Pb, $Li_4Ti_5O_{12}$

(LTO), LiFePO$_4$ (LFP), graphite (MAGE) and Mo$_6$S$_8$ Chevrel phase compounds (Chapters 4-8).

Composite electrode preparation consisted of mixing active material with a binder and a conductive diluent. The binders used were poly(vinylidene fluoride) (PVDF, HSV 900, KYNAR) or LiPAA (made by neutralizing PAA solution (Sigma-Aldrich, average molecular weight ~250,000 g/mole, 35 wt% in H$_2$O) with LiOH ·H$_2$O (Sigma Aldrich, 98%) in distilled water). The conductive diluent used was Super P carbon black (SP, EraChem, Europe). The active material, conductive diluent, binder, and a binder soluble solvent (n-methylpyrrolidone (NMP, Aldrich) for PVDF and distilled water for LiPAA) were mixed in a Retsch PM 200 planetary mill at 120 rpm with two 0.5" tungsten carbide (WC) balls for 1 hour. Pb composite electrodes were made from 80 wt% Pb powder (~325 mesh, 99%, Sigma Aldrich), 10 wt% PVDF and 10 wt% SP. LFP (Hydro Quebec) electrodes were composed of 86 wt% LFP, 7 wt% PVDF and 7 wt% SP. LTO (Nanomyte BE-10, NEI Corporation) electrodes were composed 88 wt.% LTO, 6 wt.% PVDF and 6 wt.% SP. Graphite electrodes were composed of 88 wt.% MAGE (Hitachi, average size of 20 μm), 10 wt.% LiPAA and 2 wt.% SP. Mo$_6$S$_8$ electrodes were composed of 80 wt% Mo$_6$S$_8$, 10 wt% PVDF and 10 wt% SP. Electrodes were cast from NMP slurries onto Al or stainless steel foil for LTO and LFP electrodes, Cu foil for MAGE electrodes and stainless steel foil for Mo$_6$S$_8$ and Pb electrodes. The electrodes were then air dried at 120°C for 2 hours.

Sputtering is not a commercially favoured method to fabricate electrodes as it is expensive and energy intensive. It is difficult to prepare composite electrode coatings with heavy metals such as Pb due to their large particle size and density, which causes Pb

29

powder to settle out of the coating dispersion. For this reason, sputtered Pb film electrodes were used. Unlike the composite electrodes, sputtered electrodes do not contain polymer binders or carbon based conducting diluents that could complicate the electrochemical behaviour of the active material.

Pb was sputter deposited onto 13 mm stainless steel (SS) foil discs using a modified Corona Vacuum Coater V-3T deposition system. A base pressure of 7.6 x 10^{-7} Torr with a 3.1 mTorr argon pressure and a 35W target power was used during the deposition process. The SS discs were weighed before and after sputtering using a Satorius SE-2 microbalance (±0.1 μg resolution) in order to determine the mass of the sputtered Pb film. The average thickness of the sputtered Pb film was 0.24 μm. After sputtering, the discs were transferred immediately into an argon filled glovebox to minimize the oxidation of Pb. The average electrode loading of composite Pb electrode was 2.4 mg/cm^2.

3.4 Electrochemical Methods

3.4.1 Cyclic Voltammetry

Cyclic voltammetry (CV) is an electroanalytical technique based on varying the applied potential at the working electrode in both positive (anodic) and negative (cathodic) directions at a particular scan rate while monitoring the current. In this work CV was used to analyse two aspects of various electrolyte systems at different temperatures: (1) capability and reversibility of Mg stripping/deposition on stainless steel current collector and (2) the electrolyte electrochemical window. In order to study these phenomena, a 3-electrode cell, including a working electrode (WE), a counter electrode (CE) and a reference electrode (RE) was used.

Here a 3-electrode Conflat cell was designed and used for most electrochemical tests. This cell is discussed in greater detail in Chapter 4. For CV measurements the Conflat cell configuration consisted of a stainless steel WE, a Mg metal RE, and either a Mg metal or a magnesiated Mo_6S_8 CE. In CV technique, the voltage of WE vs. CE is scanned linearly across the potential range of interest at a predetermined scan rate measured in volts/second. A scan rate of 5 mV/s and a selected potential window within the range of 5 V to -5 V were used in this study. The current response from the applied potential is then recorded as a function of applied potential while varying the temperature. All the CV measurements were taken using a SP-300 potentiostat (Bio Logic Science Instruments).

The notation used here for identifying the WE, CE and RE configuration in 2-electrode cells is CE/WE and CE/RE/WE in 3-electrode cells. In full 2 or 3-electrode cells the notation is: anode/cathode or anode/reference/cathode.

31

3.4.2 Electrochemistry

Electrochemical performance of potential electrode materials and electrolyte systems were analysed to determine their applicability in practical applications. Factors determining electrode materials' or electrolytes' commercial eligibility, including their operational potential window, capacity, energy density, rate capability and cycle life, can be measured electrochemically. This section will explain the thermodynamics behind the electrochemical response of battery materials and electrolytes and the useful parameters that can be collected from electrochemical studies.

As shown in Figure 2.1, a typical 2-electrode electrochemical cell used in this work consists of an anode and a cathode separated by an electrically insulating separator soaked in an electrolyte solution. According to the terminology used here, the anode is defined as the electrode where oxidation occurs during cell discharge and the cathode is the electrode at which reduction takes place during cell discharge. The cell potential of a typical metal-ion cell can be determined in volts by the following equation 3.2:

$$E = -\frac{(\mu_{cathode} - \mu_{anode})}{ne} \qquad (3.2)$$

In this equation $\mu_{cathode}$ and μ_{anode} are the chemical potentials in electronvolts (eV) of the metal-ion in the cathode and anode, respectively, n is the number of active electrons per metal-ion and e is the charge of an electron. In this thesis work, electrochemical measurements were taken in both 2 and 3-electrode full cells and half cells. In half-cells the WE comprises the active material of interest and is cycled versus a corresponding CE/RE electrode such as Li or Mg metal. When using a half-cell, the measured cell potential may also include the polarization from the metal CE/RE. As long as the impedance on the CE/RE is small, it is approximated that all the changes in the measured

32

half-cell potential occur only as a result of the changes in chemical potential of WE. When using a 3-electrode cell, the contribution of polarization to the measured cell potential can be eliminated, thereby more accurate results can be achieved. This is especially important when investigating potential electrode materials and/or electrolyte solutions for Mg batteries, as Mg metal is a blocking electrode in most electrolytes, which results in large polarization.

Using the common convention, cell capacity is expressed here in terms of ampere-hours (Ah). The gravimetric capacity of a cell is determined by the amount of active material in the electrode and is expressed in units of mAh/g. Volumetric capacities are measured in either mAh/cm^3 or Ah/L. Cycling currents are usually expressed as a "C-rate", which is the capacity of the cell in Ah divided by the number of hours desired to complete a half-cycle.

Typically, cycling data of a cell is displayed as a voltage curve, where measured potential is plotted versus the working electrode's gravimetric capacity. The features in a voltage curve such as hysteresis, polarization, voltage plateaus, reversible and irreversible capacities correspond to the changes in chemical potential of the metal-ions in host electrode. In the voltage profile of Mg/Mo_6S_8 half-cell, shown in Figure 3.3, most of these features are illustrated.
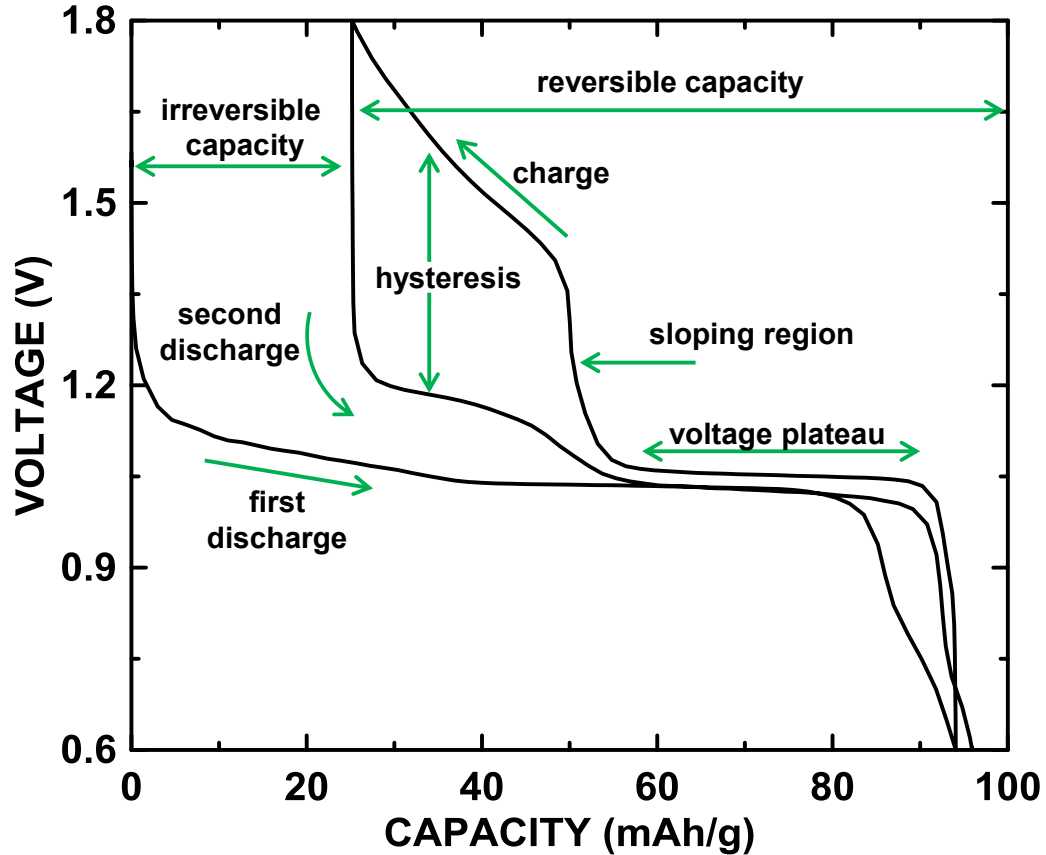
Figure 3.3: The voltage curve of a Mg/Mo_6S_8 half-cell cycled at C/20 rate at 60°C.

In the above voltage curve, two plateaus are representative of a two-step discharge and charge process. This indicates a change in the reaction mechanism and potential of the active material. As shown above, the upper voltage plateau has a higher hysteresis than the lower voltage plateau resulting in a significant slope at a potential of 1.4 V vs Mg. Plateaus in a voltage curve typically occur when two-phase regions are encountered in the active metal-host electrode phase system. Sloping regions in the voltage curve are usually indicative of single phase regions.

The irreversible capacity of a voltage curve is defined as the capacity loss between the first discharged cycle and the immediate charge cycle. As stated in the literature the initial capacity loss of a Mo_6S_8 vs. Mg cell at room temperature is due to the

incomplete Mg deintercalation caused by poor diffusion kinetics of the active material.[80] However, at elevated temperatures complete Mg extraction can be observed.[5] Therefore in the above voltage curve, the resulting irreversible capacity is suspected to be due to either larger particle size of the active material or by side reactions. The side reactions may include surface deactivation by oxidation or formation of non-reversible reaction products by the interaction of uncontrollable trace impurities in the electrolyte solution.

Charge transfer kinetics involves ion diffusion through the electrolyte, desolvation of ions at the electrode surface and diffusion through the electrode, where each step adds some resistance to the overall reaction. Therefore an additional electromotive force has to be applied to overcome this resistance. This is known as the overpotential. As a result, the electrode potential deviates from the equilibrium potential giving rise to a polarization. Hysteresis is a phenomenon which is path dependent and can be explained in terms of activation energy. The hysteresis of Mo_6S_8 electrode is exhibited as a difference between the equilibrium potential between charge and discharge curves. A path independent variable, such as a change in crystal structure or a phase transition during cycling, can cause hysteresis.

Electrochemical cells in this work were made either in custom made 2-electrode and/or 3-electrode Conflat cells. Typical 2325 coin type cells were also fabricated for comparison purposes of electrochemical results obtained by the new Conflat cell design. A detailed description of the coin type cell and Conflat cell design and their performance can be found in Chapter 4. All the cells fabricated in this thesis were cycled under thermostatically controlled conditions ($\pm$ 0.1°C) using a Maccor Series 4000 Automated Test System (Maccor Inc., Tulsa OK).

CHAPTER 4   CONFLAT TWO AND THREE ELECTRODE

ELECTROCHEMICAL CELLS

4.1 Introduction

Coin or Swagelok cells are the most commonly used hardware for testing metal ion battery materials. A typical coin cell construction is shown in Figure 4.1. Coin cells are excellent test vehicles for new electrode materials, as they are simple and quick to make and are reproducible.[98] However, the thin metal cell casing can easily distort, making even stack pressure difficult to achieve. In addition, the use of coin cells is challenging at high temperatures ($\geq 80^{\circ}$C), especially in the presence of highly volatile solvents such as tetrahydrofuran (THF). Above about 60°C we have found that coin cells containing THF based electrolytes typically leak or break open due to the softening of the polyethylene gasket coupled with high internal pressures.
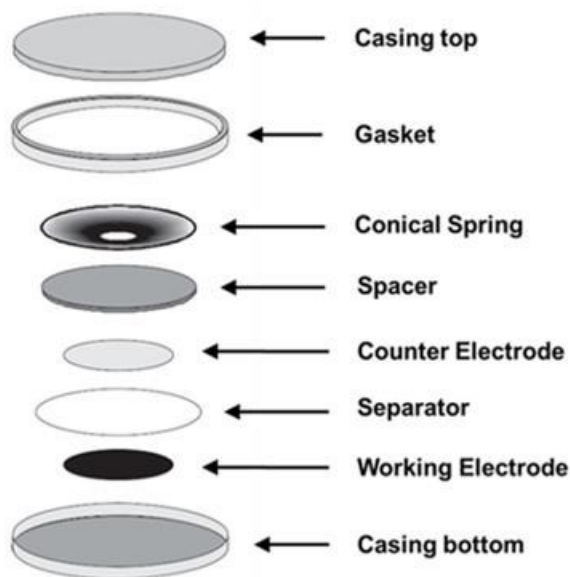

Figure 4.1: Schematic drawing of a 2-electrode coin cell.

Three electrode coin cells have been described in which contact to the third electrode is provided by a wire that passes through a small hole made in the side of the cell can. The hole is then sealed with an epoxy resin.[69,99] Such cells are extremely difficult to construct and have a high failure rate. We have found that they are not compatible with electrolytes containing volatile solvents (e.g. THF based electrolytes used in Mg batteries, for instance) since the resulting internal pressure causes leaks in the epoxy resin before it can harden.

Swagelok cells are constructed in a polytetrafluoroethylene (PTFE) or stainless steel union fitting using two metallic plungers as current collectors that are usually made of stainless steel or aluminum, depending on the electrode operating potential.[9,76,100,101] They are easy to adapt to 3-electrode cells by replacing the union fitting with a 'T' and adding a third plunger.[102] A stainless steel coil spring is typically used to provide stack pressure. The plungers are held in place and the cells are sealed by swaging the plungers with PTFE ferrules. The space around the electrodes in Swagelok cells is restricted. This can make electrode alignment difficult.[103,104] Furthermore any PTFE cell parts exposed to low voltage will react with lithium and convert to a black conductive carbonaceous substance, as will be shown below. This reaction may affect the coulombic efficiency of Swagelok cells and can eventually cause internal short circuits.

Custom-made 2 and 3 electrode cells for metal ion battery research are also available to purchase from a number of sources. They can be very expensive and often contain elastomeric or PTFE seals. Elastomeric seals typically swell when in contact with battery electrolytes. PTFE o-rings are non-elastomeric and therefore a hermetic seal is

more difficult to achieve. They also can react at low lithium potentials, as mentioned above.

In order to conduct Mg battery research we required 3-electrode cells with volatile solvents that can operate at high temperatures. We found that suitable cell hardware does not exist that satisfied our requirements research, especially at internal pressures and high temperatures. Here a new cell design based on Conflat cell fittings is described that is simple to construct into reliable 2 and 3 electrode cells. Such cells were found to perform reliably at temperatures up to 200°C.

4.2 Experimental

Standard 2.125" (53.18 mm) stainless steel Conflat vacuum fittings were purchased from Nor-Cal Products, Inc., Yreka, CA USA. Modifications to the fittings were made by DPM Solutions Inc. of Hebbville, NS Canada. These included drilling a 5/32" (3.97 mm) hole into the rim of each fitting to a depth of 0.5" (12.7 mm) to be used as female terminals for banana jack connectors. Double-sided Conflat fittings were provided with eight ¼-28 threaded bolt holes (4 tapped holes are standard for 2.125" fittings). Teflon and HDPE sheet and tube stock were purchased from McMaster-Carr of Aurora, OH. Gaskets were punched from sheet stock using a press and circular cutting dies. Coin cells were constructed from 2325 coin cell hardware. Cell assembly was performed in an argon-filled glovebox.

Counter electrodes (18 mm diameter circles) and reference electrodes were punched from Li foil (99.9%, 0.38 mm thick, Sigma Aldrich) or Mg foil (99.95%, 0.25 mm thick, Gallium Source, LLC, Scotts Valley, CA). Working electrodes were 16 mm circles punched from coated foils. LFP, LTO, MAGE and Mo_6S_8 (synthesized as

described in reference[69]) composite electrode coatings were prepared as described in Section 3.4.

For cells cycled at 60°C or less, two layers of Celgard 2300 with a layer of polyethylene blown microfiber (BMF, 3M Company) in between were used as the cell separator. The BMF provides a compliant layer, which improves stack pressure distribution. Glass filter paper (25 mm diameter, GF/F, Whatman), dried at 400°C was used as the separator for cells cycled at temperatures above 60°C. 1M $LiPF_6$ in 1:2 EC:DEC (1:2 v/v, < 50 ppm H_2O, BASF) or 1M Lithium bis(trifluoromethanesulfonyl)imide (TFSI) (HQ-115A, 3M) in PC (< 50 ppm H_2O, BASF) electrolyte was used in lithium cells. When the latter electrolyte was used all electrodes and separators were wetted by submersing them in electrolyte and then applying a vacuum momentarily.

An electrolyte solution of 0.5 M $Mg(TFSI)_2$ in acetonitrile (ACN, 99.8% anhydrous, Sigma Aldrich) was used in Mg cells. The $Mg(TFSI)_2$ was synthesized according to the following procedure. 90.10 g of $H-N(SO_2CF_3)_2$ (55.5 wt. % aqueous solution, 3M Company) was added drop wise by an addition funnel into a 3-neck flask containing 4.00 g of pure magnesium strips (99.95%, 0.25 mm thick, Gallium Source, LLC, Scotts Valley, CA) in 37.5 g of deionized water under argon flow with magnetic stirring. After all the imide acid solution was added the reaction solution was heated at 90°C for 2 hours using a heating mantle and the temperature of the solution was measured by a thermocouple. After 2 hours the reaction solution was basic indicating that the reaction of the imide acid with excess Mg was completed. After the reaction mixture was cooled down to room temperature it was centrifuged to remove any insoluble Mg fines.

The resulted solution was concentrated by heating at 110°C under argon flow. The concentrate was immediately transferred to a Pyrex crystallizing dish and evaporated to dryness at 170°C in an antechamber under vacuum overnight. The resulted dried powder was evaporated at 300°C under vacuum for few hours to purify the salt by removing any impurities present.

The notation used here for identifying the working electrode (WE), counter electrode (CE) and reference electrode (RE) configuration in 2-electrode cells is CE/WE and CE/RE/WE in 3-electrode cells. In full 2 or 3-electrode cells the notation is: anode/cathode or anode/reference/cathode. Mo_6S_8/Mg/Mo_6S_8 3-electrode Conflat cells were prepared with 0.5 M $Mg(TFSI)_2$ in ACN electrolyte. The Mo_6S_8 WE and CE had loadings of 0.0046 g/cm^2 and 0.0018 g/cm^2, respectively. Before the cell was operated, the CE was first fully magnesiated from the Mg RE at C/100 rate at 60°C. After this step, the WE could be cycled vs. the RE, using the CE as a reversible Mg source.

All cells were cycled under thermostatically controlled conditions ($\pm$ 0.1°C) using a Maccor Series 4000 Automated Test System. In order to cycle many 3-electrode cells while having limited access to dedicated 3-electrode channels, three electrode cells were cycled using two 2-electrode Maccor channels, as shown in Figure 4.2 (b). The cell connection of a 2-electrode Conflat cell to a Maccor channel is shown in Figure 4.2 (a).
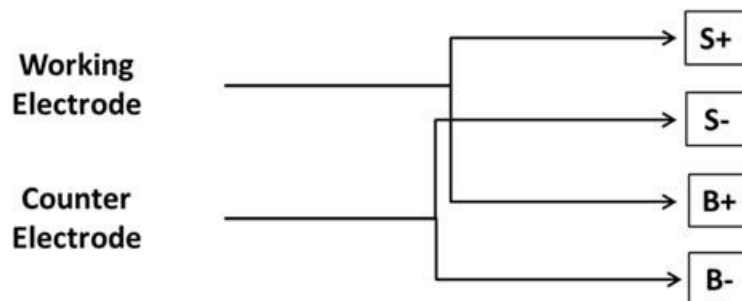
Figure 4.2 (a): A diagram showing how 2-electrode Conflat cells were connected (B = current leads, S = voltage leads).
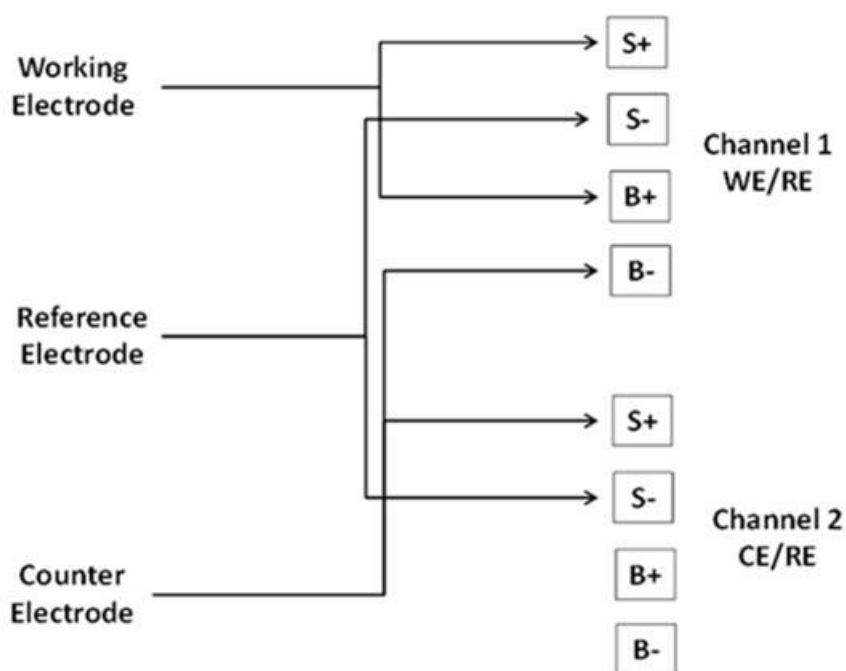

Figure 4.2 (b): A diagram showing how 3-electrode Conflat cells were connected to two 4-wire battery cycler channels. In this configuration the WE was cycled vs. the RE voltage (as measured with Channel 1), while current was provided via the CE (also connected via Channel 1). The CE vs RE voltage was monitored using Channel 2.

4.3 Results and Discussion

4.3.1 Two Electrode Conflat Cell Design

Figure 4.3(a) shows an exploded view of a 2-electrode Conflat cell and Figure 4.3(b) shows a cross section of the Conflat cell after it has been fully assembled. Typically Conflat parts are used for ultra-high vacuum fittings and seal by means of knife edges that impinge on a copper gasket. Here the copper gasket is replaced by a polymer gasket, so that the cell is sealed by the knife edges of the Conflat fitting impinging on the polymer gasket as the cell is bolted together. This is similar to the sealing mechanism that is used in a coin cell crimp seal. A PTFE insulating ring is used as a spacer, so that the top and bottom can are always separated by the same distance and that the knife edges always impinge into the gasket to the same degree when the cell bolts are tightened. The polymer gaskets are not reusable after they have been penetrated by the Conflat knife-edge; new gaskets were used for each cell. Stainless steel nuts and bolts were used to clamp the cell together. The shafts of the bolts were insulated with polyimide tape and a glass re-enforced resin was used in between the Conflat flanges and the stainless steel washers, so that they did not short circuit the cell. Alumina bolts would likely work well in this application also. The inside volume of the Conflat cell is almost identical with that of a 2325 coin cell and the same interior cell parts (spacers, spring, cell stack) used in the 2325 coin cells were used in the Conflat cells. Accordingly, 2-electrode Conflat cell assembly is almost identical to coin cell assembly.
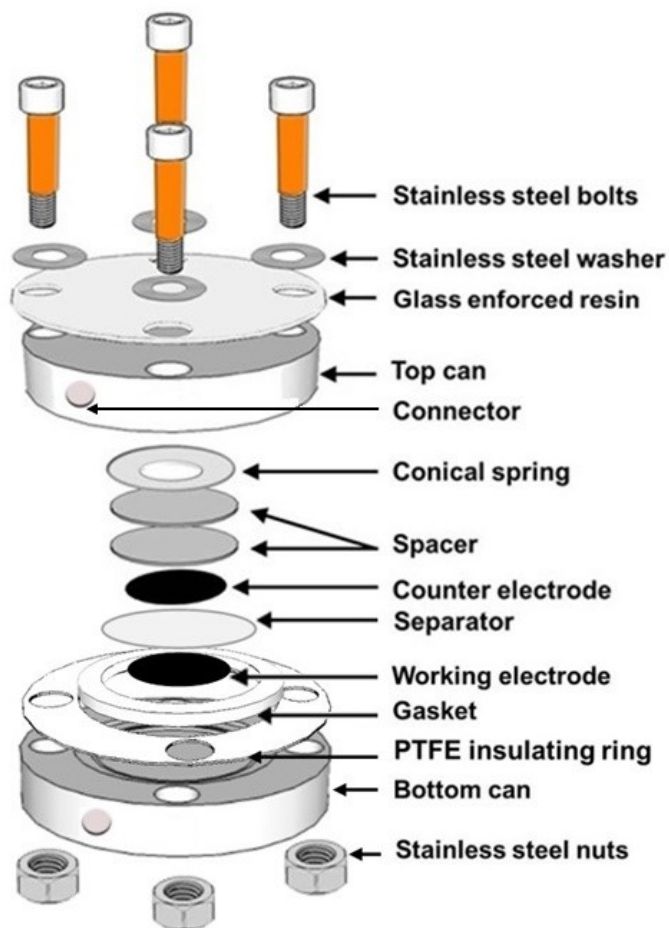
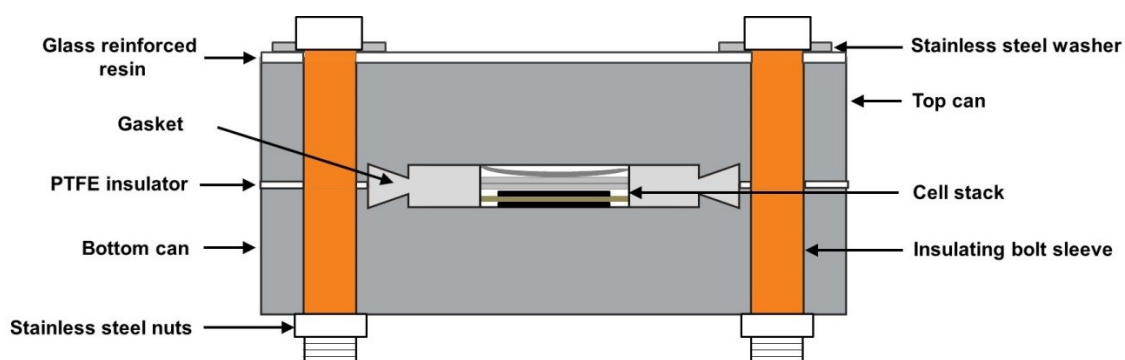Figure 4.3 (a): Exploded view of a 2-electrode Conflat cell

Figure 4.3 (b): A cross section of a fully assembled 2-electrode Conflat cell.

To test the Conflat cell seal, a well-polished piece of Li foil was sealed in a Conflat cell with an HDPE gasket and stored in humid air at 60°C for 30 days. No

noticeable change was observed in the Li foil when the cell was disassembled. Figure 4.4 (a) and (b) shows the capacity versus cycle number of a Li/MAGE 2-electrode coin cell and Conflat cell using a HDPE gasket, respectively. Both types of cells cycled nearly identically, no capacity fade in 50 cycles and with similar coulombic efficiencies (CE) of 99.8% and 99.7% for the coin cell and Conflat cell, respectively. This similarity in performance is expected since the cell stack is identical in both cells.
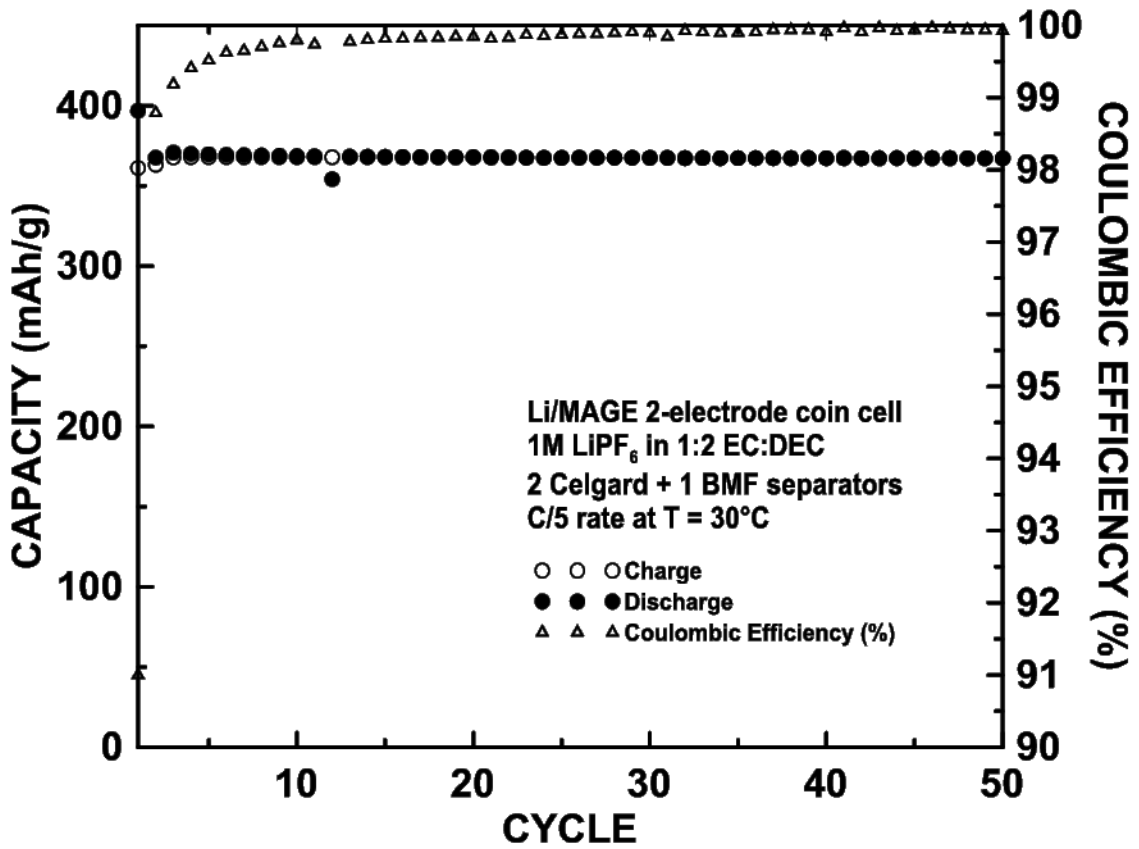

Figure 4.4 (a): Capacity versus cycle number of a Li/Mag-e 2-electrode coin cell in 1M LiPF$_6$ in 1:2 EC:DEC electrolyte at 30°C.
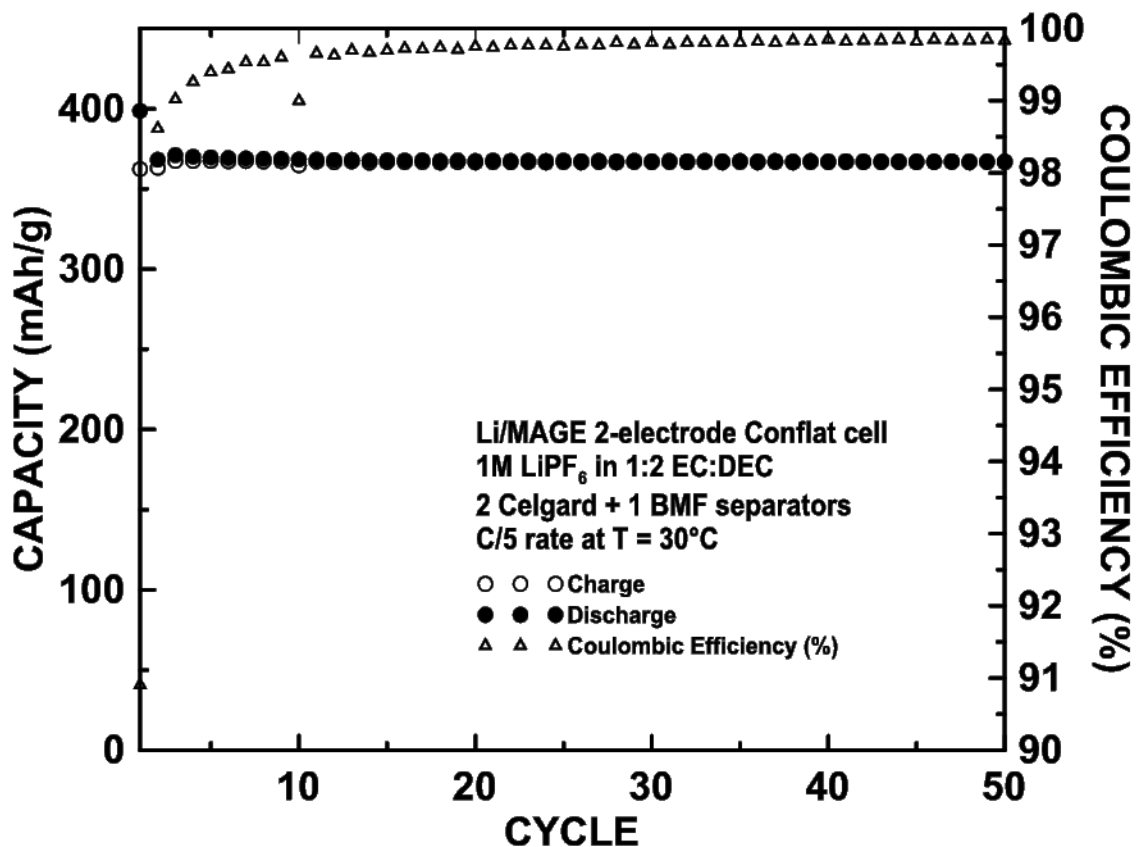
Figure 4.4 (b): Capacity versus cycle number of a Li/Mag-e 2-electrode Conflat cell in 1M LiPF$_6$ in 1:2 EC:DEC electrolyte at 30°C.

PTFE and polyimide (PI) gaskets were also found to provide a good seal. However, when PTFE or PI gaskets were exposed to Li-containing electrolytes and low voltages (< ~0.5 V), they were found to react to form carbon (and, presumably, lithium fluoride in the case of PTFE). This is demonstrated in Figure 4.5 which shows the result of using a PTFE gasket that was continually exposed to 0 V vs. Li in a Conflat LTO/Li/LFP Conflat cell. Good cycling was achieved until about 20 cycles, after which the cell failed. The PTFE gasket recovered from the cell after cycling was found to be significantly carbonized and is shown in an inset in the figure. Since the carbon that is formed by the reduction of PTFE is conductive, this reaction slowly spreads throughout the gasket, eventually causing an internal short circuit. PTFE and PI gaskets work fine at

45

higher voltages in Li cells and can be used at low voltages, if not exposed to the electrolyte (as will be shown below).
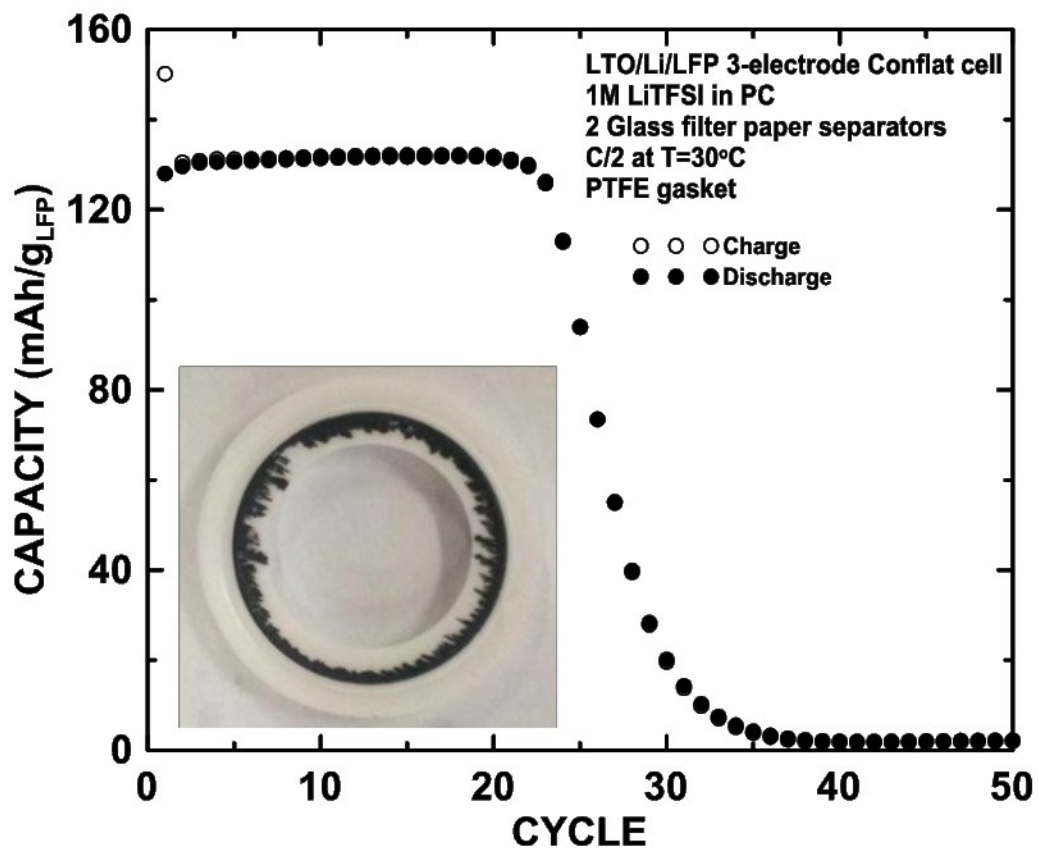

Figure 4.5: Capacity versus cycle number of a LTO/Li/LFP 3-electrode Conflat cell with a PTFE gasket. The inset shows the PTFE gasket after it was recovered from the cell.

In contrast to Li containing electrolytes, PTFE was found to be completely stable at 0 V vs. Mg in 0.5 M Mg(TFSI)$_2$ in ACN electrolyte and was also found to be stable at 0 V vs. Na in 1M NaPF$_6$ electrolyte

4.3.2 Three Electrode Conflat Cell Design

The Conflat cell design is easily adaptable to accommodate 3 or more electrodes by the addition of Conflat double-sided fittings that serve as additional electrode terminals. An exploded view of a 3-electrode Conflat cell is shown in Figure 4.6 (a). The top and bottom Conflat blank flanges of the 3-elctrode cell are the same as in the 2-electrode cell and act as the WE and CE cell terminals. A center double-sided Conflat fitting with eight ¼-28 threaded holes is the RE terminal. These threaded holes accept the bolts from the top and bottom flanges. The cell stack is confined between two steel spacers and an insulating cylinder. The RE can be a wire in the middle of the cell stack or a ring on the outside of the stack (as shown). A stainless steel ring with tab is used as a current collector for ring-type REs. Electrical connection to the RE is made via the tab which is sandwiched between the insulating cylinder and the middle Conflat fitting. In this 3-electrode cell design pressure is applied to the cell stack via an internal spring. A photograph of a fully assembled 3-electrode Conflat cell is shown in Figure 4.6(b).
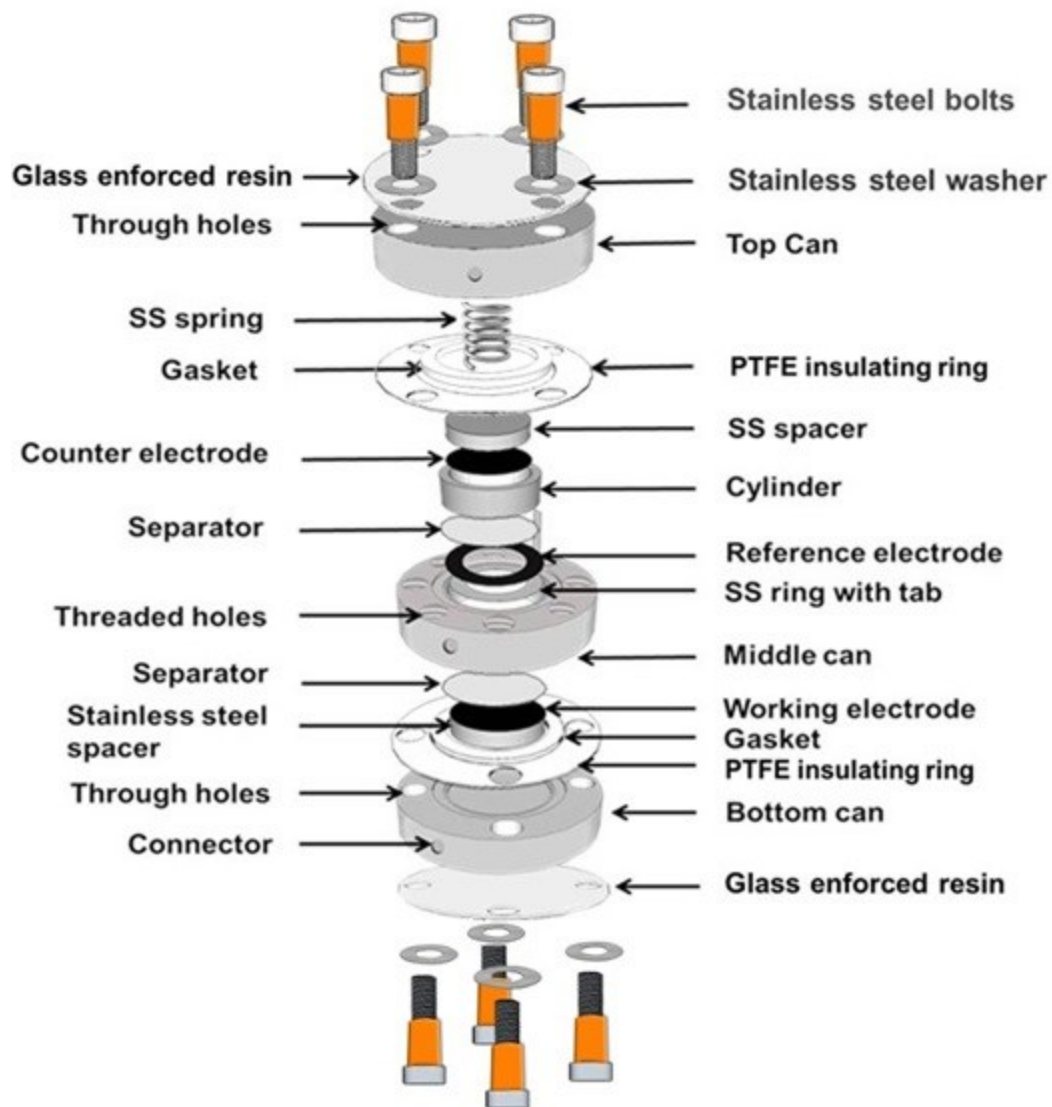
47

Figure 4.6 (a): Exploded view of a 3-electrode Conflat cell.

Figure 4.6 (b): A photograph of a fully assembled 3-electrode Conflat cell.

Figure 4.7 shows the Li RE vs MAGE WE and Li CE vs Li RE voltage curves of a Li/Li /MAGE 3-electrode Conflat cell. As expected, the Li CE vs Li RE voltage curve shows the small polarization from the stripping and plating of Li on the CE during cycling. The capacity versus cycle number and CE of this cell is shown in Figure 4.8. The performance is similar to that of a 2-electrode coin cell; with no fade after 50 cycles. The CE of this cell is excellent and was measured to be 100%, within the error of the Maccor charger. A 3-electrode Li/Li/MAGE coin cell was constructed for comparison. The cell had identical electrochemical performance. However, the 3-electrode coin cell was much more difficult to prepare. Three electrode Conflat cells were easy to construct and had a near 100% success rate.

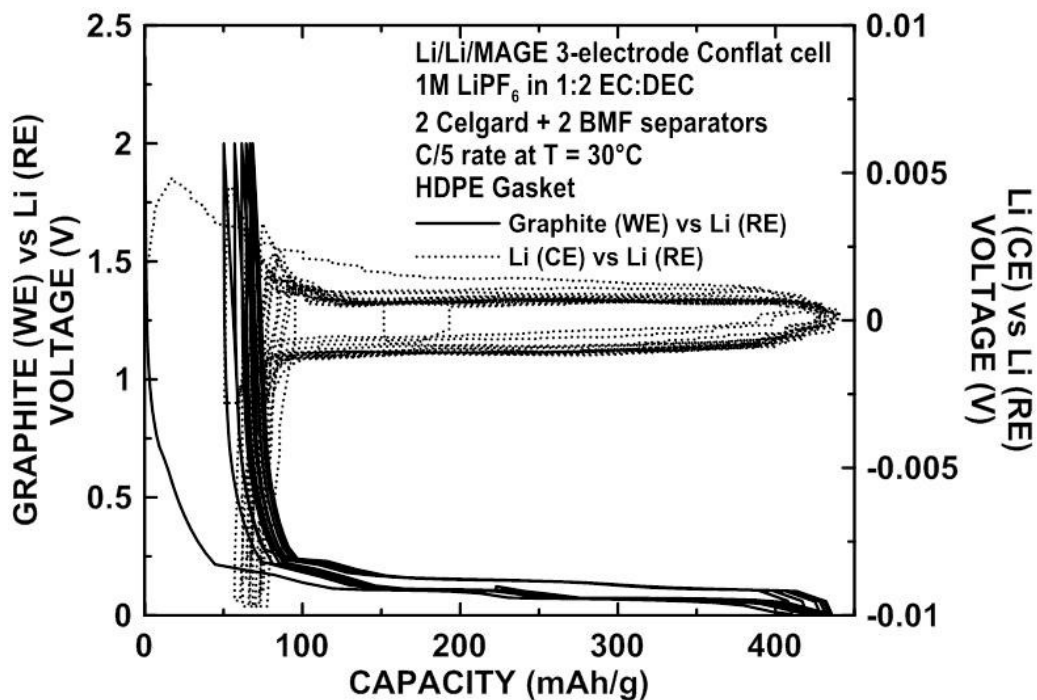Figure 4.7: Voltage curves of a Li/Li/MAGE 3-electrode Conflat cell with 1M LiPF$_6$ in 1:2 EC:DEC electrolyte at 30°C.
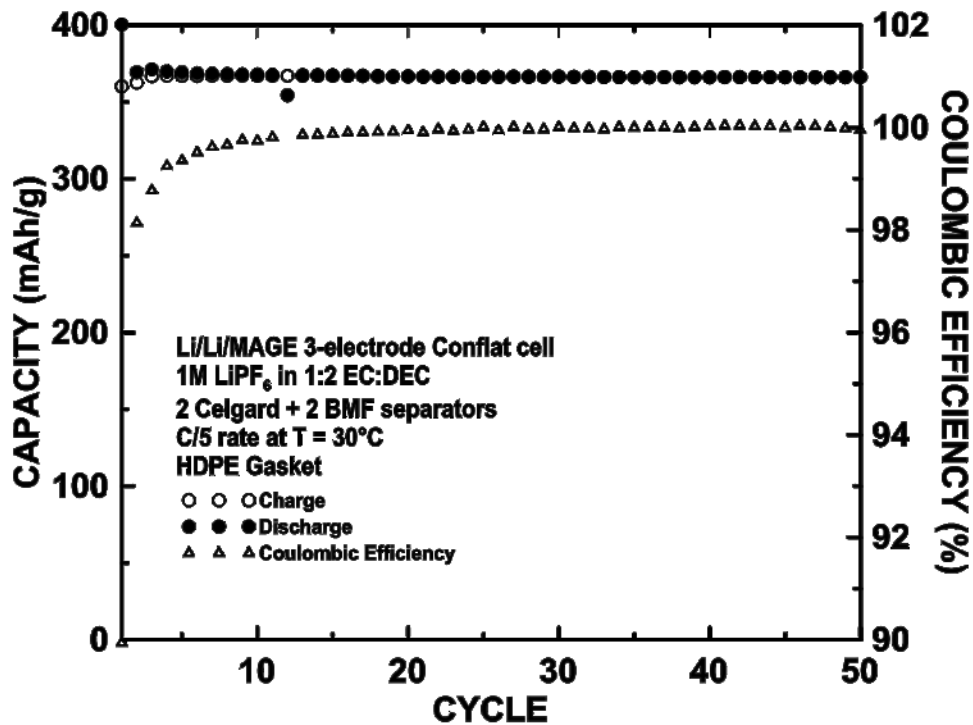

Figure 4.8: Cycling performance of a Li/Li/MAGE 3-electrode Conflat cell with 1M LiPF$_6$ in 1:2 EC:DEC electrolyte at 30°C.

4.3.3 Three Electrode Lithium-ion Conflat Cells

Lithium ion cells cycle well in 3-electrode Conflat cells, allowing the state of charge of each electrode to be observed independently and identify sources of fade. For instance, Figure 4.9 shows the Li (RE) vs LFP (WE) and Li (RE) vs LTO (CE) voltage curves of a LTO/Li/LFP 3-electrode Conflat cell. No fade was observed in this cell in 40 cycles, as is shown in Figure 4.10. This cell had a CE of ~99.5%, which is typically considered to be a high value. However in a full cell this CE can lead to very noticeable cell fade. Reactivity of LFP in this electrolyte system has not been thoroughly investigated. Another possible cause of lower CE in full cells is the alignment of the electrodes. In commercial full cells, the negative electrode is larger than the positive electrode, to allow for alignment errors. Here both electrodes are exactly the same size.

Electrode slippage of the positive electrode, shown in Figure 7, due to the imperfect CE is causing the cell to become out of balance. Though the cell initially was voltage limited by the cathode during charging, it has become voltage limited by the anode by cycle 40. This cell is expected to lose capacity if cycled further. Such insight is difficult to obtain from 2-electrode measurements only.

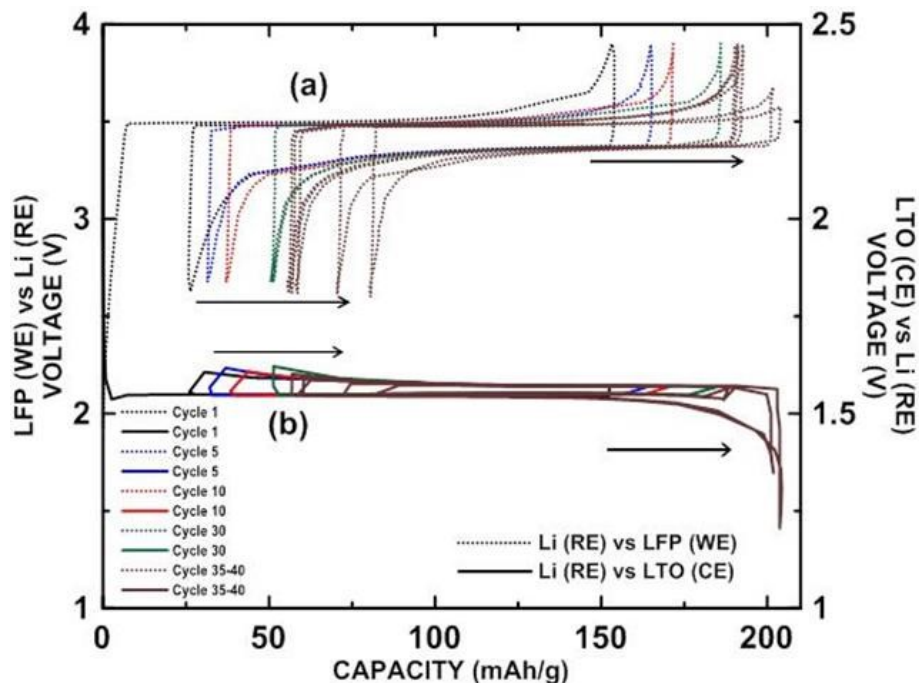Figure 4.9: Voltage vs capacity curves of a LTO/Li/LFP 3-electrode Conflat cell with 1M LiTFSI in PC electrolyte at C/2 rate, 30°C: (a) Li (RE) vs LFP (WE), (b) Li (CE) vs LTO (CE). (arrows indicate the direction of slippage of the charge/discharge end points)
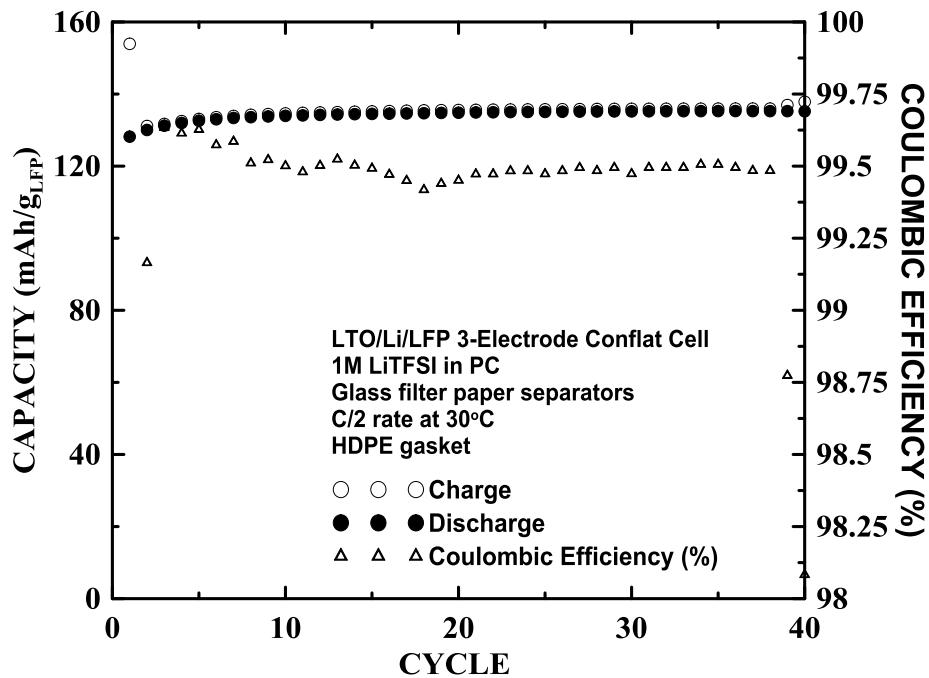

Figure 4.10: Capacity vs cycle number of a LTO/Li/LFP 3-electrode Conflat cell with 1M LiTFSI in PC electrolyte, C/2 rate, at 30°C.

52

4.3.4 Applications in Mg-Battery Research

Mg is a blocking electrode in most conventional nonaqueous battery electrolytes[59,105] and therefore it is not a suitable counter electrode in these electrolytes. Mo_6S_8 has been shown to be a reversible electrode in Mg-ion cells[5,79,106] and it was found that Mo_6S_8 can be used successfully as a reversible counter electrode in 3-electrode cells. This enables the development of new electrode materials in high voltage solvents. As an example, Mo_6S_8 vs Mg cells with ACN-based electrolyte have only been cycled a couple of times in coin cells.[69] Subsequently, ACN decomposition at the Mg electrode caused the cell to fail. In order to more effectively test Mo_6S_8 cycling performance in different electrolytes $MgMo_6S_8/Mg/Mo_6S_8$ 3-electrode Conflat cells were constructed. These cells were first constructed as $Mo_6S_8/Mg/Mo_6S_8$ cells in which the Mo_6S_8 CE had a significantly greater loading than the Mo_6S_8 WE (0.0046 g/cm^2 and 0.0018 g/cm^2, respectively). After assembly the CE was slowly fully magnesiated by discharging it vs the Mg RE by connecting the cell to a Maccor channel as shown in Figure 4.2 (a). This step converted the cell in-situ to a $MgMo_6S_8/Mg/Mo_6S_8$ 3-electrode cell. The cell was connected to the Maccor as shown in Figure 4.2 (b) where Mo_6S_8 is the WE and $MgMo_6S_8$ is the CE and source of Mg during cycling.

Figure 4.11 shows the the Mg (RE) vs. Mo_6S_8 (WE) voltage of a $MgMo_6S_8/Mg/Mo_6S_8$ 3-electrode Conflat cell cycled at $60^{\circ}C$ with 0.5 M $Mg(TFSI)_2$ in ACN at different rates. This cell has a very low irreversible capacity ~7 mAh/g, a reversible capacity close to the theoretical capacity at slow rates and low polarization.
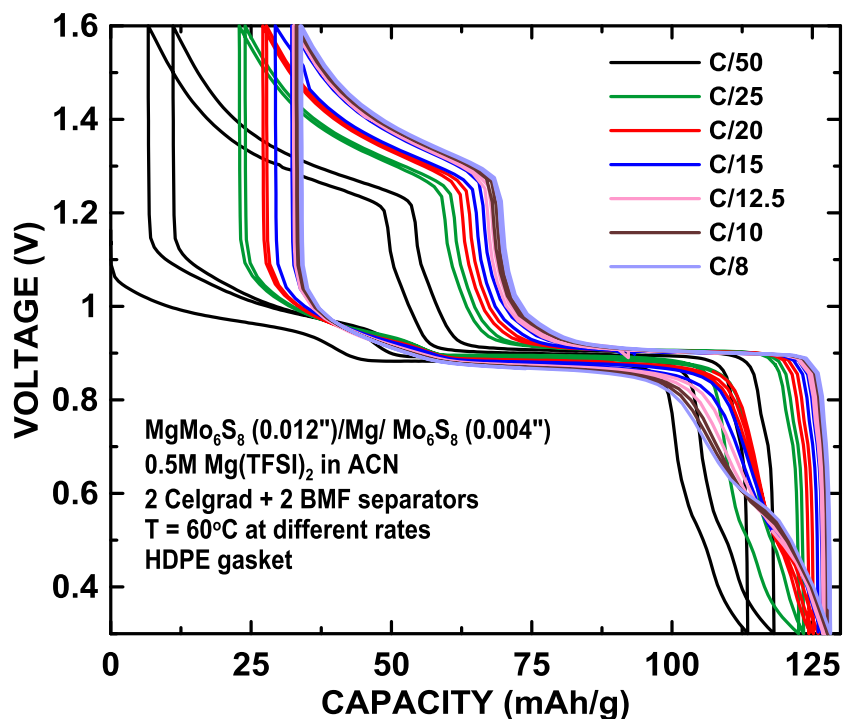
Figure 4.11: Voltage curve of a $MgMo_6S_8/Mg/Mo_6S_8$ 3-electrode Conflat cell with a HDPE gasket in 0.5M $Mg(TFSI)_2$ in ACN electrolyte cycled at 60°C at different C-rates.

Figure 4.12 shows the capacity vs. cycle number for this cell cycled at different rates. The cell showed good rate capability up to C/8, but poor coulombic efficiency at low rates, presumably because there is more time doing slow cycles for electrolyte to decompose. These results will be discussed in detail in a later publication. Here they serve to demonstrate the utility of such cells, as we have not been able to obtain such performance in two electrode cells with a Mg CE/RE. Such an experiment would not be possible in a 3-electrode coin cell, as the RE is too small to magnesiate the CE.
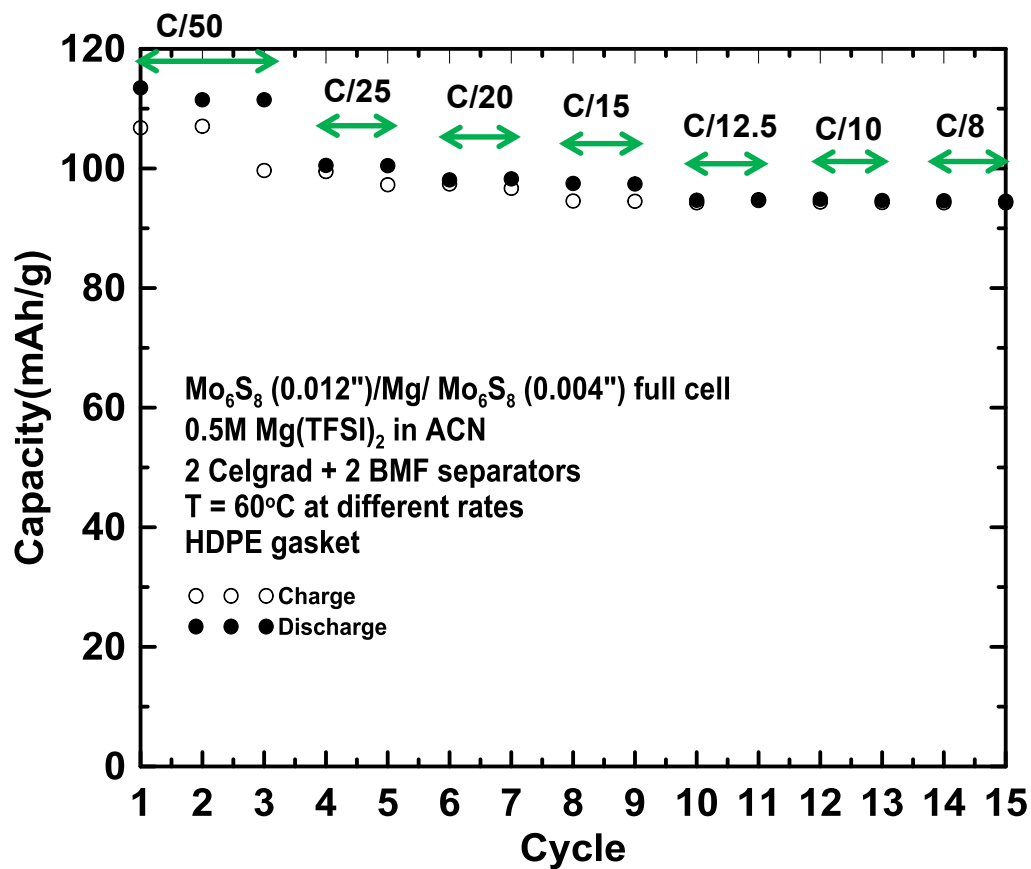
Figure 4.12: Cycling performance of a $MgMo_6S_8/Mg/Mo_6S_8$ 3-electrode Conflat cell with 0.5M $Mg(TFSI)_2$ in ACN electrolyte at 60°C.

4.3.5 High Temperature Applications

PTFE is a good gasket material at temperatures up to 200°C, however, as mentioned above, it is not stable with lithium containing electrolytes at low potentials. A modification of the basic Conflat cell design was made to cycle Li cells at high temperatures with a PTFE gasket. In order to avoid exposure of the PTFE gasket material with the electrolyte, a reservoir was made in the bottom of the Conflat cell to receive the cell stack, as shown in Figure 4.13. In this design, the PTFE gasket does not come in contact with the electrolyte and no reaction products were detected on gasket upon disassembling the cell after the experiment. This modification to standard Conflat fittings increases cell cost somewhat. It is only necessary for high temperature Li cells. At low temperatures HDPE gaskets can be used in Li cells and for Na and Mg cells PTFE gaskets can be used at both high and low temperatures, as mentioned above; for these types of cells only standard Conflat fittings are required.
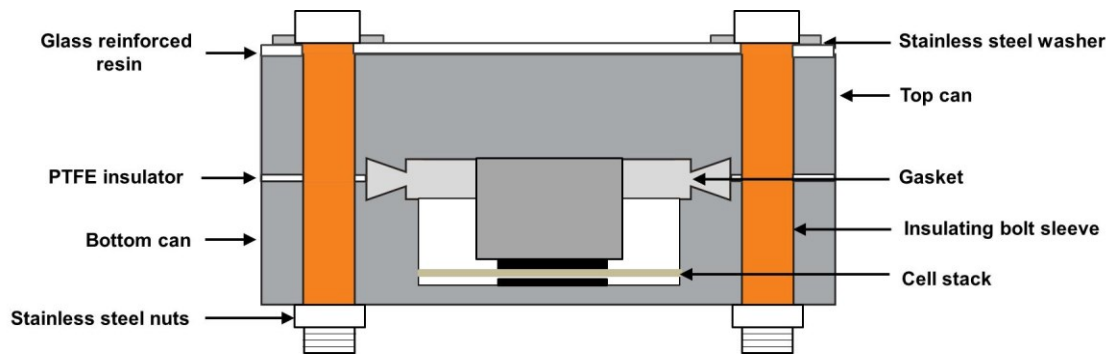
Figure 4.13: Cross section of a fully assembled high temperature 2-electrode Conflat cell.

Figure 4.14 shows the voltage curve of a Li/LTO 2-electrode Conflat cell, with a modified fitting, as shown in Figure 4.13, cycling at temperatures up to 200°C. After every ten cycles the temperature was increased by 20°C. The cell was allowed to equilibrate for 2 hours at open circuit after each the temperature increase. At temperatures above 110°C the impedance of the cell increases, presumable due to electrolyte decomposition reactions taking place at elevated temperatures, most likely at the lithium electrode.

Figure 4.14: Voltage curve of a Li/LTO 2-electrode Conflat cell with 1M LiTFSI in PC electrolyte at different temperatures, as indicated in the figure.

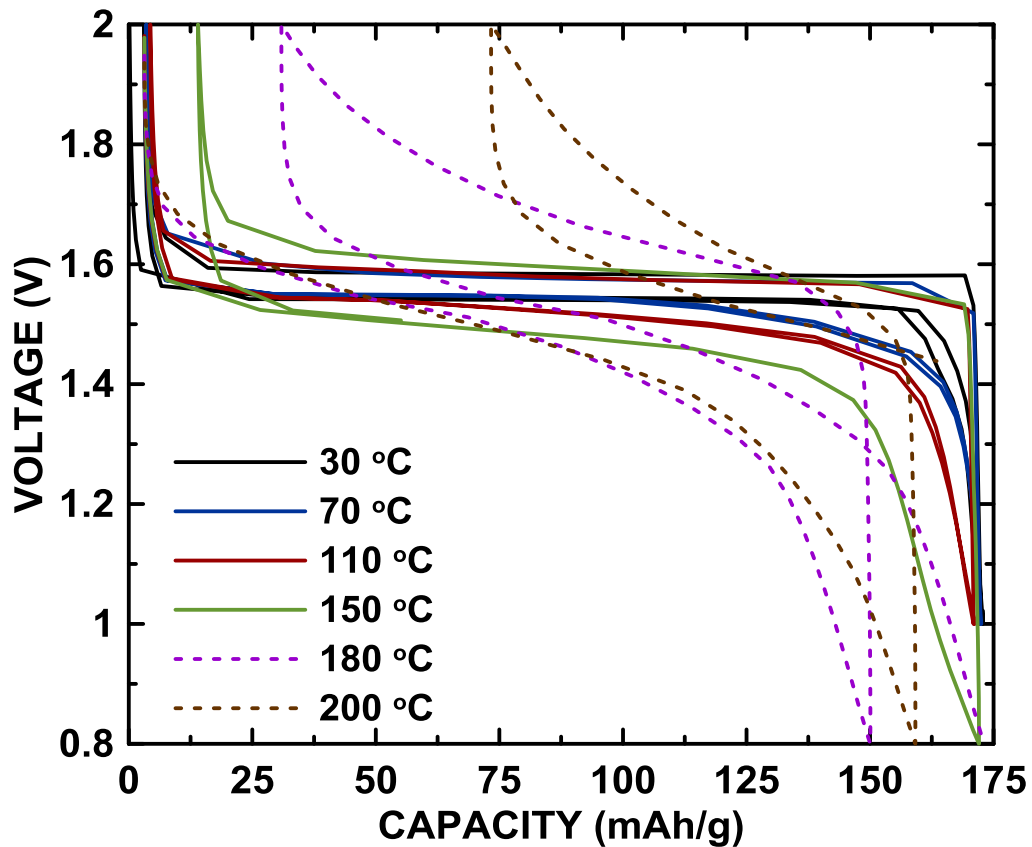Figure 4.15 shows the cycling performance of the cell. Also shown is the cycling performance of a Li/LTO 2-electrode coin cell for comparison. The cycling capacity remains constant up to about 110°C. At higher temperatures, electrolyte decomposition occurs causing impedance growth, capacity fade and poor Coulombic efficiency. The cycling performance of the Conflat and coin cells was identical up to a temperature of 130°C, where the coin cell seal failed. At this temperature the polyethylene coin cell gasket is completely molten. Coin cells with more volatile electrolytes fail at much lower temperatures, as mentioned above. In contrast, the Conflat seal remained intact and the cell continued to function up to 200°C, despite the shortcomings of the carbonate electrolyte. After disassembly the PTFE gasket was pristine. This provides interesting possibilities for the research of new materials for intermediate temperature cells.
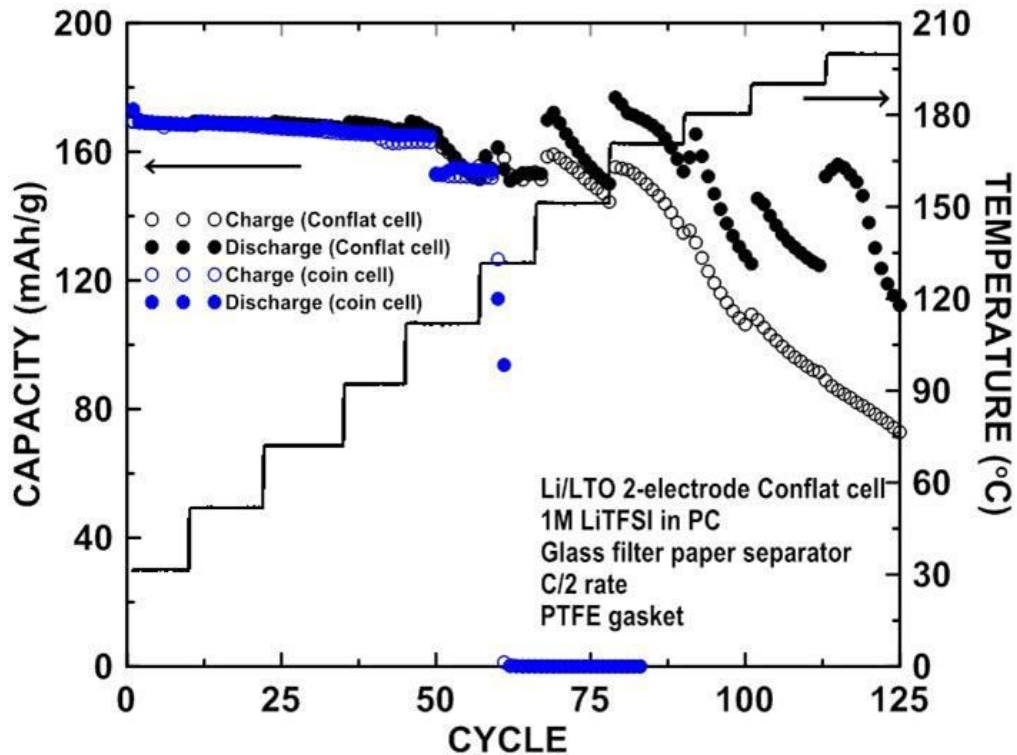

Figure 4.15: Capacity vs cycle number of a Li/LTO 2-electrode Conflat cell with 1M LiTFSI in PC electrolyte at different temperatures, as indicated in the figure.

4.4 Conclusion

Electrochemical cells based on inexpensive Conflat fittings were introduced. Such cells are sealed via a knife-edge impinging on a polymer seal. This allows a wide variety of polymers to be used that are temperature and chemically stable. 2 and 3-electrode Conflat cells were found to be easy to assemble in a reproducible fashion, cycle reliably were demonstrated to operate at temperatures up to $200°C$. It is believed such cells will be highly useful in research at high temperatures, with volatile or reactive solvents or where reliable 3-electrode cells with good stack pressure are needed. In particular Mg-battery research and research in high temperature cell chemistries using ionic liquids should benefit from this cell design.

CHAPTER 5   REVERSIBLE MAGNESIATION OF LEAD

5.1 Introduction

Rechargeable magnesium batteries have been long considered as a promising technology for energy storage and conversion. The low cost, low electrochemical potential and high volumetric and specific capacity of Mg makes it attractive as a negative electrode for secondary batteries.[5,57,59] However, a passivation layer is formed at the Mg electrode surface in common polar aprotic electrolyte solvents blocks both Mg ions and electron transport.[57] Reversible stripping and plating at the magnesium electrode has only been demonstrated in highly volatile ethereal-based solvents, THF[57] or DME.[68,107] It would be desirable to enable the use of non-volatile electrolytes with low flammability for the development of practical Mg batteries.

Alloys have been suggested for use as the negative electrode instead of Mg metal.[108] It has further suggested that the passivation layer on Mg metal electrodes might be avoided if Mg alloys are used as the negative electrode.[71,109] Arthur et. al demonstrated C-rate cycling of electrodeposited Bi, Sb and Bi-Sb alloys.[71] Bi forms Mg_3Bi_2 upon full magnesiation, corresponding to 384 mAh/g or 1897 Ah/L, with an average voltage of about 250 mV vs Mg. Sb forms Mg_3Sb_2 upon full magnesiation, corresponding to 660 mAh/g or 2040 Ah/L, with an average voltage of about 325 mV vs Mg. Therefore, when cycled versus a 1.2 V Mo_6S_8 cathode, the theoretical energy density of Bi and Sb are about 1800 Wh/L.

Bi could be cycled 100 times with low capacity fade at C-rate. Both rate and fade worsened with progressive additions of Sb. This was thought to be due to the increased Mg-Sb bond strength compared to that of Mg-Bi which causes a significant impact on the

electrochemical Mg-ion extraction properties. Arthur et al also showed reversible magnesiation from a Bi electrode with $Mg(TFSI)_2$ in acetonitrile electrolyte. Recently, Shao et al. have shown reversible magnesiation of nano-structured Bi for hundreds of cycles in diglyme-based electrolytes.[109] Furthermore, the nanostructure allowed high rates of up to 5C to be sustained.

Here Pb was considered as another potential anode material for rechargeable magnesium ion batteries. Lead is inexpensive, making it attractive for use in commercial batteries. Currently, lead acid batteries used in the majority of the > 1 billion automobiles on the planet. This made possible by the implementation recovery/recycling programs.[110] It was found that Mg can reversibly insert into Pb at 125 mV, forming Mg_2Pb. This corresponds to a theoretical capacity of 2316 Ah/L. This is the lowest voltage, highest volumetric capacity and highest energy density Mg alloy reported so far.

5.2 Experimental.

Two electrode Conflat cells, as described in Chapter 4, were constructed using a sputtered Pb disc or composite lead electrode fabricated as described in Section 3.3 and a Mg foil (99.95%, 0.25 mm thick, Gallium Source, LLC, Scotts Valley, CA) counter/reference electrodes. Two layers of Celgard 2300 separator were used in each cell with a layer of polyethylene blown microfiber separator (BMF, 3M Company) in between. The BMF provides a compliant layer, which improves stack pressure distribution. An electrolyte solution of 0.5 M ethylmagnesium chloride (EtMgCl, Sigma Aldrich) with or without 0.25 M $AlCl_3$ (anhydrous, 99.985%, Alfa Aesar) in tetrahydrofuran (THF, < 2 ppm H_2O, 99.9%, inhibitor free, Sigma Aldrich) was used in cells. Cells were cycled at C/40, C/50 or C/100 rate between 5 mV and 250 mV vs. Mg

at $60 \pm 0.1^{\circ}$C. Here C-rate was calculated based on the formation of Mg$_2$Pb at full magnesiation.

Ex-situ X-ray diffraction pattern (XRD) measurements were made by disassembling cells at different states of charge, rinsing the working electrode in THF and drying under vacuum to evaporate the solvent prior to be sealed in an air sensitive X-ray holder under argon atmosphere. XRD measurements were collected as explained in Section 3.1.1.

All the cells were constructed in an argon filled glovebox and were cycled at 60°C under thermostatically controlled conditions ($\pm$ 0.1°C) using a Maccor Series 4000 Automated Test System.

5.3 Results and Discussion

Figure 5.1 shows the voltage curve of a Pb/Mg two electrode Conflat cell cycled at C/50 rate at $60°C$. At this initial cycling rate, the cell continues to discharge well beyond the theoretical capacity of Pb (517 mAh/g). This is suggestive that catalytic reactions are occurring at the Pb electrode surface with the electrolyte that consume current, but do not allow the magnesiation of Pb to proceed. This effect has been observed previously on Sn surfaces in Li-ion[111] and Na-ion cells[112] and on Pb surfaces in Na-ion cells.[113] In Li-ion cells, such catalytic reactions can be avoided with the use of proper additives.[114] However, in Grignard reagents no analogously functioning additives are known. Another method to avoid catalytic electrolyte on alloy surfaces is to apply a high initial current pulse to the cell prior to discharge.[111–113] This is believed to cause a thin layer of the catalytic metal surface to alloy with Li or Na, rendering it non-catalytic.
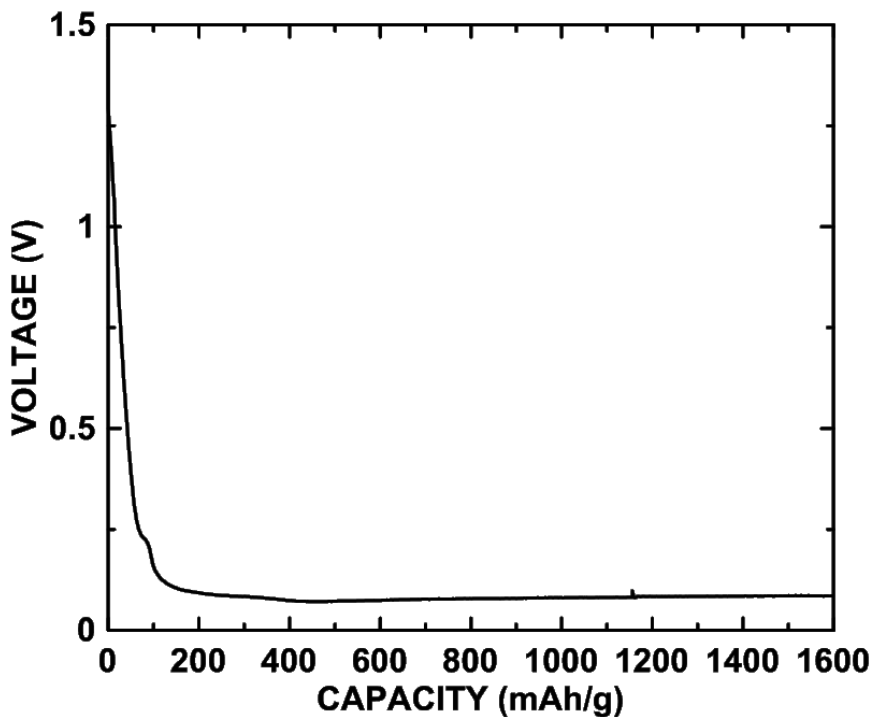

Figure 5.1: Voltage curve of a sputtered Pb film electrode vs. Mg at a C/50 rate at $60°C$.

63

In order to magnesiate the surface of Pb and inhibit reactivity with the electrolyte, cells were initially held at a constant voltage of 5 mV for 3 minutes and then the cell was allowed to rest for few minutes at open circuit voltage prior to constant current cycling. As shown in Figure 5.2, after the initial voltage hold, reversible cycling commenced. So little charge was passed through the cell during the initial voltage hold that it appears in the voltage curve as a vertical spike at the beginning of discharge. The voltage curve consists of a single plateau, indicative of a simple 2-phase reaction. The plateau has a low average voltage of about 125 mV, which is the lowest voltage yet reported for a magnesium alloy. Voltage polarization during cycling is also low for an alloy (~ 25 mV), indicating good kinetics. The reversible capacity for magnesiation is about 450 mAh/g. This is slightly less than the theoretical capacity for the formation of Mg_2Pb (517 mAh/g). This difference was attributed to weighing error in thin sputtered film. The formation of Mg_2Pb corresponds to a rather large volumetric capacity of about 2200 Ah/L, which is three times greater than that of graphite in a lithium ion cell and is the highest volumetric capacity reported for a magnesium alloy.
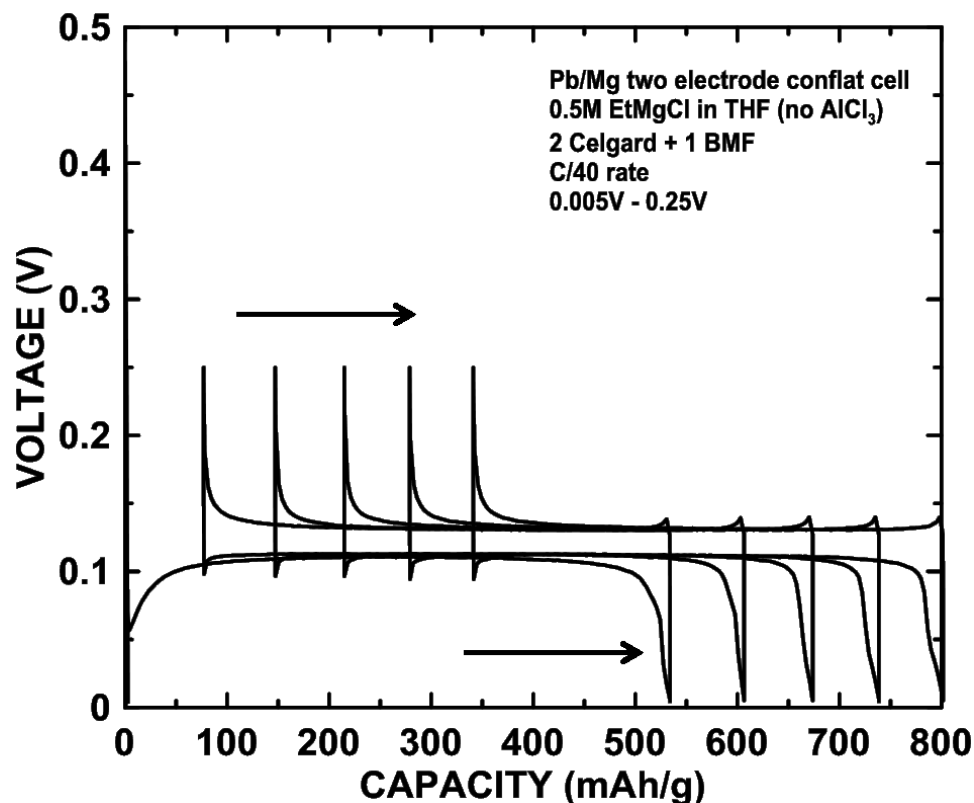
Figure 5.2: Voltage curve of a sputtered Pb film electrode vs. Mg at a C/40 rate at 60°C. A 3 minute potentiostatic hold at 5 mV was applied to the cell at the start of the first cycle (current = 0.017 mA).

Figure 5.3 shows the cycling performance of the sputtered Pb film electrode. The coulombic efficiency is poor, as the voltage curve has significant "slippage" during cycling. The discharge capacity exceeds the charge capacity by about 14% each cycle. Electrode slippage is associated with electrolyte decomposition reactions that consume the active ion at the working electrode.[115] For Li-ion battery materials, high precision coulometry is needed to detect slippage, as the slippage is usually within the error of conventional battery chargers. Here the slippage is so large that a conventional battery charger can easily detect it. After only 8 cycles the voltage curve slips in an amount that exceeds the reversible capacity of the electrode. Such a high rate of slippage indicates that Pb is poorly passivated in this electrolyte, which is surprising considering the

65

stability of THF.[105]   However even though Mg is irreversibly consumed by the side reactions, there is a continuous supply of Mg from the counter/reference electrode; therefore no detectable capacity loss occurs during cycling.
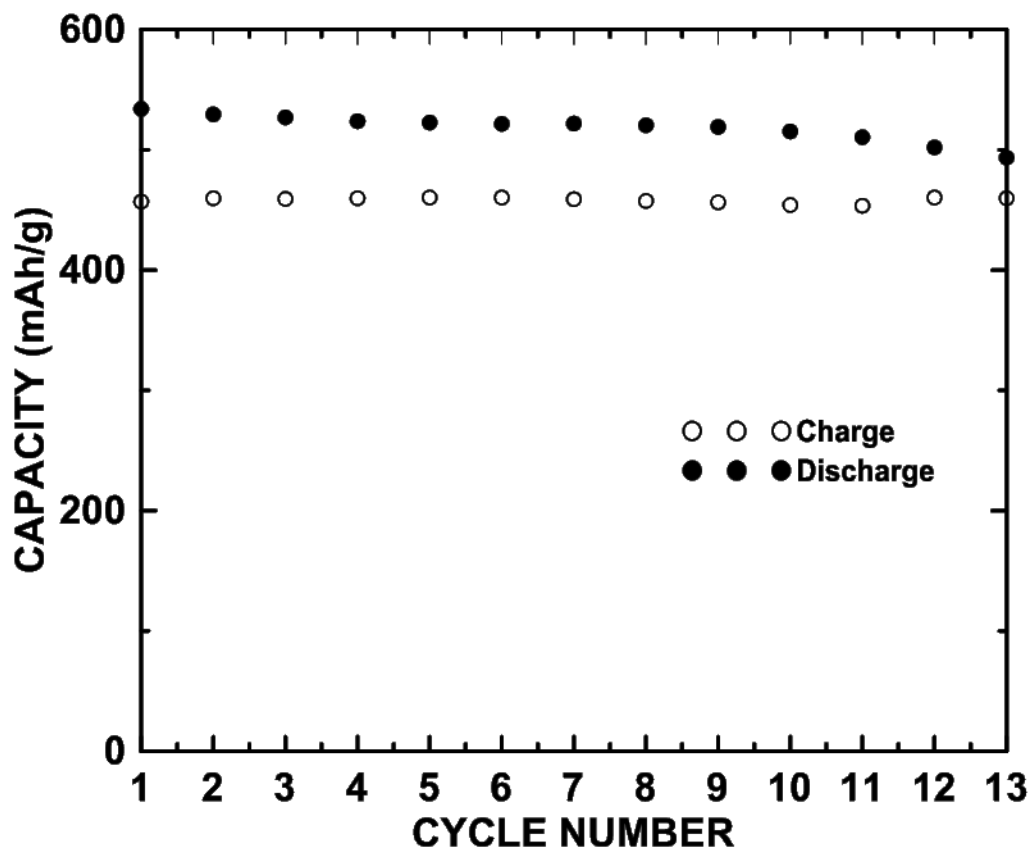

Figure 5.3: Cycling performance of the cell shown in Figure 5.2.

Figure 5.4 shows an ex-situ XRD pattern of a sputtered Pb electrode after being discharged to 5 mV. The majority phase in the XRD pattern in Mg_2Pb, however a small amount of Pb remains unreacted in the electrode. Two peaks at $21.0°$ and $23.4°$ in the XRD pattern are suspected to be from electrolyte residue left on the Pb electrode surface.
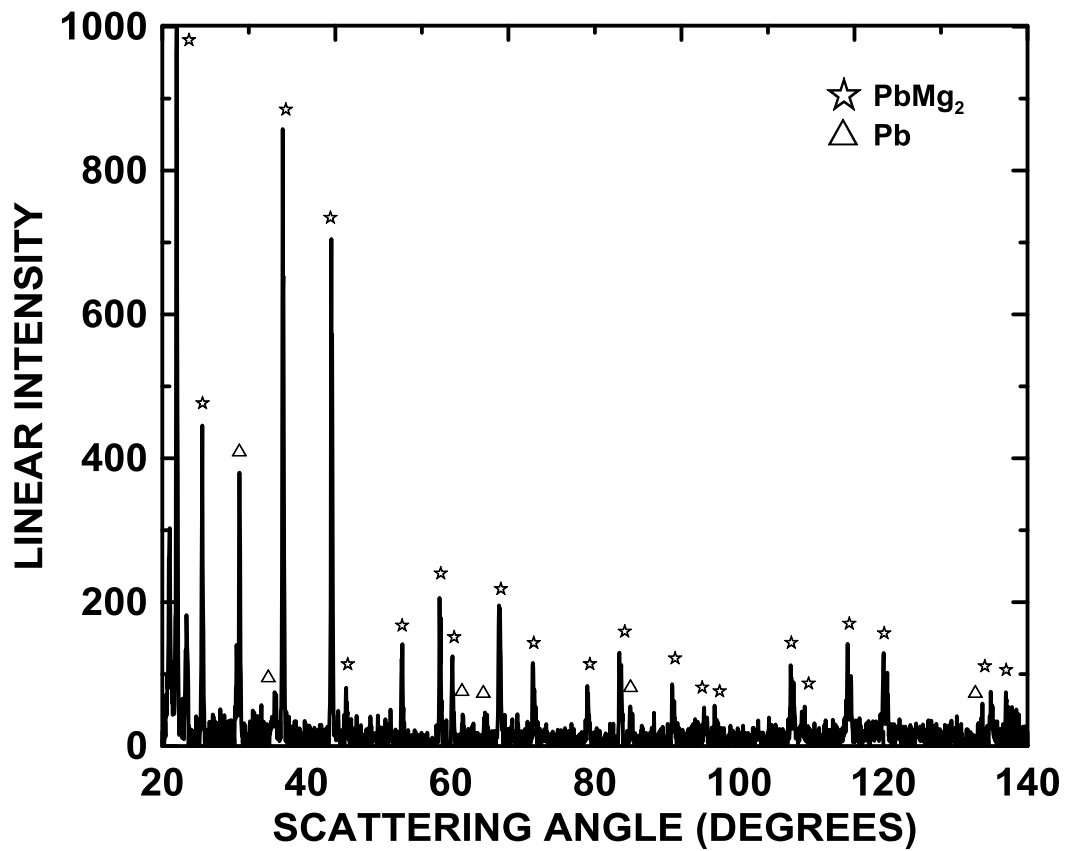

Figure 5.4: Ex-situ XRD of a fully magnesiated sputtered Pb film electrode.

Figure 5.5 shows an ex-situ XRD pattern of a sputtered Pb electrode after it has been discharged to 5 mV, and then charged to 0.25 V. The XRD peaks are now completely due to Pb, excepting some electrolyte residue peaks at 21.0° and 23.4°. Therefore the magnesiation of Pb follows the equilibrium phase diagram according to:

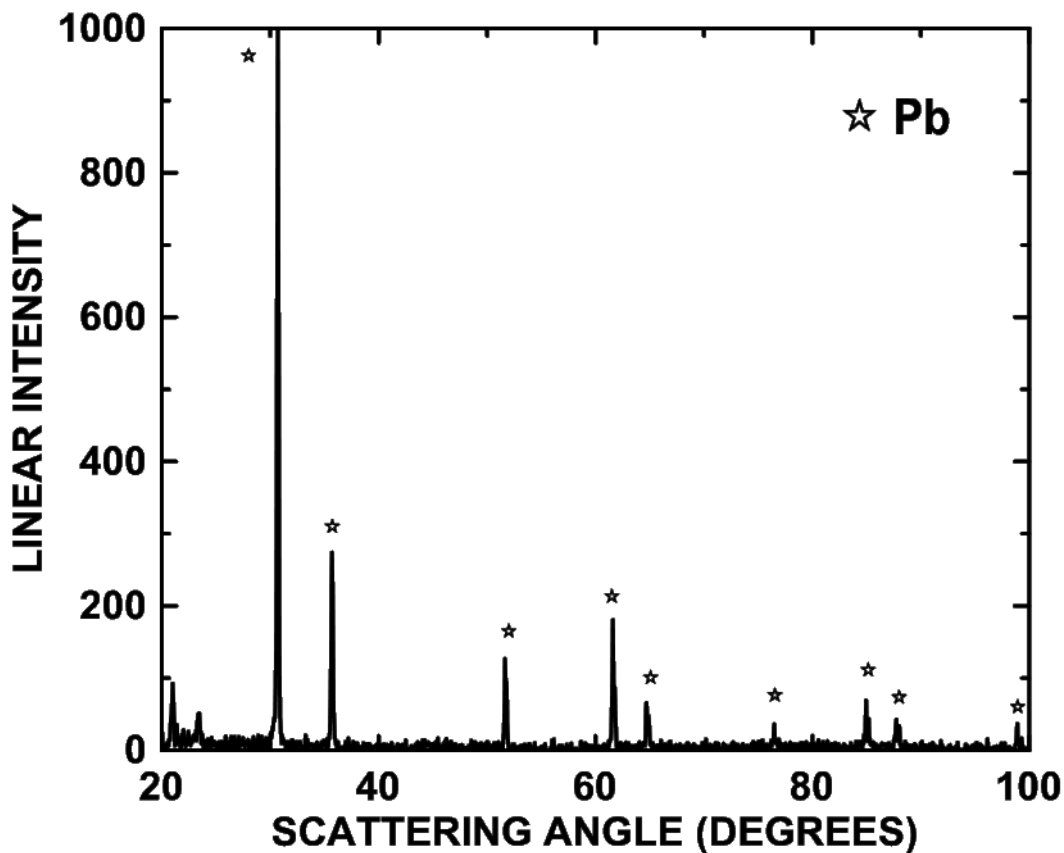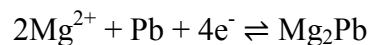$$2Mg^{2+} + Pb + 4e^- \rightleftharpoons Mg_2Pb$$

Figure 5.5: Ex-situ XRD of a sputtered Pb film electrode that was fully magnesiated, and then demagnesiated.

Figure 5.6 shows the voltage curve of a Pb composite coating vs. Mg. It is similar to the sputtered coating, excepting that a low voltage and sloping plateau grows during cycling. This plateau was also present in the voltage curve of some sputtered films. The origin of this plateau is not yet known, although it resembles that of fully lithiated Sn.[116] Near full lithiation, Sn forms disordered Li_xSn clusters, with sloping voltage plateaus.[117] Perhaps a similar mechanism occurs here. Such phases are difficult to detect by XRD and could find no evidence for them by ex-situ XRD.
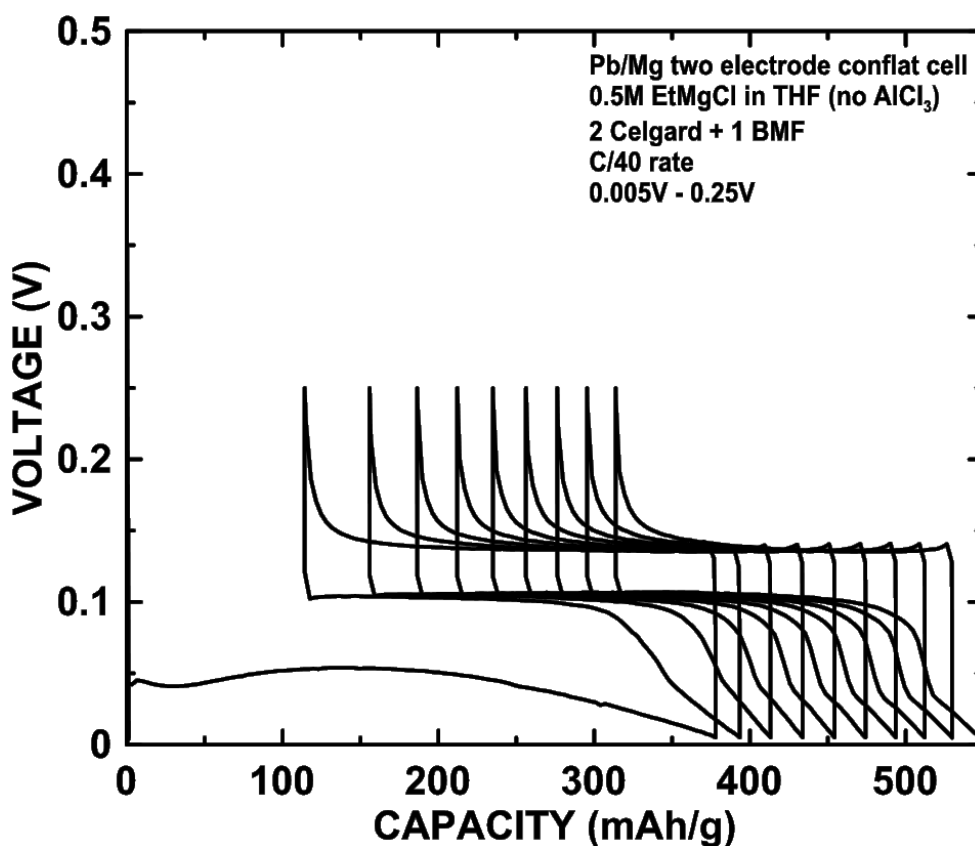

Figure 5.6: Voltage Curve of a Pb composite coating electrode vs Mg at a C/40 rate at 60°C. A 3 minute potentiostatic hold at 5 mV was applied to the cell at the start of the first cycle.

69

Figure 5.7 shows the cycling performance of the Pb composite coating vs. Mg cell shown in Figure 5.6. The irreversible capacity of this cell is ~114 mAh/g and is considerably higher than that of the cell with sputtered deposited Pb electrode. The reversible capacity is only about 275 mAh/g, which is much less than that of the sputtered electrode. Pb particles may have become disconnected during cycling or Mg may not be able to access the core of the particles, which have a much larger diameter than the sputtered film. Like the sputtered film, the electrode slippage is high and coulombic efficiency is low. Improved electrolyte stability is required for Pb electrodes to find practical use in Mg cells.
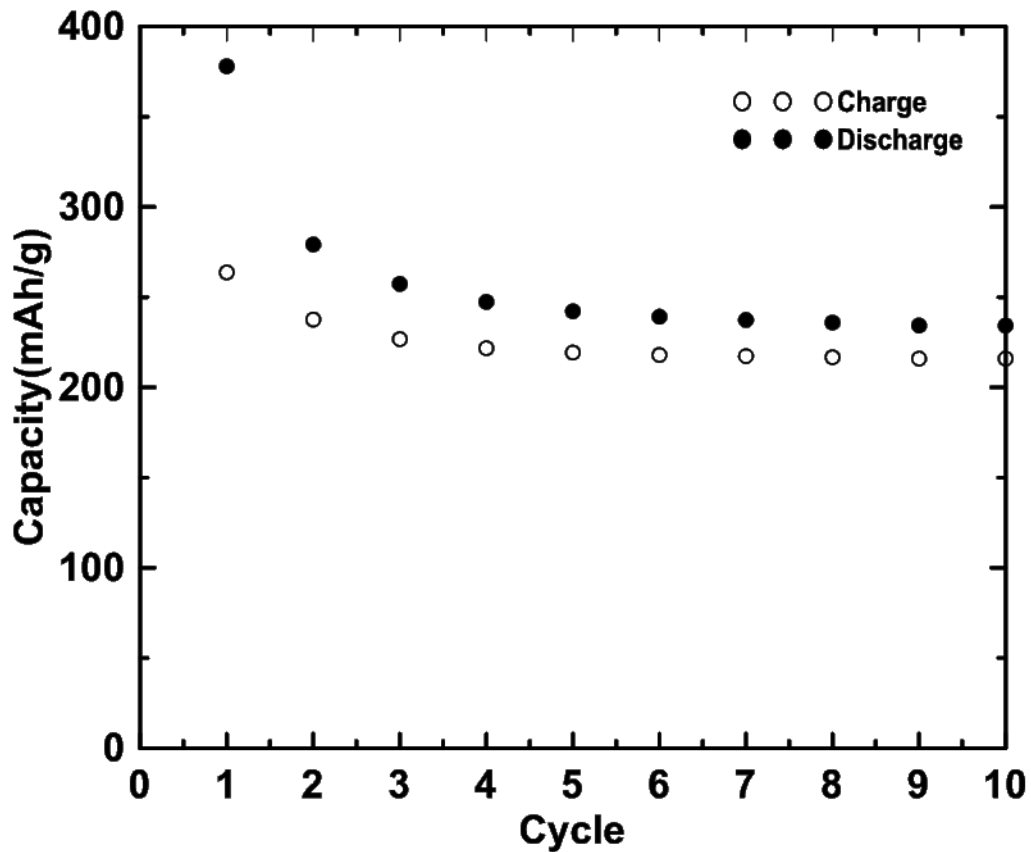

Figure 5.7: Cycling performance of Pb composite coating electrode vs Mg cell shown in Figure 5.6.

5.4 Conclusion

Magnesium was reversibly inserted in sputtered and composite Pb electrodes, forming Mg_2Pb in a 2-phase reaction with a theoretical capacity of 2316 Ah/L, which is the highest volumetric capacity reported for an Mg alloy. In addition the Pb vs. Mg voltage curve has the lowest voltage (~125 mV) of any Mg alloy. Therefore Pb was found to be the highest energy density alloy material yet reported in Mg batteries. However, extremely poor coulombic efficiencies were observed that are indicative of electrolyte decomposition reactions at the Pb surface during cycling. Improved electrolyte stability is required for Pb electrodes to find practical use in Mg cells.

CHAPTER 6   SYNTHESIS AND ELECTROCHEMICAL PERFORMANCE OF CHEVREL PHASE IN Mg AND Li CELLS

6.1 Conventional Solid State Synthesis

6.1.1 Introduction

Binary and ternary molybdenum chalcogenides, with the compositions Mo_6X_8 and $M_xMo_6X_8$ (M = metal, X = S, Se, Te) have been intensively studied owing to their unusual structural and physical properties.[118–120] They are intriguing as electrode materials in secondary batteries due to their relatively fast and reversible intercalation of various monovalent (Li^+, Na^+, Cu^+) and divalent (Mg^{2+}, Zn^{2+}, Cd^{2+}, Ni^{2+}, Mn^{2+}, Co^{2+}, Fe^{2+}) cations at ambient temperatures.[121–125]

Even though rechargeable Li ion batteries are widely used in high energy density applications, their safety, cost and geographically limited reserves makes it indispensable to exploit alternative battery technologies such as Mg, Al and Zn.[58,59] Mo_6S_8 Chevrel phase is one of the most reversible cathode materials for nonaqueous Mg batteries and has been studied for over a decade. However, Mo_6S_8 is metastable at room temperature and can only be prepared indirectly by leaching metal ions from thermodynamically stable insertion compounds, such as $Cu_2Mo_6S_8$.[79,80,106]

This section will describe the synthesis of $Cu_2Mo_6S_8$ by the high temperature solid state method introduced by Kondo et al.,[126] and an alternative method developed to synthesize $Cu_2Mo_6S_8$ efficiently in terms of time duration. The electrochemical performance of its leached product Mo_6S_8 with Li and Mg metals will also be discussed.

6.1.2 Experimental

$Cu_2Mo_6S_8$ by solid state route was synthesized according to the method in reference:[59] A stoichiometric mixture of Cu (~325 mesh, 99% metal basis, Alfa Aesar), Mo (>99.9%, 1-2 μm, Sigma Aldrich) and MoS_2 powder (~325 mesh, 99% metal basis, Alfa Aesar) was heated under vacuum for 12 hours at 150°C and then at 985°C for 150 hours to produce $Cu_2Mo_6S_8$. Cu was then leached from the resulting$Cu_2Mo_6S_8$ according to the method described in reference:[58] The $Cu_2Mo_6S_8$ powder was placed in an excess amount of 6 M HCl while stirring under bubbling O_2 for at least 12 hours. The leached product, Mo_6S_8, was then centrifuged and washed with distilled water followed by air drying at $150^{\circ}C$ for 2 hours. Mo_6S_8 composite electrodes were fabricated as described in Section 3.4 and all the XRD measurements were taken as mentioned in Section 3.1.1.

Counter electrodes (18 mm diameter circles) and reference electrodes were punched from Li foil (99.9%, 0.38 mm thick, Sigma Aldrich) and Mg foil (99.95%, 0.25 mm thick, Gallium Source, LLC, Scotts Valley, CA). Working electrodes were (16 mm circles) punched from coated foils. An electrolyte solution of 1M $LiPF_6$ in 1:2 EC: DEC (1:2 v/v, < 50 ppm H_2O, BASF) was used in lithium cells and 0.5 M $Mg(TFSI)_2$ in ACN, (99.8% anhydrous, Sigma Aldrich) was used in Mg cells. All the cells were constructed in Conflat cells in an argon filled glovebox and were cycled under thermostatically controlled conditions ($\pm\ 0.1^{\circ}C$) using a Maccor Series 4000 Automated Test System.

6.1.3 Results and Discussion

As shown in Figure 6.1, $Cu_2Mo_6S_8$ prepared by above high temperature method is highly crystalline and is composed of two phases, $Cu_2Mo_6S_8$ and $Cu_{0.9}Mo_3S_4$. No traces of impurities or unreacted starting materials were detected in the XRD.
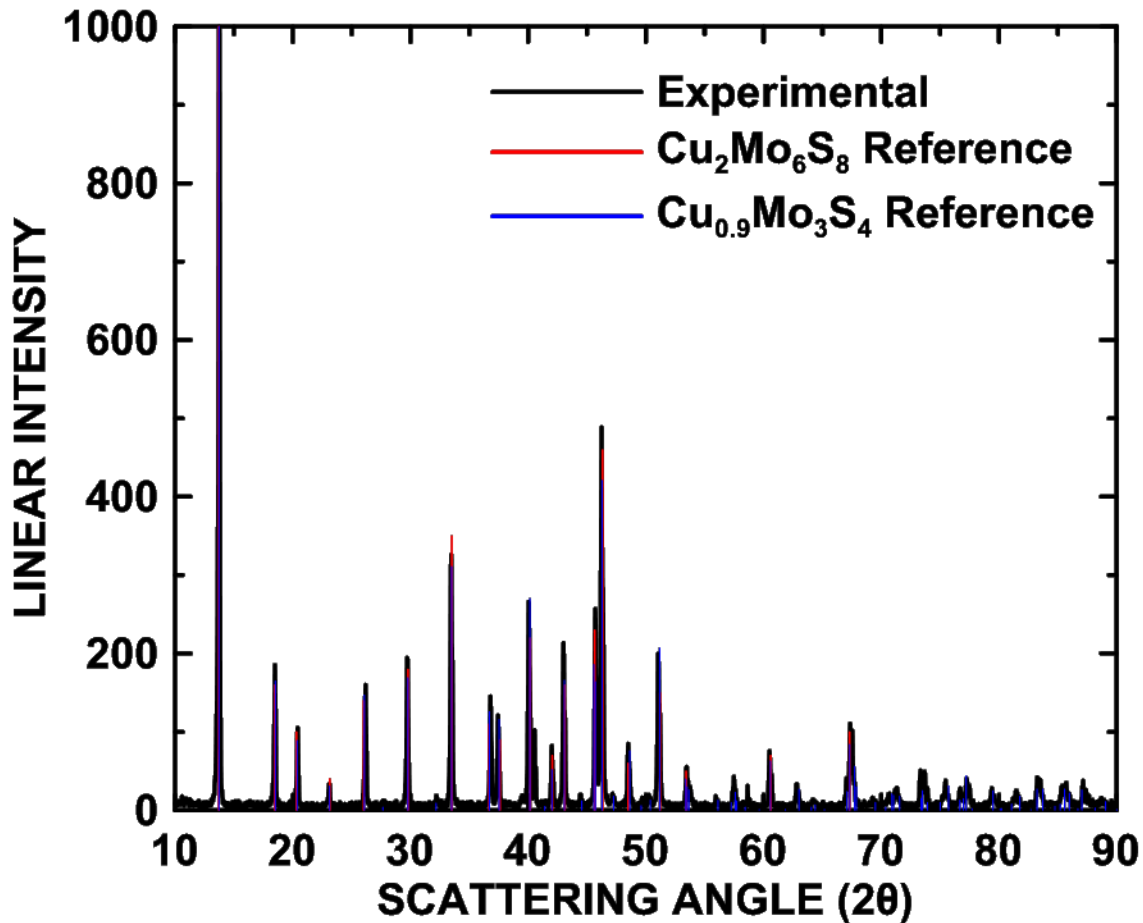
Figure 6.1: XRD pattern for heat treated Cu-Chevrel phase compound

As shown in Figure 6.2, the leached product Mo_6S_8 is a single phase crystalline material. No impurities or Cu residues were detected in the XRD pattern.
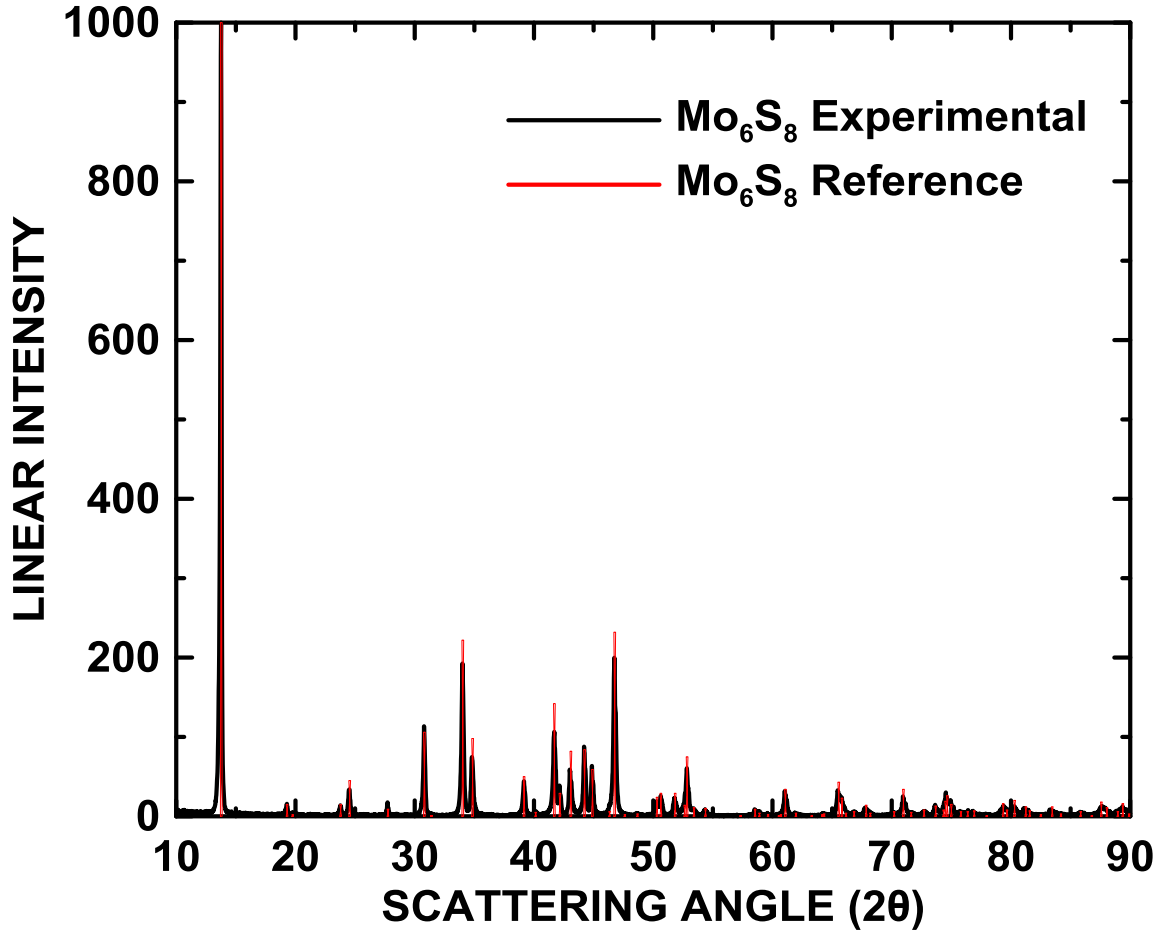
Figure 6.2: XRD pattern for leached Mo_6S_8 Chevrel compound

Figure 6.3 shows the voltage curve of a $Li/Li/Mo_6S_8$ 3-electrode Conflat cell. The voltage curve shows a high irreversible capacity and an electrode slippage to the right. Voltage curve slippage could be caused by electrolyte decomposition reactions at elevated temperatures. Even though Li is irreversibly consumed by the electrolyte decomposition reactions, there is a near unlimited supply of Li from the Li CE. Therefore, as shown in Figure 6.4, a reversible capacity close to its theoretical value (128 mAh/g) was observed even after 50th cycle.
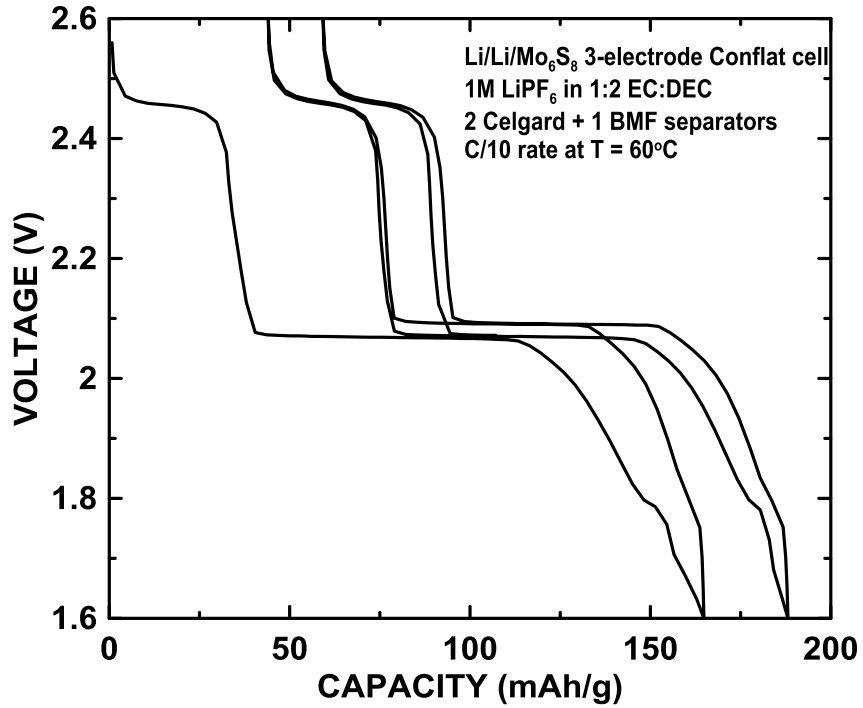
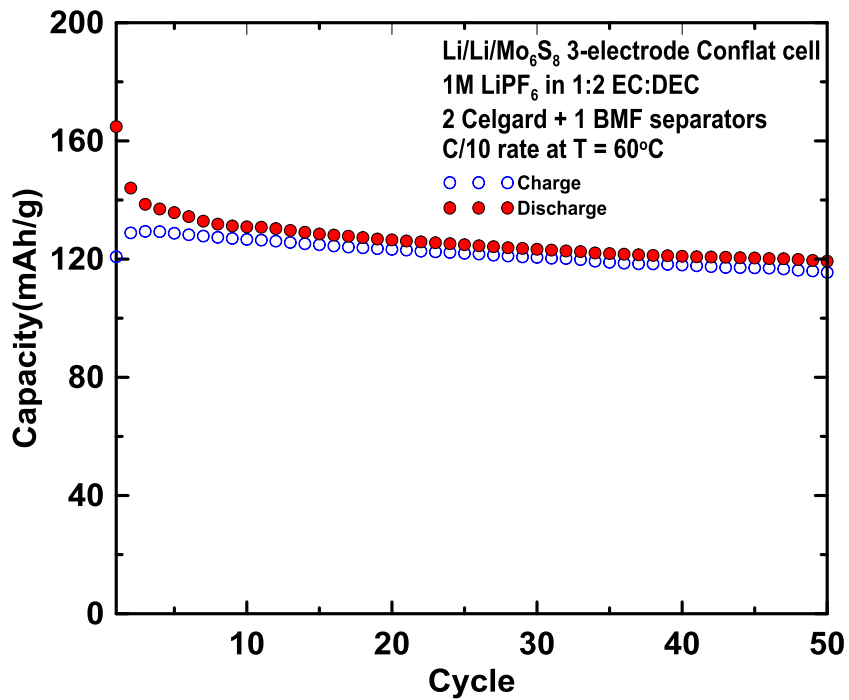Figure 6.3: Voltage curve of a Li/Li/ Mo_6S_8 3-electrode Conflat cell with 1M $LiPF_6$ in 1:2 EC: DEC electrolyte at 60°C.

Figure 6.4: Cycling performance of a Li/Li/Mo_6S_8 3-electrode Conflat cell with 1M $LiPF_6$ in 1:2 EC: DEC electrolyte at 60°C.

Unlike with Li, Mo_6S_8 showed poor electrochemical performance when cycled with Mg. Figure 6.5 shows the voltage profile of a $Mg/Mg/Mo_6S_8$ 3-electrode Conflat cell cycled with 0.5M $Mg(TFSI)_2$ in ACN electrolyte at a rate of C/100 at 60°C. This cell showed a large irreversible capacity and a reversible capacity of ~60 mAh/g, which is half the theoretical value. This behaviour might be due to poor intercalation kinetics of Mo_6S_8 caused by large particle size.
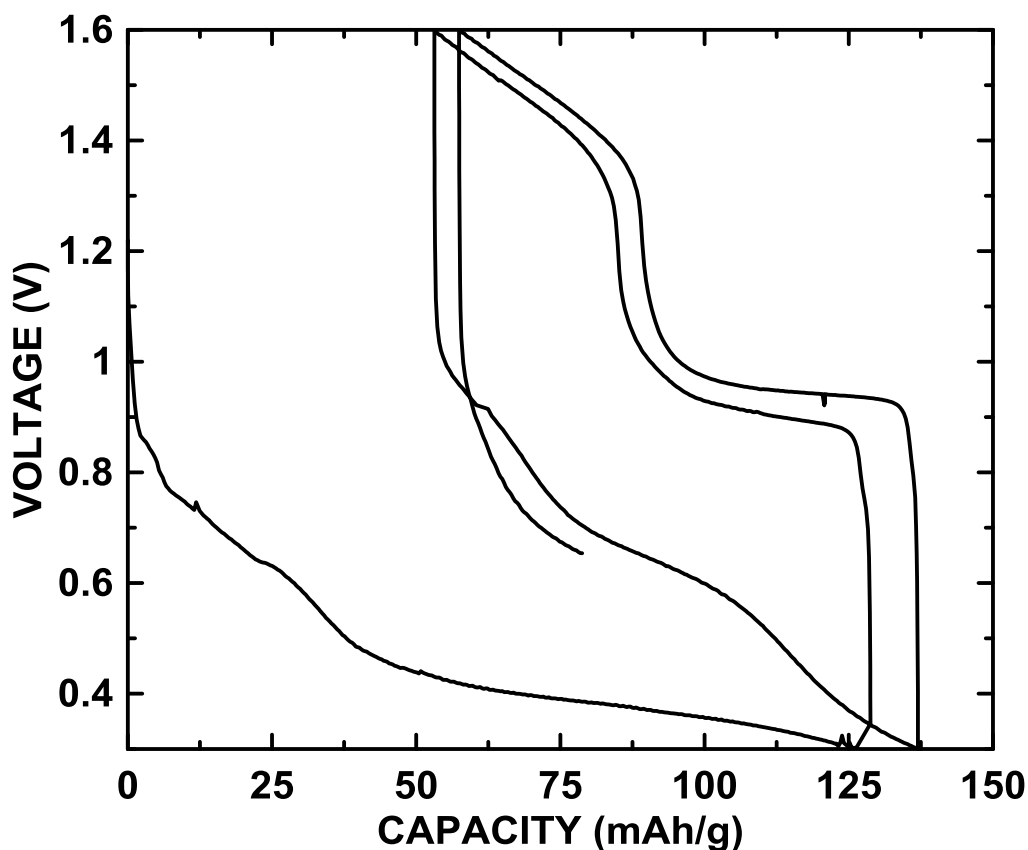

Figure 6.5: Voltage curve of a $Mg/Mg/Mo_6S_8$ 3-electrode Conflat cell with 0.5M $Mg(TFSI)_2$ in ACN electrolyte at a rate of C/100 at 60°C.

A possible way to improve the insertion-extraction kinetics of the electrode material is to reduce the particle size. This reduces the diffusion path length of Mg-ions. Lancry et al. showed that $Cu_2Mo_6S_8$ is unstable upon milling.[127] The mechanical treatment of the compound leads to an unusual amorphization and causes a chemical

77

reaction in which the Cu^+ ions are reduced and removed from $Cu_2Mo_6S_8$ lattice, in agreement with Mo oxidation to MoS_2.[127] It has been shown that this unusual instability of $Cu_2Mo_6S_8$ leads to a drastic decrease in battery performance.

Therefore to reduce the particle size, Mo_6S_8 was ground by an autogrinder (Brinkman Retsch RMO mortar grinder) at 580 rpm for 3 hours. As shown in Figure 6.6 (a) and (b), autogrinding has significantly reduced the Mo_6S_8 particle size. According to SEM images, Mo_6S_8 before being subjected to autogrinding appeared to have a flake-like morphology with a particle size 0.5 - 4.0 μm. As shown in Figure 6.6 (b) after grinding most of the agglomerated flakes were broken into primary particles and the particle size was also reduced to 0.5 – 2.0 μm.
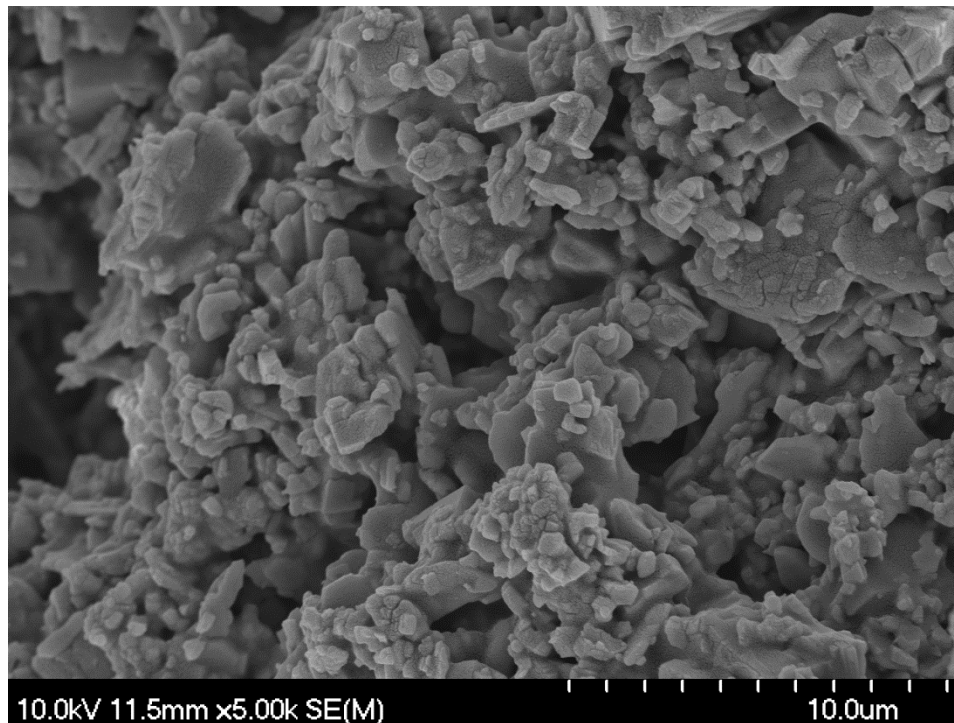

Figure 6.6 (a): SEM image of Mo_6S_8 before autogrinding, particle size 0.5 - 4.0 μm.
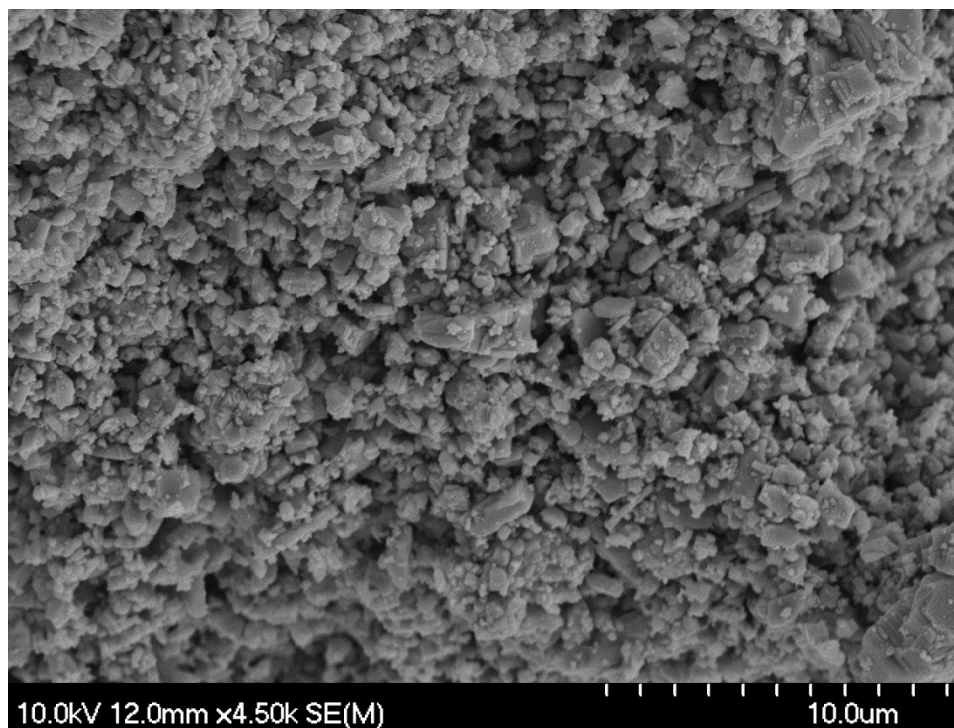
10.0kV 12.0mm ×4.50k SE(M)   10.0um

Figure 6.6 (b): SEM image of Mo_6S_8 after autogrinding, particle size $0.5 - 2.0$ μm.

Electrochemical performance of the composite electrodes fabricated from ground Mo_6S_8 (Section 3.4) was tested in a Mo_6S_8/Mg/Mo_6S_8 3-electrode full cell with 0.5M $Mg(TFSI)_2$ in ACN. As shown in Figure 4.12 and 4.13 in Chapter 4, kinetics of Mo_6S_8 was improved and the irreversible capacity was reduced. The reversible capacity of the cell was close to its theoretical value. This leads to a question of whether further optimization of Mo_6S_8 particle size can improve the electrochemical performance. Ongoing research work is being carried out in optimizing the particle size under different milling conditions using planetary milling. This will be described in Section 8.1.

6.2 Alternative Solid State Synthesis Method for Mo_6S_8 Chevrel

6.2.1 Introduction

In order to develop new cathode, anode, and electrolyte systems for rechargeable Mg batteries, a reversible CE is required. As Mg metal is a blocking electrode in most electrolytes, Mo_6S_8 Chevrel is a better choice for the CE due its good kinetics and reversibility. In order to use Mo_6S_8 as the CE, an efficient method is required to synthesize $Cu_2Mo_6S_8$. The conventional high temperature synthesis is a slow process. In this work an alternative method was investigated to synthesize Chevrel in a reduced time period.

The first approach proposed to produce $Cu_xMo_6S_8$ is solid state synthesis which was initially reported by Chevrel et al.,[79] where a stoichiometric mixture of Cu, Mo and S was heated at a high temperature ($\sim 1000^\circ C$) in an evacuated sealed quartz tube. However, the high S vapour pressure inside the tube at elevated temperatures limits the heating rate and the amounts of starting materials. In a second approach, the sulfur vapour pressure was avoided by using metal sulfide instead of sulfur as the starting material. As reported by Kondo et al.[126] a stoichiometric mixture of Cu, MoS_2 and Mo was heat treated at 150^oC for several hours and at $985^\circ C$ for 150 hours under vacuum in a non-sealed quartz tube. This is a highly time consuming route.

The third approach was reported by Rabiller-Baudry et al.[128] where $Cu_xMo_6S_8$ was synthesized from soluble sulfide precursors such as polythiomolybdates and metal salts prepared by soft chemistry at relatively low synthesis temperature ($800^\circ C$). This method allowed producing particles at micrometric scale with high surface area. E. Lancry et al.[80] reported a method for large scale production of $Cu_2Mo_6S_8$ via a molten salt route, by

reacting Mo, MoS_2 and CuS in KCl salt and heat treating the reaction mixture at $850^{\circ}C$ for 60 hours under Ar atmosphere. This approach offers much improvement in terms of decreasing both synthesis duration and temperature compared to conventional solid state reaction method.

This work presents another method of synthesizing $Cu_2Mo_6S_8$ by solid state synthesis using powdered Cu, Mo and MoS_2 as starting materials. Through this method, the synthesis duration was reduced to 24 hours and limited the leaching time period to 12 hours. Moreover, this is a successful method that can be used for bulk production of the material.

6.2.2 Experimental

A stoichiometric mixture of powdered Cu (~325 mesh, 99% metal basis, Alfa Aesar), Mo (>99.9%, 1-2 μm, Sigma Aldrich) and MoS_2 (~325 mesh, 99% metal basis, Alfa Aesar) was ball milled using a Spex mill (Model 8000-D, 975 ± 15 rpm, Spex Certiprip, Metuchen, N.J.) for 1 hour, with 115 g WC balls (3/16 inch in diameter) in a stainless steel vial (60 cm^3). The resultant homogenous powdered mixture was allowed to react in a quartz boat under vacuum through three sequential stages: (1) Heating at $150^{\circ}C$ for 2 h, (2) heating at $985^{\circ}C$ for 22 h, (3) naturally cooling down to room temperature. Cu was leached from $Cu_2Mo_6S_8$ according to the method described in Section 6.1.2 and the XRD measurements were taken as in Section 3.1.1.

CE/RE (18 mm diameter circles) were punched from Li foil (99.9%, 0.38 mm thick, Sigma Aldrich) and Mg foil (99.95%, 0.25 mm thick, Gallium Source, LLC, Scotts Valley, CA). WE were (16 mm circles) punched from coated foils. Mo_6S_8 electrodes were made as mentioned in Section 3.4. Average electrode loading was 3.33 mg/cm^2. An

electrolyte solution of 0.5 M EtMgCl (Sigma Aldrich) and 0.25 M AlCl$_3$ (anhydrous, 99.985%, Alfa Aesar) in THF (< 2 ppm H$_2$O, 99.9%, inhibitor free, Sigma Aldrich) was used in Mg cell and 1M LiPF$_6$ in 1:2 EC:DEC (1:2 v/v, < 50 ppm H$_2$O, BASF) electrolyte was used in lithium cell. Mg/Mo$_6$S$_8$ cell was cycled at C/20 rate at 30°C and Li/Mo$_6$S$_8$ cell was cycled at C/10 rate at 60°C. All cells were cycled under thermostatically controlled conditions (± 0.1°C) using a Maccor Series 4000 Automated Test System.

6.2.3 Results and Discussion

Figure 6.7 shows the XRD pattern of the precursor materials Spex milled in air, which agrees with the reference pattern. The initial milling was used to improve the kinetics of the thermal reaction by increasing the surface area and more intimately mixing the starting materials. No intermediate phases were formed during Spex milling.
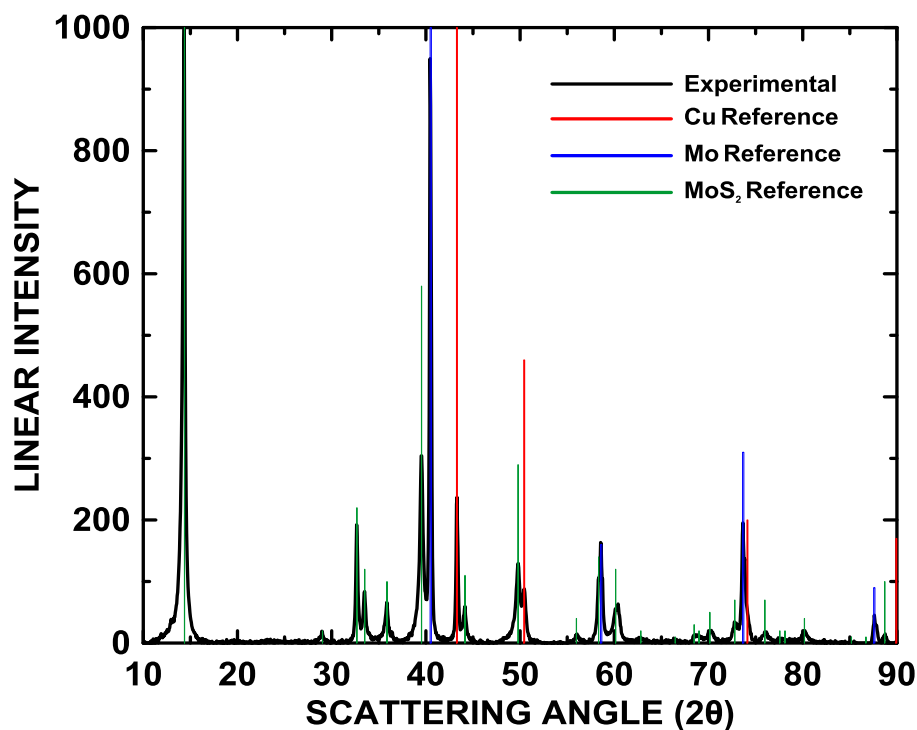

Figure 6.7: Powder XRD pattern of Spex milled powder before heat treatment

Figure 6.8 shows the XRD pattern of the heat treated sample of $Cu_2Mo_6S_8$ prepared by Spex milling. The sample appears to be a mixture of two highly crystalline phases, $Cu_2Mo_6S_8$ and $Cu_{0.9}Mo_3S_4$. Similar results were obtained for $Cu_2Mo_6S_8$ prepared as described in Section 6.1.2. Neither MoS_2 nor Mo impurity was detected in the XRD pattern.
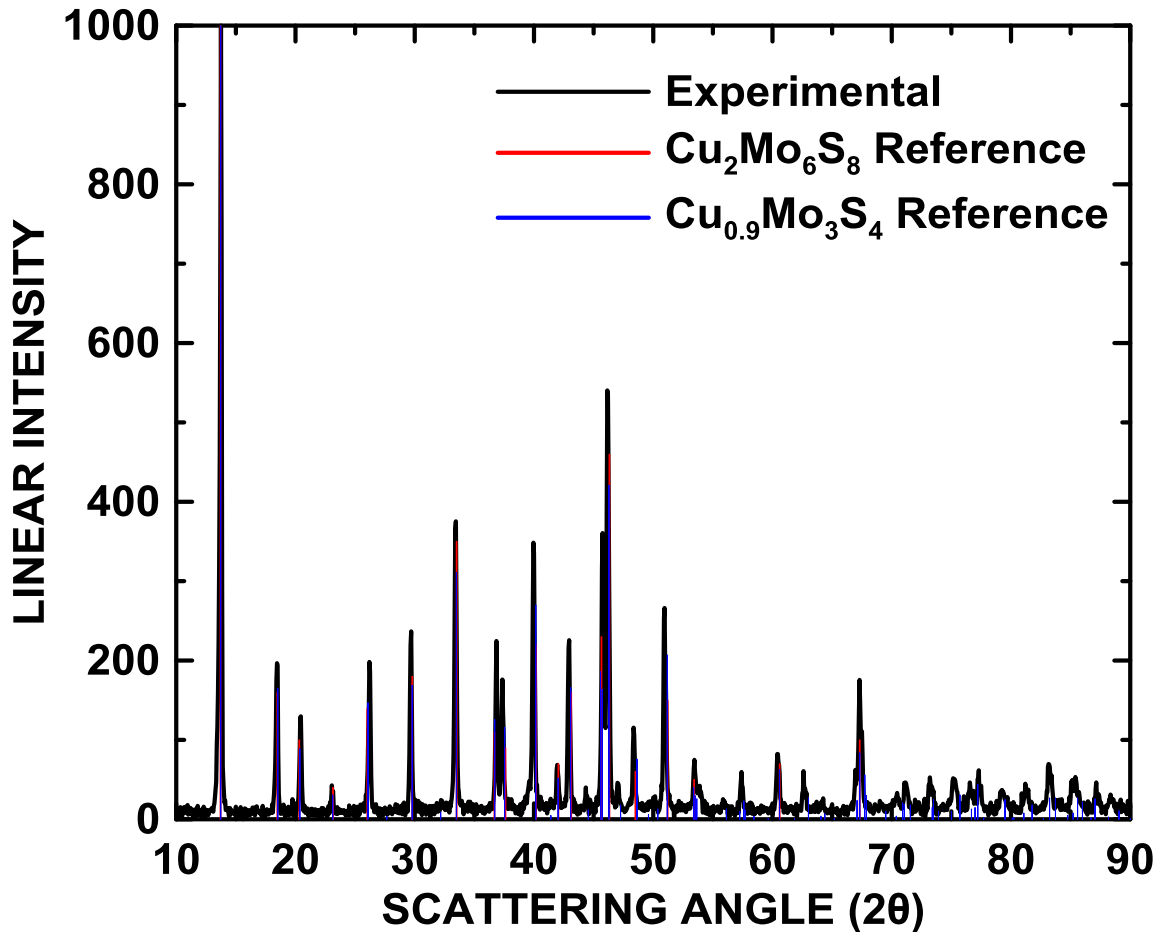

Figure 6.8: Powder XRD pattern of Spex milled powder after heat treatment showing the formation of $Cu_2Mo_6S_8$.

According to the XRD pattern shown in Figure 6.9, both of the above phases completely converted into Mo_6S_8 during leaching without leaving any impurities. The chemistry of the leaching process can be stated as below, where formation of water and stable $[CuCl_4]^{2-}$ compound is the driving force of the reaction.[80]
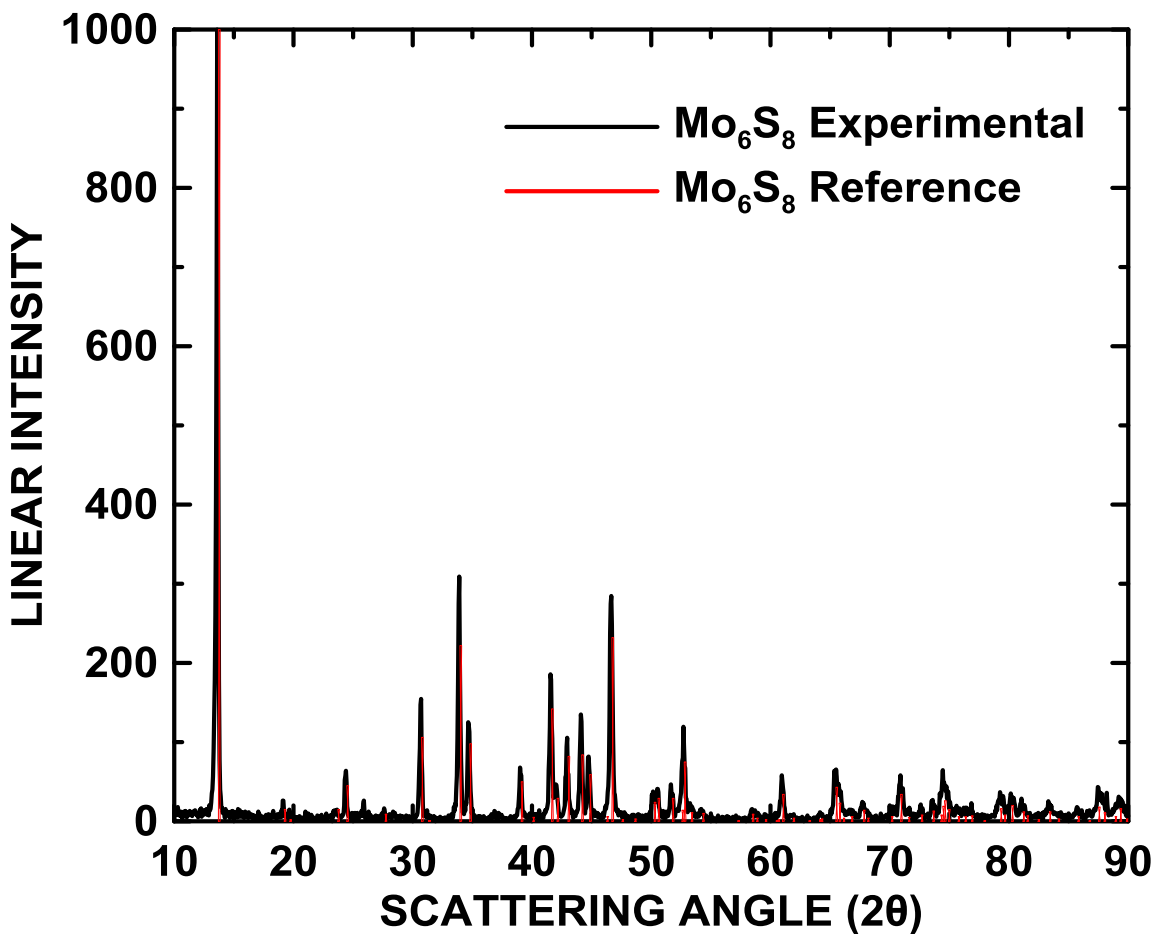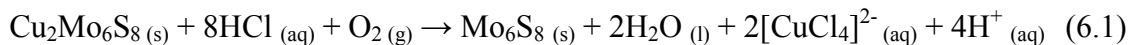
$$Cu_2Mo_6S_{8\,(s)} + 8HCl_{\,(aq)} + O_{2\,(g)} \rightarrow Mo_6S_{8\,(s)} + 2H_2O_{\,(l)} + 2[CuCl_4]^{2-}_{\,(aq)} + 4H^+_{\,(aq)} \quad (6.1)$$

Figure 6.9: Powder XRD pattern of acid leached Mo_6S_8 powder prepared by Spex milling method.

Figure 6.10 compares the voltage profiles of Mo_6S_8 prepared by conventional high temperature solid state synthesis and Spex milling cycled vs Li at $60^{\circ}C$. Both materials show similar electrochemical performance, indicating that the leached product of $Cu_2Mo_6S_8$ prepared by Spex milling is successful. The stoichiometry and kinetics of the Li insertion into the Mo_6S_8 differs from the insertion of Mg ions and involves three fast processes as described in Gocke et al.[120]

$$Li^+ + e^- + Mo_6S_8 \rightarrow Li_1Mo_6S_8 \qquad (6.2)$$

$$2Li^+ + 2e^- + Li_1Mo_6S_8 \rightarrow Li_3Mo_6S_8 \qquad (6.3)$$

$$Li^+ + e^- + Li_3Mo_6S_8 \rightarrow Li_4Mo_6S_8 \qquad (6.4)$$

As stated in reference,[121] the amount of Li inserted (x) is 0 at 2.6 V and x = 4 at 1.75 V. The theoretical capacity of Mo_6S_8 is 128 mAh/g, and Mo_6S_8 synthesized by Spex milling showed a reversible capacity of 120 mAh/g with a little capacity loss during cycling. This performance is similar to that of Mo_6S_8 prepared by conventional high temperature solid state synthesis.[80] The voltage profiles of Mo_6S_8 prepared by both high temperature synthesis and Spex milling precursor methods show a severe voltage slippage to the right when cycled vs Li metal. This voltage slippage is associated with the oxidative electrolyte decomposition reactions that consume the active ion to form either SEI or soluble decomposition products at electrode surface. The slippage per cycle gradually decreases with cycling number, indicating that some of the decomposition products may be forming a stable SEI layer.[115] Formation of the SEI also explains the large irreversible capacity between the first discharge and the second consecutive cycle in both of the cells. The coulombic efficiency of a cell is defined as follows (equation 6.1).

$$Coulombic\ effciency\ (\%) = \left(\frac{charge\ capacity}{discharge\ capacity}\right) * 100 \qquad (6.1)$$

As shown in Figure 6.11, the significant difference between the discharge and charge capacities indicates a poor coulombic efficiency.

The cycling performances of Mo_6S_8 Chevrel phase synthesized by both of the methods discussed above shows that they are capable of reversible intercalation of Li ions with a reversible capacity close to its theoretical value (128 mAh/g).
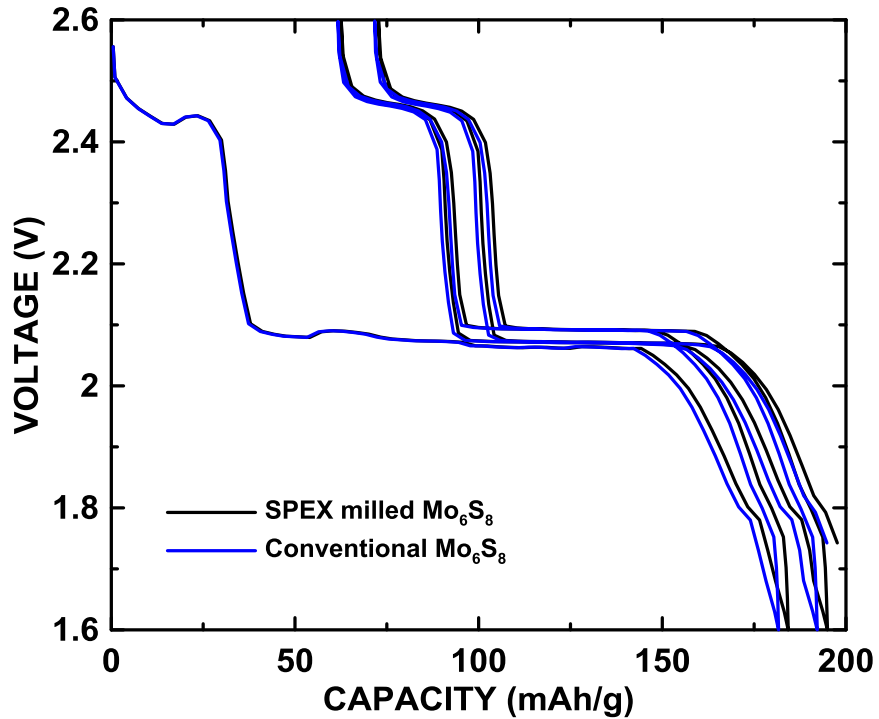

Figure 6.10: Voltage vs capacity curve of a Li/Mo_6S_8, high temperature solid state synthesis (blue), Spex milling method (black) 2-electrode Conflat cell with 1M $LiPF_6$ in 1:2 EC: DEC electrolyte at a C/10 rate at 60°C.
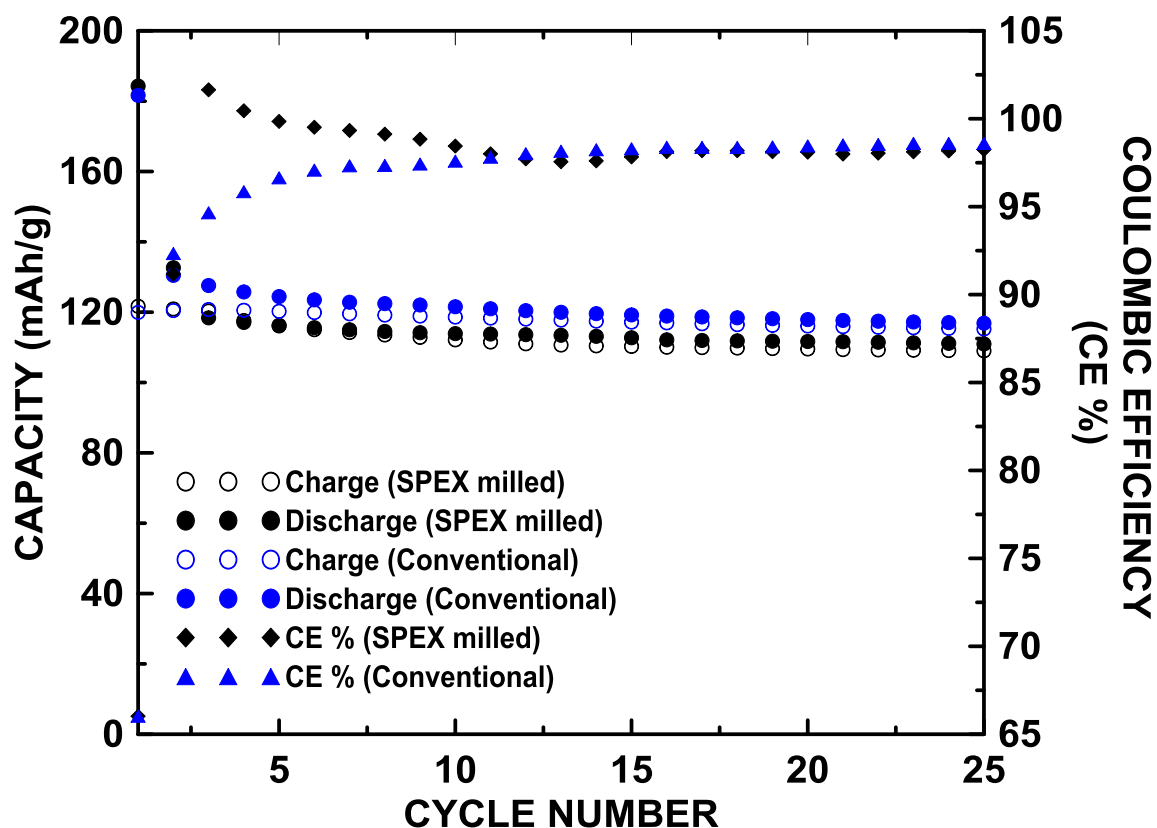
Figure 6.11: Cycling performance of a Li/Mo_6S_8, high temperature solid state synthesis (blue circles), Spex milling method (black circles), coulombic efficiency of a Li/Mo_6S_8, high temperature solid state synthesis (blue triangles), Spex milling method (black diamonds) 2-electrode Conflat cell with 1M $LiPF_6$ in 1:2 EC: DEC electrolyte at a C/10 rate at 60°C.

Figure 6.12 and 6.13 shows the voltage profile and the cycling performance of a Mg/Mo_6S_8 (from Spex milled $Cu_2Mo_6S_8$) 2-electrode coin half-cell cycled at 30°C. The first discharge consists of a single plateau of ~100 mAh/g capacity corresponding to the insertion of two formula units of Mg into Mo_6S_8. At 30°C only one Mg ion can reversibly be intercalated into Mo_6S_8 crystal structure due to its poor intercalation kinetics at low temperature. The same phenomenon was observed with Mo_6S_8 prepared by conventional high temperature solid state synthesis.[80] Therefore as shown in Figure 6.12, a reversible

capacity of 50 mAh/g was observed during subsequent cycling along with a single plateau at 1.1 V.

At ambient temperature, reversible magnesium insertion into Mo_6S_8 Chevrel phase can be described as follows:
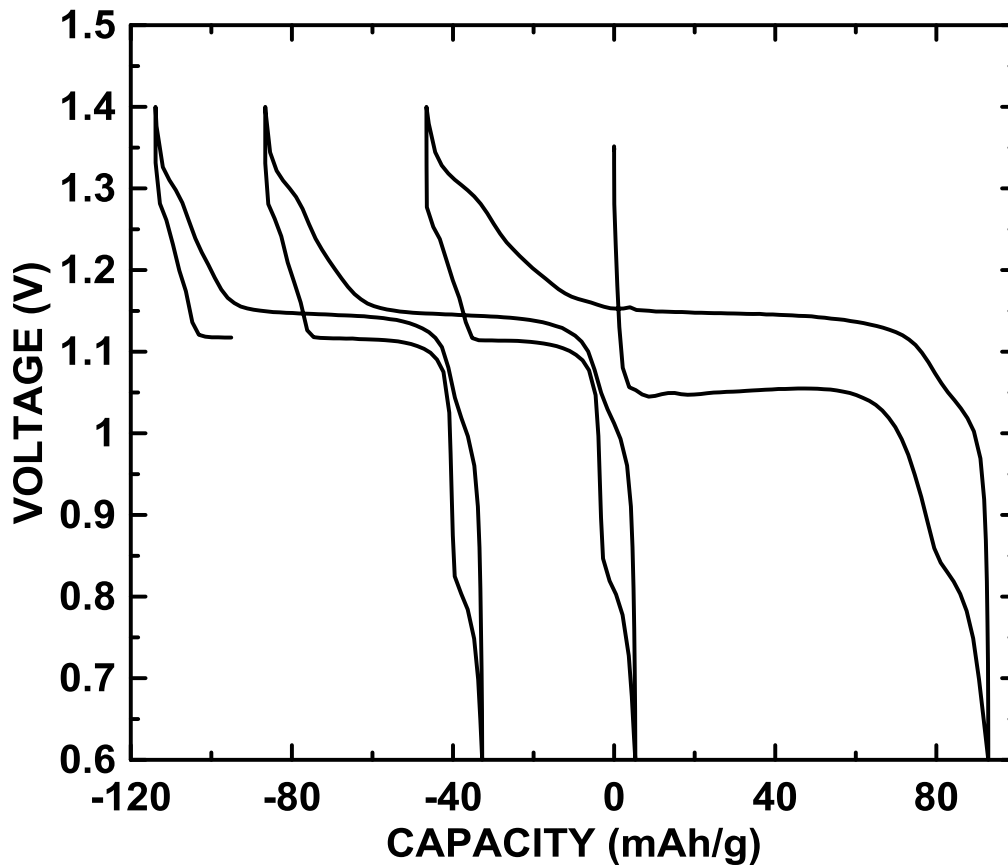
$$Mg^{2+} + Mo_6S_8 + 2e^- \rightleftharpoons MgMo_6S_8 \qquad (6.5)$$

Figure 6.12: Voltage vs capacity curve of a Mg /Mo_6S_8 coin-half cell with 0.5M EtMgCl in THF (1:2 AlCl$_3$: EtMgCl) electrolyte at a C/20 rate at 30°C.
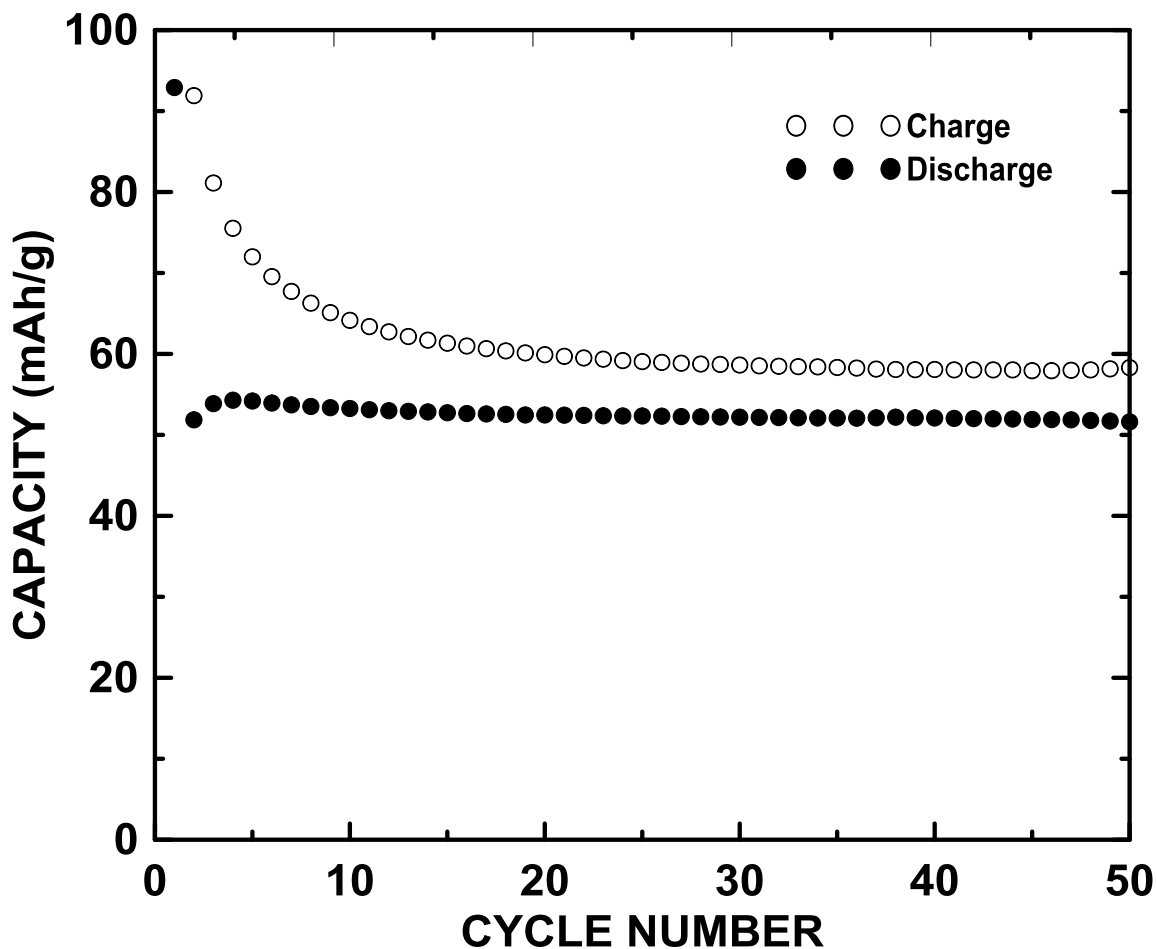
Figure 6.13: Cycling performance of a Mg /Mo$_6$S$_8$ coin-half cell with 0.5M EtMgCl in THF (1:2 AlCl$_3$: EtMgCl) electrolyte at a C/20 rate at 30°C.

The poor coulombic efficiency and the electrode slippage during cycling were suspected to be caused by electrolyte decomposition reactions that consume the Mg ions continuously. Even though Mg is being irreversibly consumed by the side reactions, no significant capacity loss was observed due to the continuous supply of Mg from the CE/RE. Subsequently, it was found that the Grignard electrolyte did not perform well and it may have caused poor coulombic efficiency as well.

Similar to Mo$_6$S$_8$ prepared by conventional high temperature solid state synthesis, the particle size of Mo$_6$S$_8$ prepared by Spex milling method was also reduced by

autogrinding at 580 rpm for 3 hours. The electrochemical performance of the composite electrodes fabricated from ground Mo_6S_8 (Section 3.4) was tested in a $Mo_6S_8/Mg/Mo_6S_8$ 3-electrode full cell with 0.5M $Mg(TFSI)_2$ in ACN. As shown in Figure 6.14, the irreversible capacity and the polarization of the cell are higher than that of the cell cycled with Mo_6S_8 prepared by conventional high temperature solid state synthesis
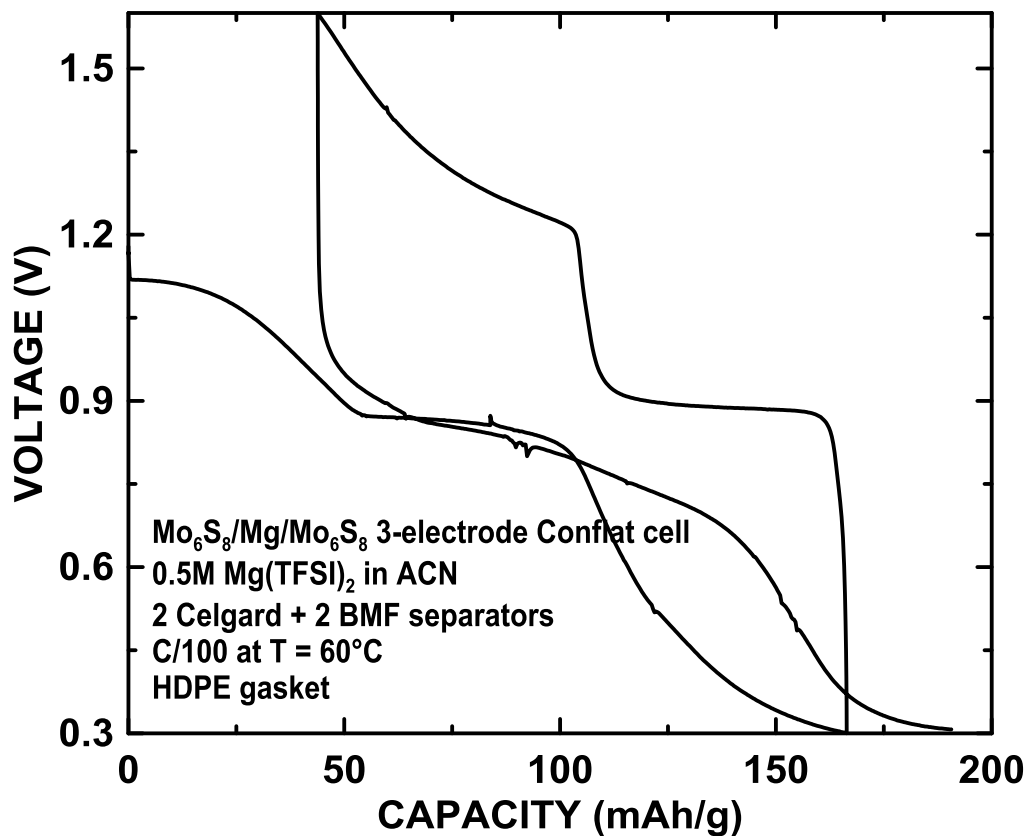

Figure 6.14: Voltage curve of a Spex milled Mo_6S_8 in $MgMo_6S_8/Mg/Mo_6S_8$ 3-electrode Conflat cell with a HDPE gasket in 0.5M $Mg(TFSI)_2$ in ACN electrolyte cycled at $60^{\circ}C$ at C/100 rate.

6.3 Electrochemical Performance of Grignard Reagent

Due to the poor coulombic efficiencies observed with Spex milled Mo_6S_8 cycled in Grignard reagent, the reagent was tested again with Mo_6S_8 prepared by by conventional high temperature solid state synthesis, leaching, and autogrinding, as described in Section 6.1.3. Irrespective of the type of synthesis or particle size, same electrochemical performance was observed with the Grignard reagent.

Figure 6.15 (a) and (b) compares the electrochemical behaviour of 0.5M EtMgCl in THF in a Mg/SS 2-electrode Conflat cell cycled with and without $AlCl_3$ in the electrolyte. Contradictory to previous studies,[5] Mg could not be efficiently plated and stripped on a SS electrode in a 0.5M EtMgCl in THF electrolyte solution with $AlCl_3$. This could have led to the poor electrochemical performance of Mo_6S_8 observed in the previous section. The cell without $AlCl_3$ cycled much efficiently compared to that of the cell with $AlCl_3$. The reason for such behaviour is still not clear.
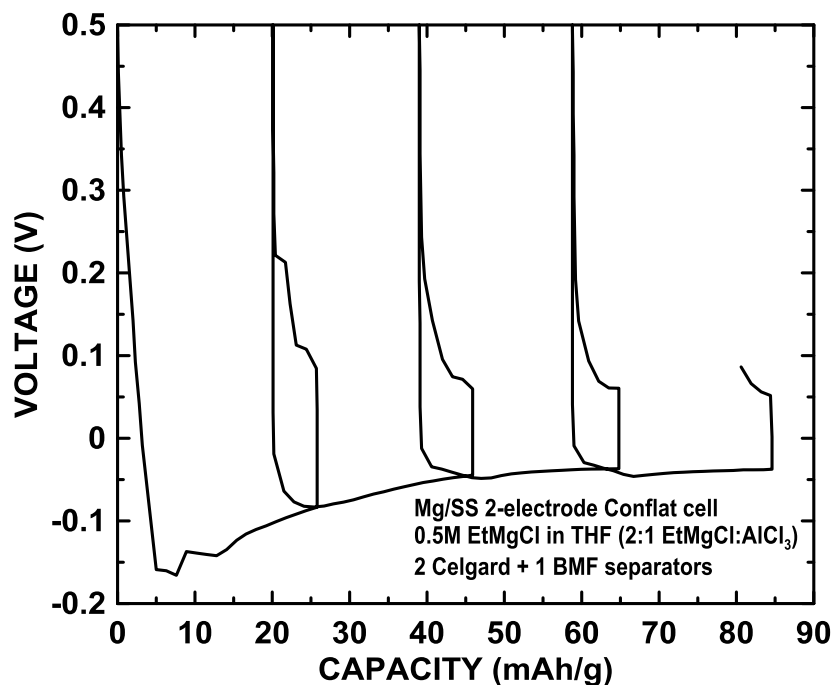
Figure 6.15 (a): Voltage vs capacity curve of a Mg /SS 2-electrode Conflat cell with 0.5M EtMgCl in THF (1:2 AlCl$_3$: EtMgCl) electrolyte at 60°C.
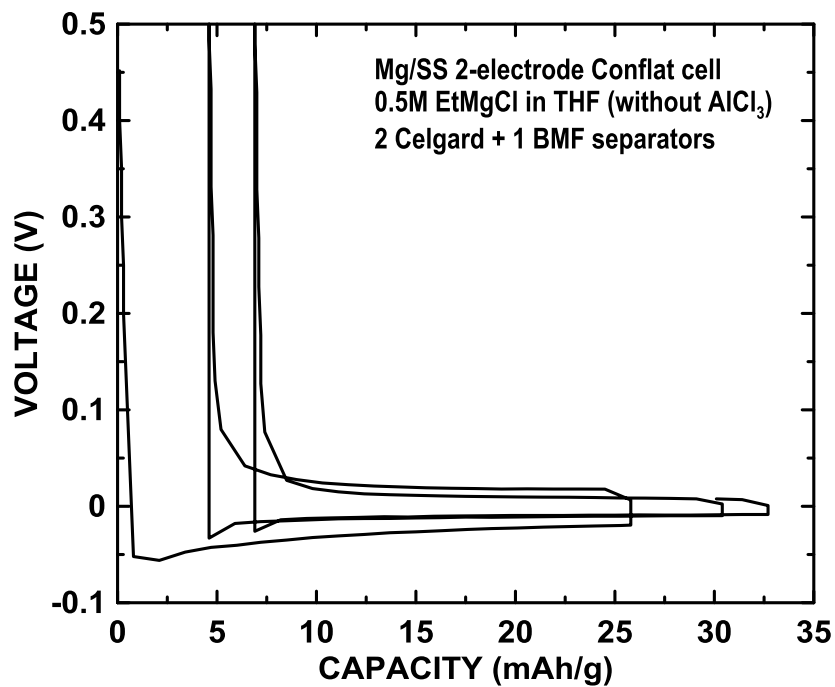

Figure 6.15 (b): Voltage vs capacity curve of a Mg /SS 2-electrode Conflat cell with 0.5M EtMgCl in THF (without AlCl$_3$) electrolyte at 60°C.

6.4 Conclusions

Even though Mo_6S_8 Chevrel compound prepared by conventional high temperature method showed good cycling performance with Li, poor intercalation kinetics was observed with Mg. This was later overcome by reducing the particle size and thereby improving the kinetics of the material. The latter developed Spex milling synthesis method reduced the $Cu_2Mo_6S_8$ synthesis duration from 160 hours to 24 hours compared to that of conventional high temperature solid state synthesis process. The XRD pattern for leached Mo_6S_8 made by Spex milling method agreed well with the reference pattern confirming the absence of any impurities or secondary phases. The electrochemical performance of Spex milled Mo_6S_8 with Li is similar to that of regular Mo_6S_8, while poor coulombic efficiencies were observed with Mg which is suspected to be due to the issues with Grignard reagent as described above. In addition, the autoground Mo_6S_8 prepared by Spex milling method showed high irreversible capacity and polarization with $Mg(TFSI)_2$ in ACN, compared to that of Mo_6S_8 prepared by conventional high temperature synthesis.

CHAPTER 7   CONCLUSIONS

Mg batteries are considered as an alternative to current state of art Li-ion batteries, primarily owing to their potential low cost and the high volumetric energy density of Mg. Nevertheless, Mg battery technology is still in its infancy due to the lack of appropriate cathode and anode materials with high energy densities and electrolyte systems with broad potential windows. The Mo_6S_8 Chevrel phase compound has shown high reversibility for Mg intercalation. It was shown in this project that it is suitable for use as a counter electrode in cells to test new materials. In order to test new materials and electrolyte systems, a stable 3-electrode cell is furthermore required. This thesis work focused on several objectives including the development of a rigid 2 and 3- electrode cell design that can be used as a test vehicle for battery research; the investigation of new anode materials for Mg batteries; and the development of a time efficient method to synthesize Mo_6S_8 Chevrel and to explore potential electrolyte systems for Mg batteries.

The new cell design presented in this thesis based on Conflat vacuum fittings provides a unique opportunity to evaluate ambient and high temperature electrochemical properties of new electrode materials and electrolytes. Conflat cells are excellent low cost cells that use readily available parts. They are simple to assemble into 2 and 3-electrode cell configurations in a reproducible fashion. They are particularly useful for high temperature studies as their operational reliability was demonstrated at temperatures up to 200°C. Conflat cells can be considered as an excellent alternative to coin cell and Swagelok cell hardware, especially in Mg battery research where the electrolyte is volatile and moderately high temperatures are used.

Even though rechargeable Mg batteries have been long considered as a promising technology for energy storage and conversion applications, the use of Mg metal is limited by the properties of the metal electrolyte interface. In this work it was found that Mg reversibly inserts into sputtered Pb, forming Mg_2Pb in a 2-phase reaction. The theoretical capacity of Mg_2Pb alloy is 2316 Ah/L, which is the highest volumetric capacity reported for an Mg alloy. Moreove, this capacity occurs at a low average voltage of about 0.125 V. However, extremely poor coulombic efficiencies observed were indicative of electrolyte decomposition reactions at the Pb electrode surface during cycling. Improved electrolyte stability is required to enable the use of Pb electrodes in practical Mg cells.

One of the most reversible cathode material identified for rechargeable Mg batteries is Mo_6S_8 Chevrel phase compounds. Therefore, Mo_6S_8 was used as the CE in most of the research work carried out in this thesis. The Mo_6S_8 Chevrel is a metastable phase at room temperature and can only be prepared indirectly by leaching intercalated metal from a thermodynamically stable fully intercalated compound such as $Cu_2Mo_6S_8$. Therefore, high temperature solid state synthesis method introduced by Kondo et al.[126] was used to synthesize $Cu_2Mo_6S_8$. Since this method is time consuming, an alternative method was introduced in this work to synthesize $Cu_2Mo_6S_8$ by SPEX milling within a shortened time frame.

From XRD measurements it was found that $Cu_2Mo_6S_8$ prepared by Spex milling method and its leached product were well associated with the corresponding reference patterns. The electrochemical performance of Spex milled Mo_6S_8 with Li was similar to that of regular Mo_6S_8 prepared by high temperature solid state synthesis. However, poor coulombic efficiencies were observed in Mg cells. This was suspected to be caused by

95

the issues associated with Grignard electrolyte used. Unlike the Mo_6S_8 prepared by conventional solid state synthesis, the autoground Mo_6S_8 prepared by the Spex milling method showed high irreversible capacity and polarization when cycled with $Mg(TFSI)_2$ in ACN. Therefore, the Spex milling method might require further modifications to obtain Mo_6S_8 with good cycling capability with Mg.

CHAPTER 8   FUTURE WORK

8.1 Electrolyte Study for Rechargeable Magnesium Batteries

8.1.1 Introduction

One of the major reasons for practical rechargeable Mg batteries have not yet been developed is the lack of electrolytes with wide electrochemical windows that are capable of reversible Mg deposition and dissolution. Generally, the voltage stability of an electrolyte solution is determined in terms of its susceptibility to oxidise or/and reduce in the presence of an, oxidizing agent (cathode) or a reducing agent (anode). Therefore, one of the major approaches in developing rechargeable Mg batteries is to develop a practical electrolyte system.

Considering the fact that Mg is reactive with water, aqueous electrolyte solutions are eliminated.[82] In addition, metallic Mg spontaneously forms a passivating surface film in most commonly used polar aprotic organic solvent based electrolytes containing ionic salts, such as: magnesium BF_4^-, ClO_4^- or PF_6^-.[64] Unlike the ionically conducting and electronically insulating SEI formed on Li metal, this blocking surface film is both electronically and ionically insulating. In the 1920s, Jolibois et al.[89] showed efficient Mg deposition in ethereal solutions of Grignard reagents (RMgX). It was found that Mg electrodes are always bare and non-passivated in these systems.[78] Nevertheless, their poor anti oxidation capability restrict the use of Grignard reagents in practical batteries.

Later, Gregory et al.[9] suggested that magnesium organobortaes ($Mg[B(R_2'R_2'')]_2$, R = alkyl or aryl group) in ethereal solutions are potential candidates for rechargeable Mg batteries. The magnesium borate complexes used for this study were synthesized by a reaction between an organomagnesium (R_2Mg) base and a Lewis acid (BR_3). They

investigated the performance of magnesium dibutyldiphenylborate ($Mg[B(Bu_2Ph_2)]_2$) in 7:3 volumetric mixture of THF:DME with a $Mg_xCo_3O_4$ cathode vs a Mg metal anode. Their work showed an improvement in electrochemical stability of the electrolytes based on magnesium borate complexes. The low anodic stability of Grignard reagents is resulted by the highly oxidizable C-Mg bond in RMgX complexes.[129] Based on the improved anodic stability exhibited by $Mg[B(R_2{}'R_2{}'')]_2$, it was assumed that the character of Lewis acid, BR_3, would be the key factor in determining the potential stability of the electrolyte. It was explained that the electron withdrawing nature of the Lewis acid increases the Mg-C bond length of R_2Mg, which partially increases the ionic character and thereby reduces its susceptibility towards oxidation.

Based on this hypothesis, Aurbach et al. investigated the effect of different combinations and ratios of R_2Mg Lewis base to $AX_{3-n}R_n$ Lewis acid (where A = Al, B, As, P, Sb, Ta, Fe and X = Cl, Br, F and R = alkyl or aryl groups).[82] They synthesized a series of $Mg(AX_{4-n}R_n)_2$ complexes by reacting R_2Mg and $AX_{3-n}R_n$ while gradually increasing the Lewis acid character to optimize the C-Mg bond. In addition, they also tested THF solutions of Bu_2Mg as a Lewis base with Lewis acids, such as: BPh_2Cl, $BPhCl_2$, $B[(CH_3)N]_3$, BEt_3, BBr_3, BF_3, $SbCl_3$, $SbCl_5$, PPh_3, PEt_2Cl, $AsPh_3$, $FeCl_3$ and TaF_3.[82] Surprisingly, they observed no reversible Mg deposition. However, $Mg(AlCl_2BuEt)_2$ complex synthesized by reacting Bu_2Mg: $AlCl_2Et$ in 1:2 ratio showed most promising results. It showed an anodic stability of 2.4 V and an almost 100% coulombic efficiency.[5,91,92] Surface analysis of Mg films deposited from this electrolyte has shown it does not develop a stable passivating film. Such electrolytes are known as first generation of Mg electrolytes. The main limitation of first generation magnesium

organohaloaluminate electrolytes is their electrochemical instability caused by the weak Al-C bond that breaks via β-hydride elimination.[130]

This led to the introduction of second generation of Mg electrolytes. Here, the electrochemical stability was improved by substituting the alkyl groups with phenyl groups, thereby excluding β-hydride elimination. The $Mg(AlCl_2Ph_2)_2$ complex synthesized by reacting 1:2 ratio of $AlCl_3$: PhMgCl was reported to have an electrochemical window of 3.3 V vs Mg on a Pt WE.[58] Despite the high reversibility of these electrolyte systems, they all have common drawbacks, such as: their high nucleophilicity, high vapour pressure and sensitivity towards air/moisture causing potential safety issues. The high nucleophilicity of magnesium organohaloaluminate electrolytes restricts their application in batteries with electrophilic cathodes, such as sulfur or air. For example, it was found that $Mg(AlCl_2Ph_2)_2$ electrolyte directly reacts with sulfur to form phenyl disulphide and biphenyl sulfide.[131]

As an inert polar aprotic solution, ionic liquids are considered as a potential candidate for reversible Mg electrochemistry. Amir et al.[78] studied the possibility of using ionic liquids, such as ethylmethylimidazolium, butylmethylimidazolium tetrafluoroborate ($BMImBF_4$) and trihexyl(tetradecyl)phosphonium bis(trifluoromethylsulfonyl)imide as electrolytes in Mg batteries. These electrolytes further comprised Mg salts, such as: $MgCl_2$, $Mg(CF_3SO_3)_2$, $Mg(ClO_4)_2$ and $Mg(C_4H_9)_2$. They reported that none of these systems were capable of reversible Mg deposition and dissolution even with high Mg salt concentrations. Cyclic voltammetry studies of these electrolyte systems showed a pronounced cathodic process during the initial cycling, indicating Mg deposition. The lack of a corresponding anodic process signified the irreversible nature of Mg deposition

and dissolution in these systems. Also the decay in cathodic current observed with consecutive cycling was suggested to be due to the passivation of the electrode. Based on their study, it was concluded that derivatives of imidazolium salts are reactive with Mg deposits, and an unavoidable passivation occurs due to the reactions of Mg with inevitable traces of impurities such as moisture.

In addition, as described in Section 2.4.3, Doe et al. reported an inorganic Mg salt capable of highly reversible Mg electrodeposition with an electrochemical stability close to 3 V vs Mg at room temperature.[67] As shown in reaction 7.1, these inorganic Mg salts were synthesized by the acid-base reaction between $MgCl_2$ and $AlCl_3$. They were tested in a variety of solvents including ethereal solutions, such as THF, DME and higher glymes.

$$m MgCl_2 + n AlCl_3 \rightleftharpoons Mg_m Al_n Cl_{[(2*m)+(3*n)]} \qquad (7.1)$$

Despite the high reversibility and improved electrochemical window of these electrolyte systems, they are still composed of highly volatile solvents which are difficult to apply in practical applications. Recently, the electrochemical behaviour of $Mg(TFSI)_2$ salt in glyme/diglyme solvent system was reported.[94] It has shown excellent anodic stability and reduced corrosive nature with stainless steel and Al (exceeding 4 V vs Al) current collectors and excellent compatibility with high voltage cathodes such as poly(2,2,6,6-tetramethyl-piperidinyl-1-oxy-4-yl methacrylate).

In this chapter, preliminary research on potential electrolyte systems for rechargeable Mg batteries will be discussed. This is currently a work in progress. Wherever possible, an explanation for the observed electrochemistry is given based on

the information available. Further experiments are being conducted, as described below, to provide stronger justification for the models proposed.

8.1.2 Experimental

REs were punched from Mg foil (99.95%, 0.25 mm thick, Gallium Source, LLC, Scotts Valley, CA). Mo_6S_8 composite electrodes were prepared according to Section 3.4. They were punched into 18 mm diameter circles and magnesiated with 0.5M $Mg(TFSI)_2$ in ACN at C/50 rate at $60^{\circ}C$ in a 2-electrode Conflat cell with a Mg CE/RE electrode. Upon complete magnesiation of Mo_6S_8, the electrode was harvested and rinsed with dimethyl carbonate in an argon-filled glovebox. Either magnesiated Mo_6S_8 or Mg metal was used as the CE and stainless steel spacer (18 mm diameter and 3.3 mm thick) was used as the WE, respectively. All the cells were fabricated in a 3-electrode Conflat cell as described in Chapter 4. They were cycled with 0.5M and saturated concentrations of $Mg(TFSI)_2$ dissolved in ACN, adiponitrile (ADN, 99% Sigma Aldrich), pyridine (PY, 99.8% anhydrous, Sigma Aldrich), PC (BASF), DME (99.5% anhydrous, Sigma Aldrich) and diglyme (99.5% anhydrous, Sigma Aldrich) solvents. All the cells were fabricated in an argon-filled glovebox. Cyclic voltammograms (CVs) were measured as described in Section 3.3, in a temperature range of $40^{\circ}C$ to $150^{\circ}C$. The cell temperature was measured by a thermocouple attached to the cell with a heat conductive paste (Type Z9 Silicone heat sink compound, GC Electronics). All the CV plots shown below are the measurements taken between the SS (WE) vs Mg (RE).

8.1.3 Results and Discussion

Figure 8.2 shows the CVs of 0.5M $Mg(TFSI)_2$ in ACN at different temperatures. A small anodic peak was observed at ~3.8 V vs Mg at temperatures below $100^{\circ}C$. This

could either be due to Mg stripping or electrolyte oxidation. The increase in current at a potential of 5 V at all the temperatures is most likely caused by either corrosion of SS or oxidation of electrolyte, or combination of both phenomenon. The peak close to –2 V vs Mg is may be due to Mg plating or electrolyte reduction.

This is controversial with the previous galvanostatic measurements shown in the literature. It was reported that in a Mg/Mg/SS 3-electrode cell ACN was reduced at the WE at -0.2 V vs Mg to form a non-passivating/conductive surface film which mimics the effect of Mg reduction at WE surface.[69] It is possible that due to the relatively fast sweep rate used in this experiment, electrolyte decomposition isn't significant at temperatures below 80°C. This might be caused by its comparatively slow kinetics. Therefore, further investigations are required to be done in order to determine the capability of reversible magnesiation from ACN. For example, a slow sweep rate could be used to observe any appearance of new peaks due to electrolyte decomposition. Also, the linear sweep can be reversed at -1 V vs Mg to 5 V vs Mg in order to elucidate the origin of the anodic peak at 3.8 V. If the cathodic peak at -2 V vs Mg is caused by Mg plating, the above anodic peak should not be formed. However, in this study the peak at 0 V vs Mg at a temperature of 80°C and above is suspected to be caused by the electrolyte reduction on SS electrode. With increasing temperature severe electrolyte decomposition takes place giving rise to large currents.
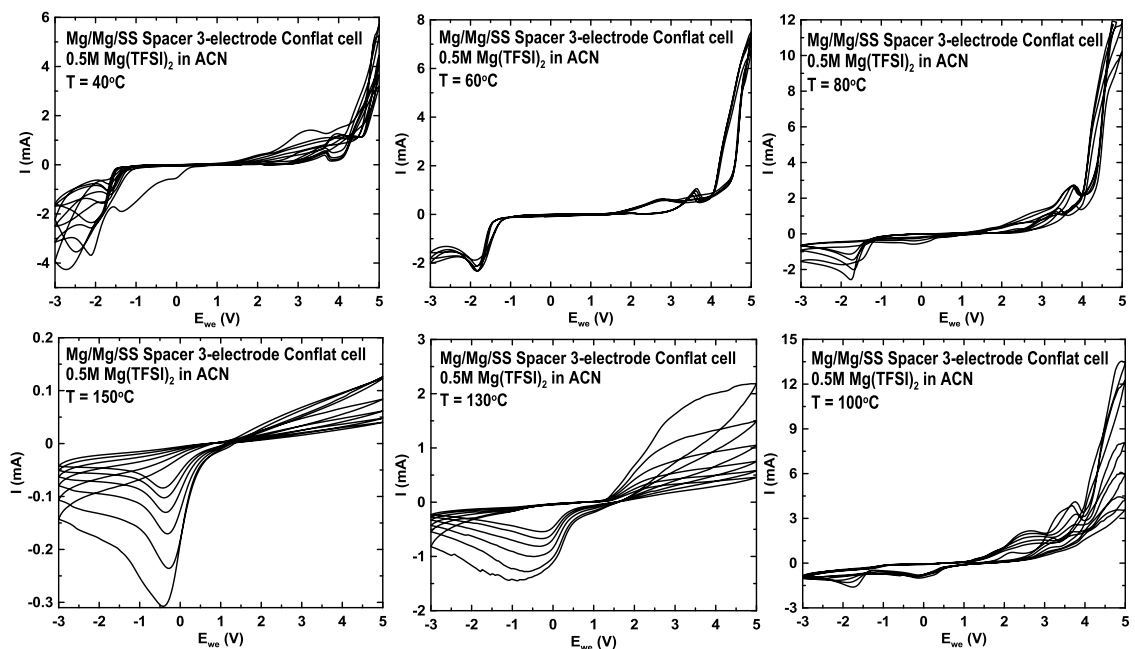
Figure 8.2: Cyclic voltammetric measurements of Mg/Mg/SS with 0.5M Mg(TFSI)$_2$ in ACN at different temperatures.

Figure 8.3 shows the CVs for 2M (saturated concentration) Mg(TFSI)$_2$ in ACN at different temperatures. At 40°C instead of Mg stripping or plating, a significant electrolyte reduction was observed at about zero potential. If this feature was caused Mg plating, a corresponding anodic peak could be expected due to Mg stripping. The absence of such an anodic peak led to the assumption that the peak observed at zero potential is due to electrolyte reduction. In addition, the first cycle at 60°C also showed a peak corresponding to possible electrolyte reduction which completely disappeared during the next consecutive cycles. This was suspected to be due to the formation of passivation layer by the deposition of the reduced electrolyte products on the SS WE.

The small anodic peak observed close to 2 V at temperatures below 130°C is suspected to be caused by Mg stripping as this is reversibly in correspondence with the cathodic peak observed at -2 V (vs Mg) that was deduced due to Mg plating in Figure

8.2. The same experiments suggested for 0.5M Mg(TFSI)$_2$ in ACN can be applied here to confirm the ability of reversible magnesiation. As reported in the literature, the sudden increase in current at ~3 V vs Mg is due to probable corrosion of SS WE.[69] The decaying cathodic current obtained during the cycling at all temperatures indicates the passivation of SS electrode, causing Mg plating on WE to become difficult. Based on these preliminary data, saturated Mg(TFSI)$_2$ in ACN is more stable at high temperatures than 0.5 M Mg(TFSI)$_2$ in ACN as electrolyte reduction was not observed until 130°C.
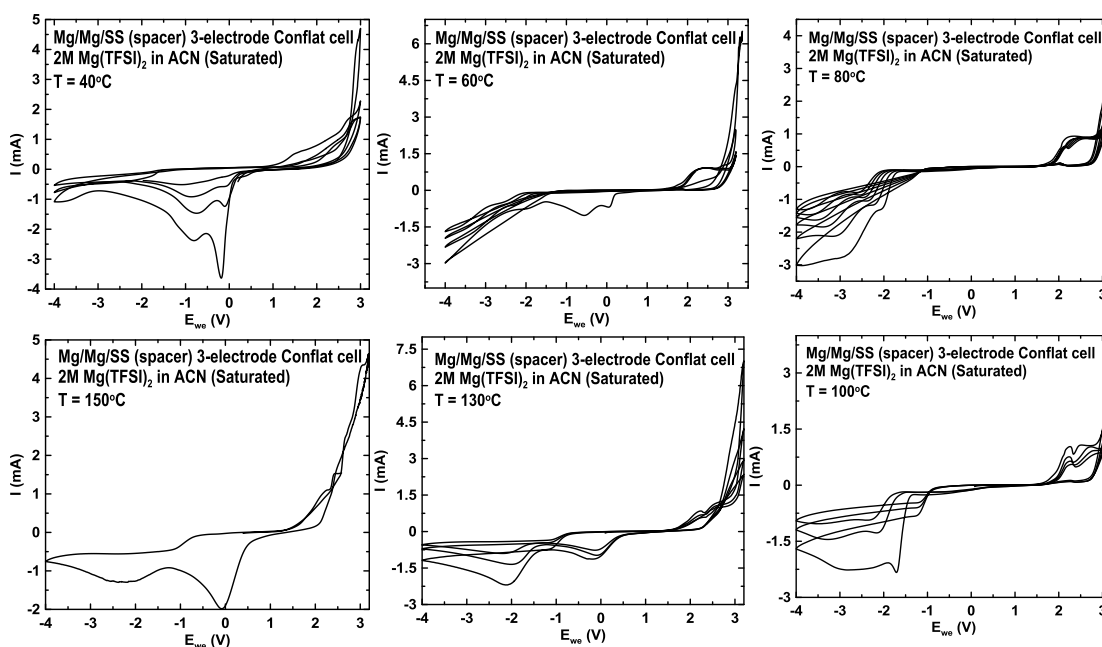
Figure 8.3: Cyclic voltammetric measurements of Mg/Mg/SS with 2M Mg(TFSI)$_2$ in ACN at different temperatures.

When CVs of Mg/Mg/SS 3-electrode cells were attempted with Diglyme, ADN, DME, PC and PY solvents large reducing potentials (< -5 V vs Mg) were confronted at the CE, which were outside the operational range of the potentiostat. Therefore, magnesiated Mo$_6$S$_8$ was used as the CE, which was found to be reasonably non-polarizable in the electrolytes tested.

Figure 8.4 shows CVs of a $MgMo_6S_8$/Mg/SS 3-electrode cell cycled with 0.5M

$Mg(TFSI)_2$ in diglyme in a potential range of -1 V to 2.5 V. The cathodic peak obtained

at the potential of -0.5 V could be from either Mg plating or electrolyte reduction. The

peak at a potential of ~0.6 V could have resulted by either Mg stripping or electrolyte

oxidation. The peaks at high potential are believed to be generated by oxidation reactions

of the electrolyte or corrosion of the CE current collector/cell can. The absence of a

significant decay in electrode current might be due to two reasons: (1) capability of

reversible Mg deposition and dissolution of the electrolyte system, (2) absence of a

passivation film (blocking layer) if the electrolyte decomposition products are soluble. At

temperatures above $80^{\circ}C$, the electrolyte decomposition reactions are dominant. The

noise observed at elevated temperatures could be due to the formation of gaseous

products as result of severe electrolyte decomposition. However, recently the Lee group

reported that pure glyme or diglyme solvents were incapable of generating an anodic

current on the SS WE with Mg CE/RE. They speculate that this is most likely due to the

formation of passivation layer by reactions with the solvent.[94] Therefore, it would be very

interesting to further investigate the reversibility of the above solvent system.
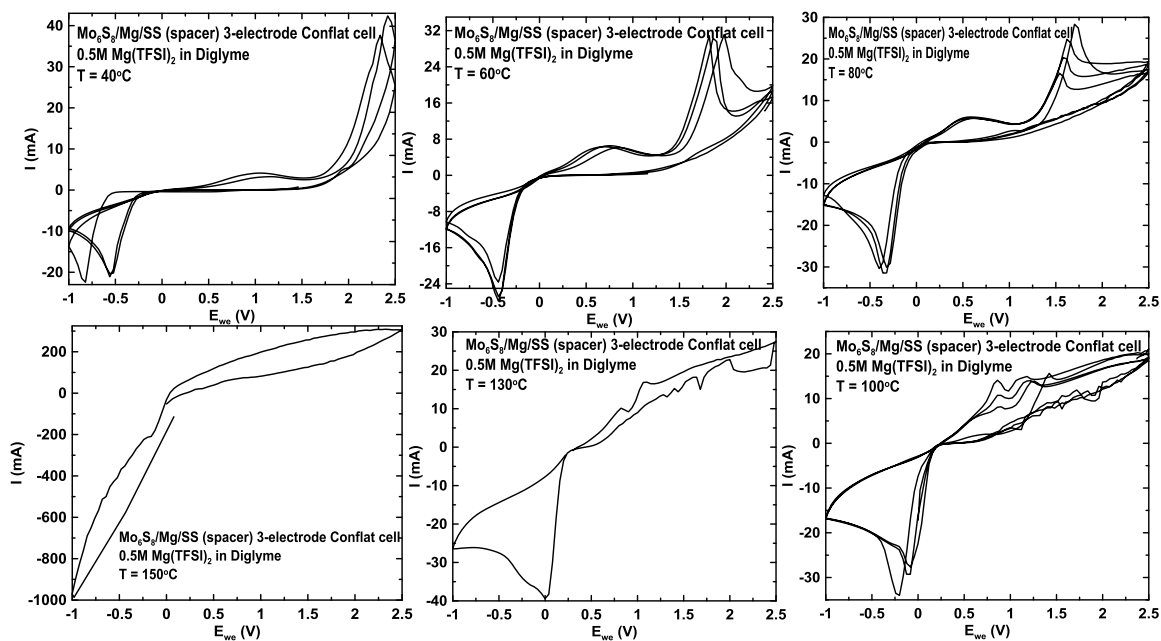
Figure 8.4: Cyclic voltammetric measurements of $Mg_xMo_6S_8$/Mg/SS with 0.5M $Mg(TFSI)_2$ in diglyme at different temperatures.

As shown in Figure 8.5, with 1M (saturated concentration) $Mg(TFSI)_2$ in diglyme the anodic peak previously observed in Figure 8.4 at 0.6 V vs Mg was not noted. Instead, a low current was achieved at $40°C$ while a significant decay in current was observed at both $40°C$ and $60°C$. This could be due to the formation of an insulating film on SS WE. At temperatures above $60°C$ a large anodic current was encountered at the WE that could be due to severe electrolyte oxidation reactions, where the resulting currents were beyond the operational range of potentiostat. Therefore, the CV measurements for saturated $Mg(TFSI)_2$ in diglyme was limited to $60°C$.
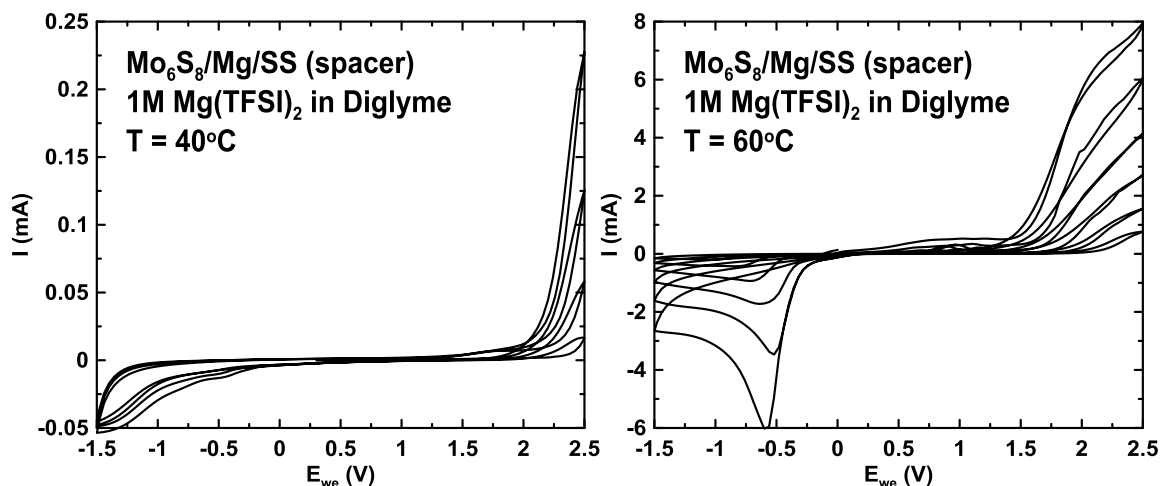
Figure 8.5: Cyclic voltammetric measurements of a $Mg_xMo_6S_8$/Mg/SS cell with 1M $Mg(TFSI)_2$ in diglyme at different temperatures.

The CV measurements for 0.5M $Mg(TFSI)_2$ in ADP are shown in Figure 8.6. With this electrolyte, electrolyte reduction reactions are suspected throughout the temperature range due to the peak observed at -0.4 V (vs Mg). With increasing temperature this peak becomes more significant due to increased rate of electrolyte decomposition reactions. The small peak observed at 2.1 V (vs Mg) could be due to either Mg stripping or decomposition of electrolyte. The increase in current at higher voltages is suspected to be due to the corrosion of the SS electrode. At 100°C the peak observed at 1.4 V (vs Mg) might also be a result of corrosion or electrolyte decomposition. The corresponding cathodic peak observed at -2.5 V (vs Mg) could be caused by either Mg plating or electrolyte reduction. Therefore, further experiments are required to confirm the reversibility of this electrolyte.
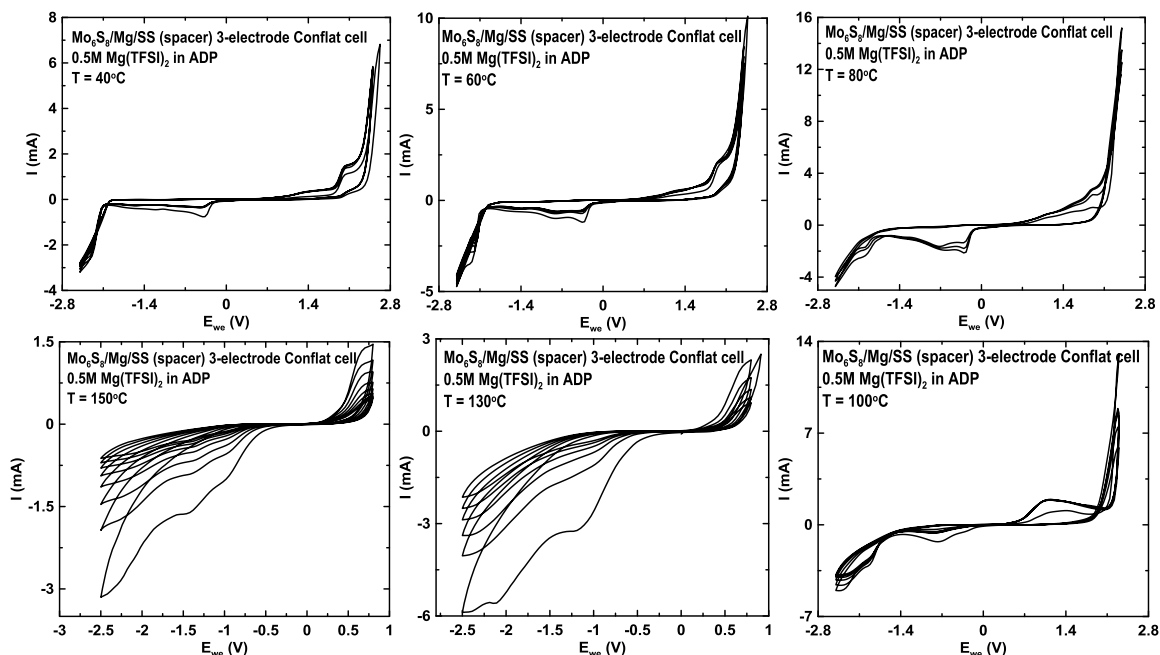
Figure 8.6: Cyclic voltammetric measurements of $Mg_xMo_6S_8/Mg/SS$ with 0.5M $Mg(TFSI)_2$ in ADP at different temperatures.

The CV measurements shown in Figure 8.7 for saturated 1M $Mg(TFSI)_2$ in ADP electrolyte are similar to that of the above concentration shown in Figure 8.6.
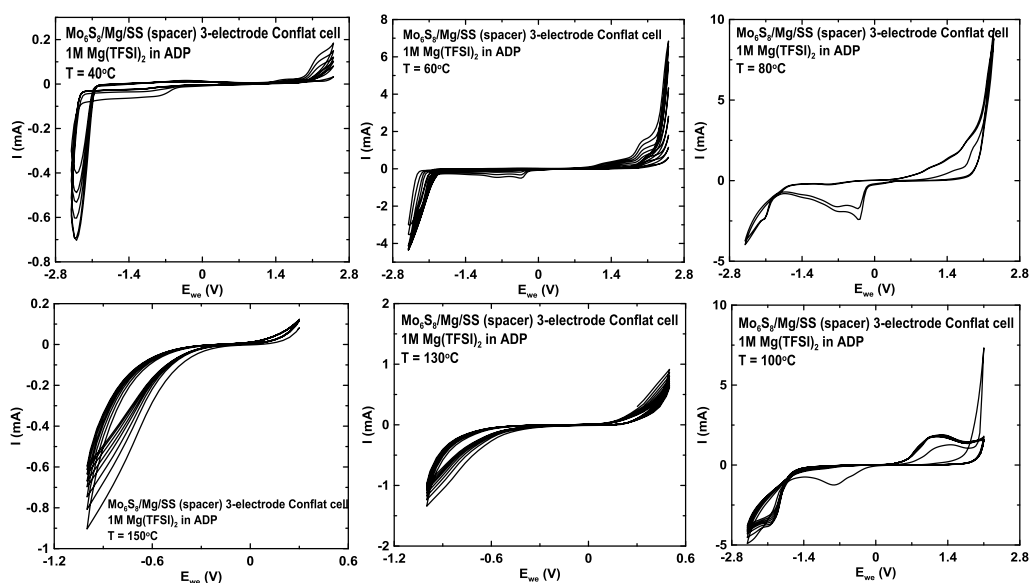
Figure 8.7: Cyclic voltammetric measurements for $Mg_xMo_6S_8/Mg/SS$ with 1M $Mg(TFSI)_2$ in ADP at different temperatures.

Figure 8.8 shows CVs of 0.5M Mg(TFSI)$_2$ in DME. At 40°C, the noticeably low decaying current attained at SS WE indicates that a passivation layer may be forming on WE surface, caused by the decomposition of electrolyte. At 60°C, the first few cycles show zero current over the sweeping potential range, which is the behaviour of a blocking electrode. However, in next consecutive cycles a cathodic peak at -2.8 V (vs Mg) appears which could be a result of Mg plating or electrolyte reduction. The CV measurements taken at 80°C and 100°C show a reversible cycling indicating a possible corrosion/electrolyte decomposition reaction at -1.6 V and 1.4 V vs Mg. At temperatures above 100°C the electrolyte decomposition reactions increases.
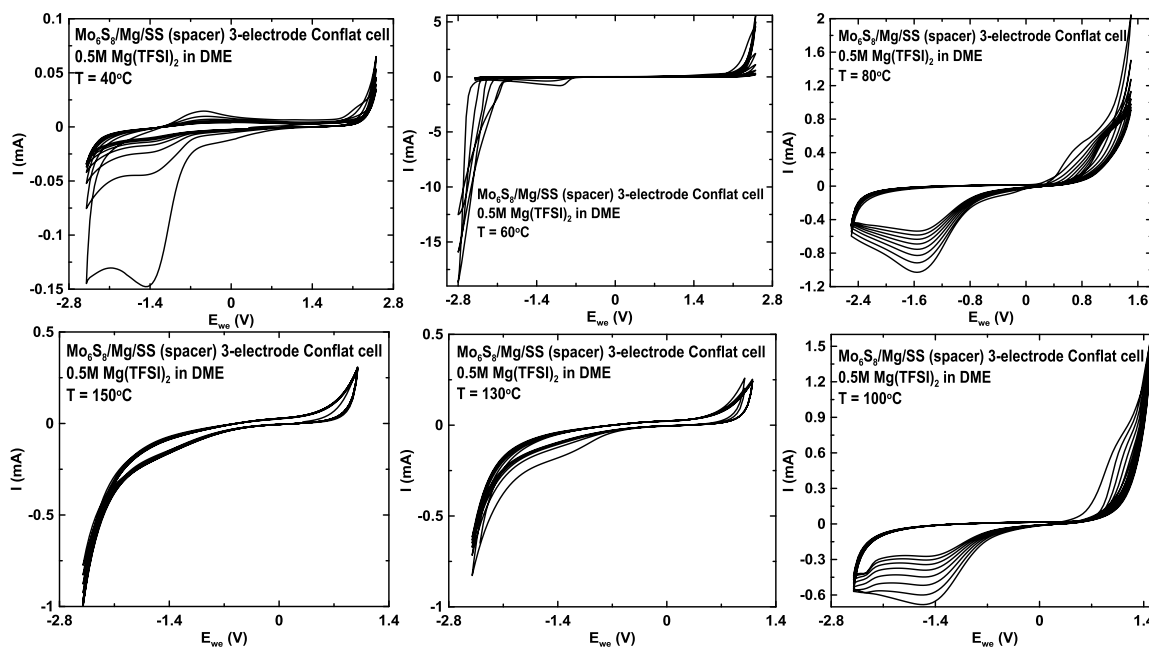
Figure 8.8: Cyclic voltammetric measurements for Mg$_x$Mo$_6$S$_8$/Mg/SS with 0.5M Mg(TFSI)$_2$ in DME at different temperatures.

Based on the CV measurements shown in Figure 8.9 for 0.5M Mg(TFSI)$_2$ in PC, it was found that PC is incapable of reversible Mg deposition and dissolution due to the formation of passivating film on WE surface. At temperatures below 80°C no current

corresponding to either Mg plating or stripping was observed. At 80°C and above, the peak obtained at -5 V vs Mg was suspected to be due to electrolyte reduction at SS electrode. The peak at -1.5 V (vs Mg) was most likely from the oxidation of reduced products on the WE surface.
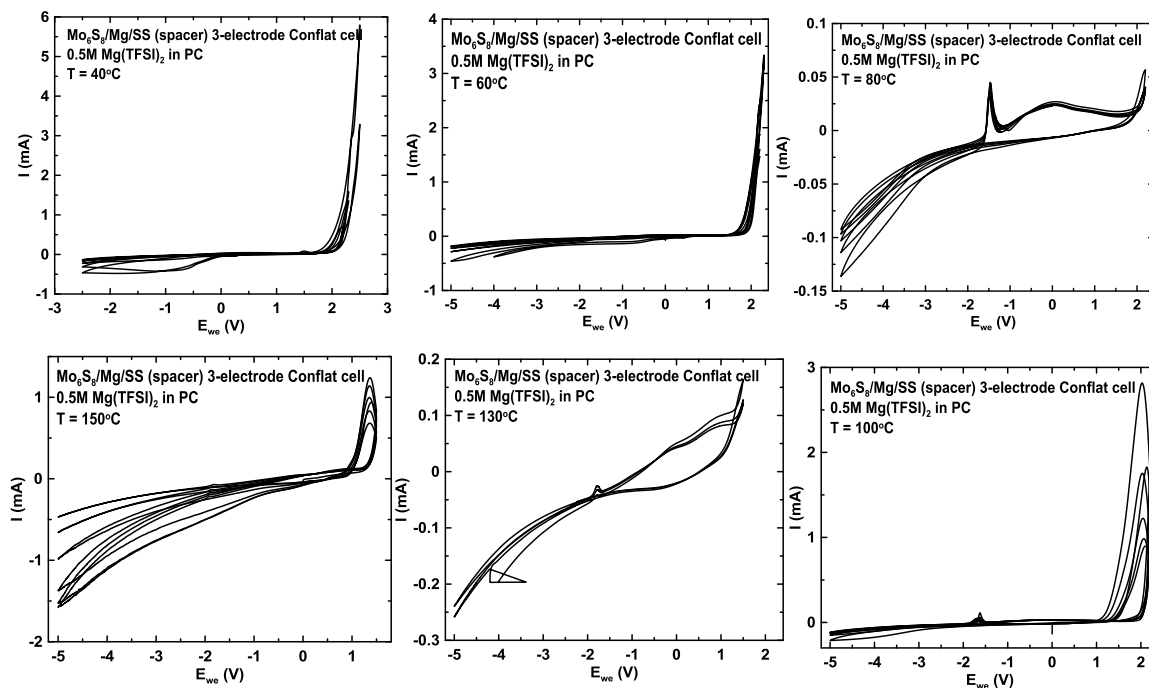
Figure 8.9: Cyclic voltammetric measurements for $Mg_xMo_6S_8/Mg/SS$ with 0.5M $Mg(TFSI)_2$ in PC at different temperatures.

As shown in Figure 8.10, CV data obtained for saturated 1M $Mg(TFSI)_2$ in PC is similar to that of above results shown in Figure 8.9, except at 80°C. At low temperatures, the current observed was very low indicating that no Mg deposition or dissolution taking place. However, at 80°C the cathodic and anodic peak achieved could be due to Mg plating and stripping. Further experiments are required (ex: SEM) to confirm its capability of reversible magnesiation. At 100°C the current at the SS electrode decays rapidly, showing evidence for the formation of a blocking surface film on the WE. At

elevated temperatures above 100°C, only the evidence for electrolyte decomposition was observed.
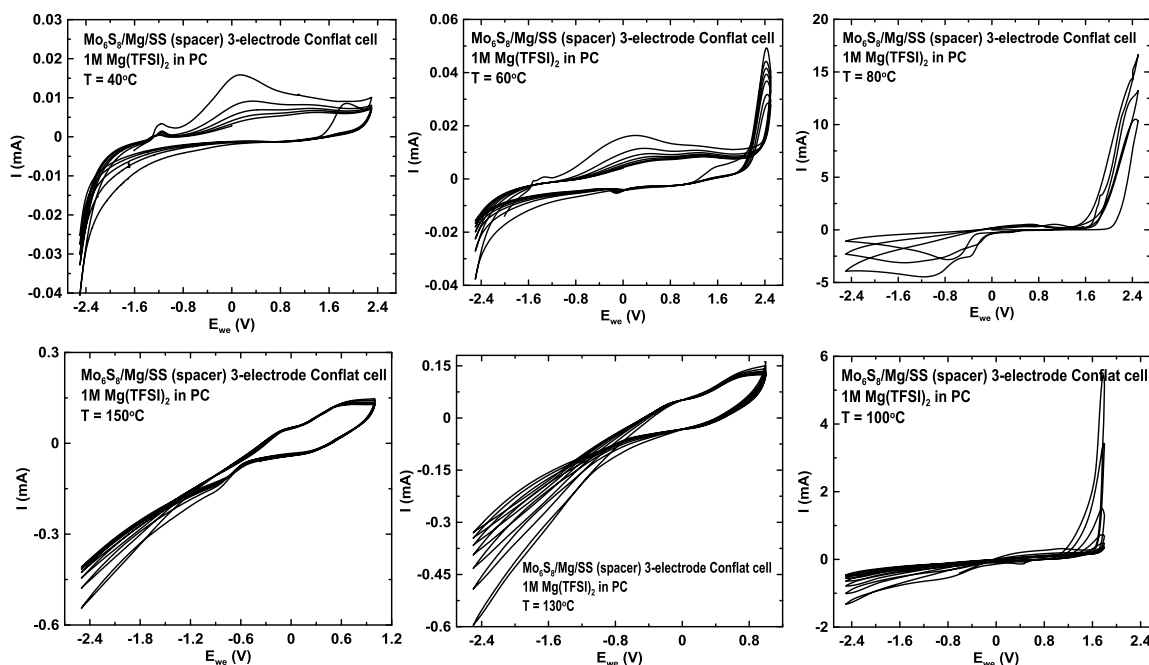
Figure 8.10: Cyclic voltammetric measurements for $Mg_xMo_6S_8$/Mg/SS with 1M $Mg(TFSI)_2$ in PC at different temperatures.

As shown in Figure 8.11, the CVs of 0.5M $Mg(TFSI)_2$ in PY did not show reversible magnesiation at temperatures below 130°C. The small two peaks observed at a potential of -1 V (vs Mg) at 80°C and 100°C were suspected to be from the reduction of electrolyte. The single peak at -0.5 V resulted from the oxidation of reduced products on the SS electrode as Mg stripping does not take place at a negative potential vs Mg. At 130°C, the reversible two peaks observed at -1 V and 1 V (vs Mg) could be from Mg plating and stripping. Like the other electrolyte systems, further investigations are required for this electrolyte to elucidate the origin of individual peaks in the CV. However, at temperatures above 130°C only electrolyte decomposition was observed.

111
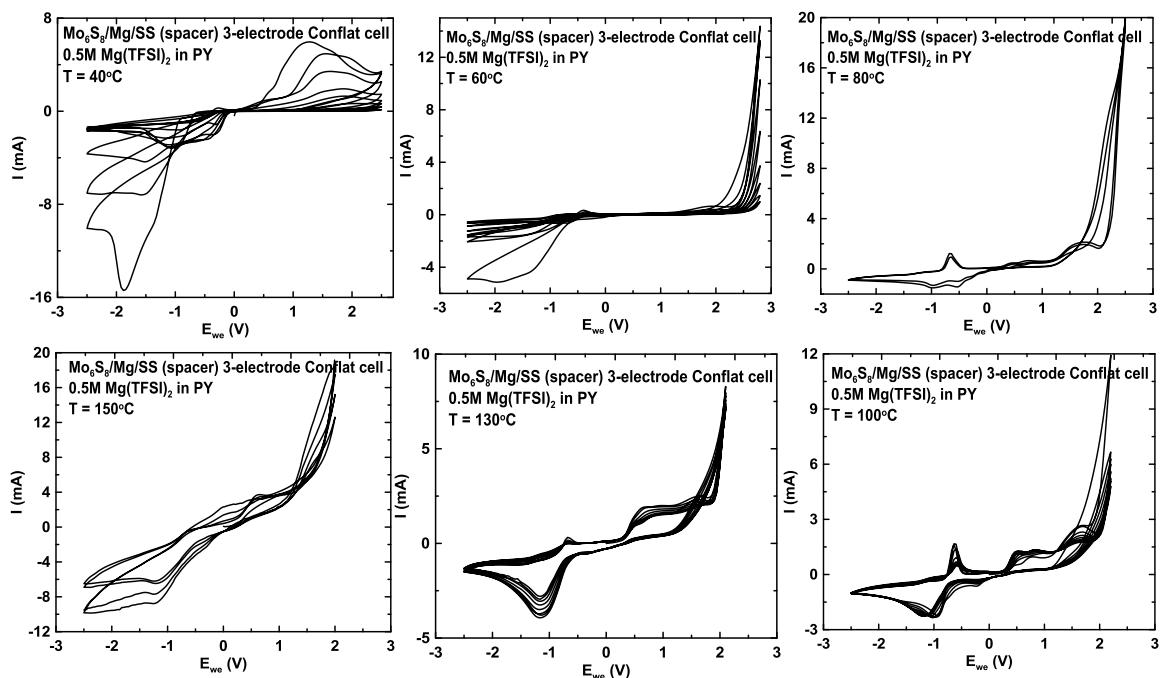
Figure 8.11: Cyclic voltammetric measurements of $Mg_xMo_6S_8/Mg/SS$ with 0.5M $Mg(TFSI)_2$ in PY at different temperatures.

8.2 Conclusions

This chapter presented some preliminary work that has been done on investigating the voltage stability of some electrolytes based on polar solvents and their ability to plate and strip Mg. Electrolyte solvents such as diglyme, adiponitrile, acetonitrile, 1, 2-dimethoxyethane showed corresponding cathodic and anodic peaks with $Mg(TFSI)_2$ at different temperatures that might be caused by either reversible magnesiation or electrolyte decomposition reactions. In order to confirm the actual reversibility of Mg deposition and dissolution in these electrolytes further experiments must be conducted. In order to study potential cathode materials at high potentials and thereby to achieve high energy densities, it is important to develop new electrolyte systems with wide electrochemical windows for rechargeable Mg batteries.

112

BIBILOGRAPHY

1. Linden D. Thomas Reddy, Handbook of Batteries, 4th editio, McGraw-Hill, (2011).

2. A. Khaligh, Z. Li, *IEEE Transactions on Vehicular Technology*, **59** (6) , 2806 (2010).

3. E. Levi, Y. Gofer, D. Aurbach, *Chemistry of Materials*, **22** (3) , 860 (2010).

4. M. Vreeke, D. Mah, C. Doyle, *Journal of The Electrochemical Society*, **145** (10) , 3668 (1998).

5. D. Aurbach, Z. Lu, A. Schechter, Y. Gofer, H. Gizbar, R. Turgeman, Y. Cohen, M. Moshkovich, E. Levi, *Nature*, **407** (6805) , 724 (2000).

6. N. Petr, R. Imhof, O. Haas, *Electrochimica Acta*, **45** , 351 (1999).

7. D. Archer, A. Ganopolski, *Geochemistry, Geophysics, Geosystems*, **6** (5) (2005).

8. Y. Gofer, R. Turgeman, H. Cohen, D. Aurbach, *Langmuir*, **19** (6) , 2344 (2003).

9. T.D. Gregory, R.J. Hoffman, R.C. Winterton, *Journal of The Electrochemical Society*, **137** (3) (1990).

10. Y. NuLi, J. Yang, J. Wang, Y. Li, *The Journal of Physical Chemistr*, 12594 (2009).

11. Z. Huang, T. Masese, Y. Orikasa, T. Mori, T. Minato, C. Tassel, Y. Kobayashi, H. Kageyama, Y. Uchimoto, , 11578 (2014).

12. M. Höök, X. Tang, *Energy Policy*, **52** , 797 (2013).

13. C.E. Sandy Thomas, *International Journal of Hydrogen Energy*, **34** (23) , 9279 (2009).

14. D. Aurbach, A. Zaban, A. Schechter, Y. Ein-eli, E. Zinigrad, B. Markovsky, *Journal of the Electrochemical Society*, **142** (9) (1995).

15. D. Hermance, S. Sasaki, *IEEE Spectrum*, **35** (11) , 48 (1998).

16. V. Neburchilov, H. Wang, J.J. Martin, W. Qu, *Journal of Power Sources*, **195** (5) , 1271 (2010).

17. M. Winter, J.O. Besenhard, M.E. Spahr, P. Novμk, *Advanced Materials*, (10) , 725 (1998).

18. D. Aurbach, E. Zinigrad, H. Teller, P. Dan, *Journal of The Electrochemical Society*, **147** (4) , 1274 (2000).

19. I. Epelboin, M. Froment, *Journal of The Electrochemical Society*, **127** (10) , 2100 (1980).

20. K. Xu, *Chemical Reviews*, **104** (10) , 4303 (2004).

21. J.M. Tarascon, M. Armand, *Nature*, **414** (6861) , 359 (2001).

22. B. Scrosati, J. Hassoun, Y.K. Sun, *Energy & Environmental Science*, **4** (9) , 3287 (2011).

23. O. Crowther, A.C. West, *Journal of The Electrochemical Society*, **155** (11) , A806 (2008).

24. Y. Cui, C.M. Lieber, *Science (New York, N.Y.)*, **291** (5505) , 851 (2001).

25. M. Dogru, T. Bein, *Nature Nanotechnology*, **6** (6) , 333 (2011).

26. M. Lazzari, *Journal of The Electrochemical Society*, **127** (3) , 773 (1980).

27. A. Herold, *Bull. Soc. Chim. France*, (187) , 999 (1955).

28. D. Fauteux, R. Koksbang, *Journal of Applied Electrochemistry*, **23** , 1 (1993).

29. Y.P. Wu, E. Rahm, R. Holze, *Journal of Power Sources*, **114** (2) , 228 (2003).

30. M. Endo, C. Kim, K. Nishimura, T. Fujino, K. Miyashita, *Carbon*, **38** (2) , 183 (2000).

31. N. Yao, L.A. Heredy, R.C. Saunders, *J. Electrochem. Soc.*, (118) , 1039 (1971).

32. C.E. Johnson, M. Foster, *J. Electrochem. Soc.*, (116) , 1612 (1969).

33. C. Wen, R.A. Huggins, *J. Solid State Chem*, (35) , 376 (1980).

34. M. Foster, C.E. Crouthamel, S.E. Wood, *J. Phys. Chem.*, (70) , 3042 (1966).

35. W. Weppner, R.A. Huggins, *J. Electrochem. Soc.*, (124) , 1569 (1977).

36. W. Weppner, R.A. Huggins, *J. Electrochem. Soc.*, (124) , 1569 (1977).

37. W. Weppner, R.A. Huggins, *J. Electrochem. Soc.*, (125) , 7 (1978).

38. G. Boukamp, G. Lash, R. Huggins, *J. Electrochem. Soc.*, (128) , 725 (1981).

39. R. Seefurth, R.A. Sharma, *J. Electrochem. Soc.*, (124) , 1207 (1977).

40. K. Ozawa, *Solid State Ionics*, **69** (3-4) , 212 (1994).

41. K. Mizushima, P.C. Jones, P.J. Wiseman, J.B. Goodenough, *Materials Research Bulletin*, **15** (6) , 783 (1980).

42. T. Ohzuku, A. Ueda, *Journal of The Electrochemical Society*, **141** (11) , 2972 (1994).

43. J.N. Reimers, J.R. Dahn, *Journal of The Electrochemical Society*, **139** (8) , 2 (1992).

44. D. Aurbach, Y. Ein-Eli, *Journal of The Electrochemical Society*, **142** (6) , 1746 (1995).

45. P.G. Bruce, A.R. Armstrong, R.L. Gitzendanner, *Journal of Materials Chemistry*, **9** , 193 (1999).

46. W.K. Pang, J.Y. Lee, Y.S. Wei, S.H. Wu, *Materials Chemistry and Physics*, **139** (1) , 241 (2013).

47. M. Thackeray, *Journal of the American Ceramic Society*, **54** , 3347 (1999).

48. A. Dey, B. Sullivan, *Journal of The Electrochemical Society*, **117** , 222 (1970).

49. T. Ohzuku, Y. Iwakoshi, K. Sawai, *Journal of The Electrochemical Society*, **140** (9) (1993).

50. Q. Wang, J. Sun, X. Yao, C. Chen, *Thermochimica Acta*, **437** (1-2) , 12 (2005).

51. J. Tarascon, D. Guyomard, *Solid State Ionics*, **69** (3-4) , 293 (1994).

52. C. Barlowz, *Electrochemical and Solid-State Letters*, **2** (8) , 362 (1999).

53. T. Kawamura, S. Okada, J. Yamaki, *Journal of Power Sources*, **156** (2) , 547 (2006).

54. S.G. Wirasingha, N. Schofield, A. Emadi, in, Veh. Power Propuls. Conf., IEEE, (2008), p. 1.

55. Y. Guo, F. Zhang, J. Yang, F. Wang, Y. NuLi, S. Hirano, *Energy & Environmental Science*, **5** (10) , 9100 (2012).

56. S.-W. Kim, D.-H. Seo, X. Ma, G. Ceder, K. Kang, *Advanced Energy Materials*, **2** (7) , 710 (2012).

57. H.D. Yoo, I. Shterenberg, Y. Gofer, G. Gershinsky, N. Pour, D. Aurbach, *Energy & Environmental Science*, **6** (8) , 2265 (2013).

58. J. Muldoon, C.B. Bucur, A.G. Oliver, T. Sugimoto, M. Matsui, H.S. Kim, G.D. Allred, J. Zajicek, Y. Kotani, *Energy & Environmental Science*, **5** (3) , 5941 (2012).

59. D. Aurbach, Y. Gofer, Z. Lu, A. Schechter, O. Chusid, H. Gizbar, Y. Cohen, V. Ashkenazi, M. Moshkovich, R. Turgeman, *Journal of Power Sources*, **97-98** , 28 (2001).

60. Y. NuLi, J. Yang, Y. Li, J. Wang, *Chemical Communications (Cambridge, England)*, **46** (21) , 3794 (2010).

61. M. Gaultois, T. Sparks, *Chemistry of Materials*, **25** , 2911 (2013).

62. F. Wang, Y. Guo, J. Yang, Y. Nuli, S. Hirano, *Chemical Communications (Cambridge, England)*, **48** (87) , 10763 (2012).

63. Y. Guo, J. Yang, Y. NuLi, J. Wang, *Electrochemistry Communications*, **12** (12) , 1671 (2010).

64. D. Aurbach, H. Gizbar, A. Schechter, O. Chusid, H.E. Gottlieb, Y. Gofer, I. Goldberg, *Journal of The Electrochemical Society*, **149** (2) , A115 (2002).

65. C. Liebenow, Z. Yang, P. Lobitz, *Electrochemistry Communications*, **2** , 641 (2000).

66. D. Aurbach, M. Moshkovich, A. Schechter, R. Turgeman, *Electrochemical and Solid-State Letters*, **3** (1) , 31 (2000).

67. R.E. Doe, R. Han, J. Hwang, A.J. Gmitter, I. Shterenberg, H.D. Yoo, N. Pour, D. Aurbach, *Chemical Communications (Cambridge, England)*, **50** (2) , 243 (2014).

68. R. Mohtadi, M. Matsui, T.S. Arthur, S.J. Hwang, *Angewandte Chemie (International Ed. in English)*, **51** (39) , 9780 (2012).

69. T.T. Tran, W.M. Lamanna, M.N. Obrovac, *Journal of the Electrochemical Society*, **159** (12) , A2005 (2012).

70. N. Singh, T.S. Arthur, C. Ling, M. Matsui, F. Mizuno, *Chemical Communications (Cambridge, England)*, **49** (2) , 149 (2013).

71. T.S. Arthur, N. Singh, M. Matsui, *Electrochemistry Communications*, **16** (1) , 103 (2012).

72. O.I. Malyi, T.L. Tan, S. Manzhos, *Journal of Power Sources*, **233** , 341 (2013).

73. V. Shklover, T. Haibach, *Journal of Solid State Chemistry*, **323** (123) , 317 (1996).

74. P. Bruce, F. Krok, J. Nowinski, *J. Mater. Chem.*, **1** (4) , 705 (1991).

75. P. Novk, J. Desilves, *Journal of The Electrochemical Society*, **140** (1) , 140 (1993).

76. G.G. Amatucci, F. Badway, a. Singhal, B. Beaudoin, G. Skandan, T. Bowmer, I. Plitz, N. Pereira, T. Chapman, R. Jaworski, *Journal of The Electrochemical Society*, **148** (8) , A940 (2001).

77. K. Makino, Y. Katayama, T. Miura, T. Kishi, *Journal of Power Sources*, **99** , 66 (2001).

78. N. Amir, Y. Vestfrid, O. Chusid, Y. Gofer, D. Aurbach, *Journal of Power Sources*, **174** (2) , 1234 (2007).

79. R. Chevrel, M. Sergent, J. Prigent, *Materials Research Bulletin*, **9** (11) , 1487 (1974).

80. E. Lancry, E. Levi, Y. Gofer, M. Levi, G. Salitra, D. Aurbach, *Chem. Mater*, **16** , 2832 (2004).

81. M.D. Levi, H. Gizbar, E. Lancry, Y. Gofer, E. Levi, D. Aurbach, *Journal of Electroanalytical Chemistry*, **569** (2) , 211 (2004).

82. D. Aurbach, I. Weissman, Y. Gofer, E. Levi, *Chemical Record (New York, N.Y.)*, **3** (1) , 61 (2003).

83. T. Ichitsubo, T. Adachi, S. Yagi, T. Doi, *Journal of Materials Chemistry*, **21** (32) , 11764 (2011).

84. P. Balaya, H. Li, L. Kienle, J. Maier, *Advanced Functional Materials*, **13** (8) , 621 (2003).

85. H. Kobayashi, Y. Kawamoto, M. Tabuchi, M. Takano, *Solid State Ionics*, **82** , 25 (1995).

86. A.M. Stux, K.E. Swider-Lyons, *Journal of The Electrochemical Society*, **152** (10) , A2009 (2005).

87. T.E. Sutto, T.T. Duncan, *Electrochimica Acta*, **79** , 170 (2012).

88. R. Demir-Cakan, M. Morcrette, F. Nouar, C. Davoisne, T. Devic, D. Gonbeau, R. Dominko, C. Serre, G. Férey, J.-M. Tarascon, *Journal of the American Chemical Society*, **133** (40) , 16154 (2011).

89. P. Jolibois, *Compt.Rend*, (155) , 353 (1912).

90. O. Mizrahi, N. Amir, E. Pollak, O. Chusid, V. Marks, H. Gottlieb, L. Larush, E. Zinigrad, D. Aurbach, *Journal of The Electrochemical Society*, **155** (2) , A103 (2008).

91. Y. Vestfried, O. Chusid, Y. Goffer, *Organometallics*, **26** , 3130 (2007).

92. N. Pour, Y. Gofer, D.T. Major, D. Aurbach, *Journal of the American Chemical Society*, **133** (16) , 6270 (2011).

93. C. Liao, B. Guo, D. Jiang, R. Custelcean, S.M. Mahurin, X.-G. Sun, S. Dai, *Journal of Materials Chemistry A*, **2** (3) , 581 (2014).

94. S.Y. Ha, Y.W. Lee, S.W. Woo, B. Koo, J.-S. Kim, J. Cho, K.T. Lee, N.-S. Choi, *ACS Applied Materials & Interfaces*, **6** (6) , 4063 (2014).

95. M. Deutsch, G. Holzer, J. Hartwigs, J. Wolf, M. Fritsch, E. Forster, *The Americal Physical Society*, **51** (1) (1995).

96. H.Putz, K.Brandenburg, , Match!Phase Identification from Powder Diffraction (n.d.).

97. B.A. Hunters, , IURC Powder Diffraction 22 (1997).

98. J.C. Burns, L.J. Krause, D.-B. Le, L.D. Jensen, a. J. Smith, D. Xiong, J.R. Dahn, *Journal of The Electrochemical Society*, **158** (12) , A1417 (2011).

99. D.A. Stevens, J.R. Dahn, *Journal of The Electrochemical Society*, **147** (4) , 1271 (2000).

100. M. Chamas, M. Sougrati, C. Reibel, P. Lippens, *Chemistry of Materials*, **25** , 2410 (2013).

101. K. Cheung, W. Lindsay, D. Friedland, *Journal of The Electrochemical Society*, **2** , 1 (1985).

102. A. Blyr, C. Sigala, G. Amatucci, D. Guyomard, Y. Chabre, J.M. Tarascon, *Journal of The Electrochemical Society*, **145** (1) , 194 (1998).

103. M. Ender, A. Weber, E. Ivers-Tiffée, *Journal of The Electrochemical Society*, **159** (2) , A128 (2012).

104. S. Klink, E. Madej, E. Ventosa, A. Lindner, W. Schuhmann, F. La Mantia, *Journal of The Electrochemical Society*, **22** , 120 (2012).

105. Z. Lu, a. Schechter, M. Moshkovich, D. Aurbach, *Journal of Electroanalytical Chemistry*, **466** (2) , 203 (1999).

106. E. Lancry, E. Levi, Y. Gofer, M.D. Levi, D. Aurbach, *Journal of Solid State Electrochemistry*, **9** (5) , 259 (2005).

107. R.E. Doe, R. Han, J. Hwang, A.J. Gmitter, I. Shterenberg, H.D. Yoo, N. Pour, D. Aurbach, *Chemical Communications (Cambridge, England)*, **50** (2) , 243 (2014).

108. T.T. Tran, M.N. Obrovac, *Journal of The Electrochemical Society*, **158** (12) , A1411 (2011).

109. Y. Shao, M. Gu, X. Li, Z. Nie, P. Zuo, G. Li, T. Liu, J. Xiao, Y. Cheng, C. Wang, J.-G. Zhang, J. Liu, *Nano Letters*, **14** (1) , 255 (2014).

110. R. Salomone, F. Mondello, F. Lanuzza, G. Micali, *Environmental Management*, **35** (2) , 206 (2005).

111. S.D. Beattie, T. Hatchard, A. Bonakdarpour, K.C. Hewitt, J.R. Dahn, *Journal of the Electrochemical Society*, **150** (6) , A701 (2003).

112. L.D. Ellis, T.D. Hatchard, M.N. Obrovac, *Journal of the Electrochemical Society*, **159** (11) , A1801 (2012).

113. L.D. Ellis, B.N. Wilkes, T.D. Hatchard, M.N. Obrovac, *Journal of the Electrochemical Society*, **161** (3) , A416 (2014).

114. J.-S. Bridel, S. Grugeon, S. Laruelle, J. Hassoun, P. Reale, B. Scrosati, J.-M. Tarascon, *Journal of Power Sources*, **195** (7) , 2036 (2010).

115. A.J. Smith, J.C. Burns, X. Zhao, D. Xiong, J.R. Dahn, *Journal of The Electrochemical Society*, **158** (5) , A447 (2011).

116. I. Courtney, J. Tse, O. Mao, J. Hafner, J. Dahn, *Physical Review B*, **58** (23) , 15583 (1998).

117. J. Dahn, I. Courtney, O. Mao, *Solid State Ionics*, **111** , 289 (1998).

118. Ø. Fischer, *Applied Physics*, **16** , 1 (1978).

119. T. Tsubota, M. Ohtaki, K. Eguchi, *Journal of Ceramic Society of Japan*, **107** (8) , 697 (1999).

120. E. Gocke, R. Schöllhorn, G.Aselmann, W. Muller-Warmuth, *Inorganic Chemistry*, **26** (11) (1987).

121. W. McKinnon, J. Dahn, *Physical Review B*, **31** (5) , 3084 (1985).

122. S. Seghir, C. Boulanger, S. Diliberto, J.-M. Lecuire, M. Potel, O. Merdrignac-Conanec, *Electrochemistry Communications*, **10** (10) , 1505 (2008).

123. S. Seghir, C. Boulanger, S. Diliberto, M. Potel, J.-M. Lecuire, *Electrochimica Acta*, **55** (3) , 1097 (2010).

124. M. Levi, E. Lancri, E. Levi, H. Gizbar, Y. Gofer, D. Aurbach, *Solid State Ionics*, **176** (19-22) , 1695 (2005).

125. C. Ritter, C. Niildeke, W. Press, R. Schiillhorn, *Z. Phys. B*, **92** , 437 (1993).

126. S. Kondo, K. Takada, Y. Yamamura, H. Gyoten, S. Yoshida, *Solid State Ionics*, **57** (1-2) , 147 (1992).

127. E. Levi, Y. Gofer, Y. Vestfreed, *Chemistry of Materials*, (11) , 2767 (2002).

128. M. Rabiller-Baudry, M. Sergent, R. Chevrel, *Materials Research Bulletin*, **26** (6) , 519 (1991).

129. W.V. Evans, F.H. Lee, C.H. Lee, *Journal of American Chemical Society*, **57** (489) (1935).

130. Y. Gofer, O. Chusid, H. Gizbar, Y. Viestfrid, H.E. Gottlieb, V. Marks, D. Aurbach, *Electrochemical and Solid-State Letters*, **9** (5) , A257 (2006).

131. H.S. Kim, T.S. Arthur, G.D. Allred, J. Zajicek, J.G. Newman, A.E. Rodnyansky, A.G. Oliver, W.C. Boggess, J. Muldoon, *Nature Communications*, **2** , 427 (2011).

APPENDIX A   COPYRIGHT PERMISSSION LETTERS

Figure 2.3:

Figure 2.4:

License Number	3438360051107
License date	Jul 29, 2014
Licensed content publisher	Nature Publishing Group
Licensed content publication	Nature
Licensed content title	Prototype systems for rechargeable magnesium batteries
Licensed content author	D. Aurbach, Z. Lu, A. Schechter, Y. Gofer, H. Gizbar et al.
Licensed content date	Oct 12, 2000
Type of Use	reuse in a dissertation / thesis
Volume number	407
Issue number	6805
Requestor type	academic/educational
Format	print and electronic
Portion	figures/tables/illustrations
Number of figures/tables/illustrations	1
Figures	Figure 3
Author of this NPG article	no
Your reference number	Figure 2.4
Title of your thesis / dissertation	Developing of New Cell design for Metal Battery Research and Investigating Electrode Materials and Electrolyte Systems for Mg Batteries
Expected completion date	Aug 2014
Estimated size (number of pages)	128
Total	0.00 USD

Chapter 04: